Fakultät für Physik der Technischen Universität München
Physik-Department E12

The Evolution of $B(E2)$ Values Around the Doubly-Magic Nucleus ^{132}Sn

Thomas Behrens

Vollständiger Abdruck der von der Fakultät für Physik der Technischen Universität München zur Erlangung des akademischen Grades eines

Doktors der Naturwissenschaften (Dr. rer. nat.)

genehmigten Dissertation.

Vorsitzender: Univ.-Prof. Dr. Harald Friedrich
Prüfer der Dissertation:
1. Univ.-Prof. Dr. Reiner Krücken
2. Univ.-Prof. Dr. Stephan Paul

Die Dissertation wurde am 16.07.2009 bei der Technischen Universität München eingereicht und durch die Fakultät für Physik am 24.08.2009 angenommen.

Abstract

In this work the evolution of $B(E2)$ values in nuclei around the $N = 82$ shell closure has been studied. The reduced transition strength between ground state and first excited 2^+ state is a good indicator for the collectivity in even-even nuclei. Former experimental and theoretical investigations of the region above $N = 82$ indicated that the $B(E2)$ values might be systematically lower than expected and questioned the current understanding of collective excitations.

Since the experimental data concerning the proposed $N = 82$ shell quenching for nuclei below ^{132}Sn is not yet conclusive, a systematic investigation of neutron-rich nuclei both below and above this shell closure has been performed at the Radioactive Ion Beam Facility REX-ISOLDE at CERN.

The $B(E2)$ values of $^{122-126}$Cd ($N < 82$) and $^{138-144}$Xe ($N > 82$) have been measured by Coulomb excitation in inverse kinematics, applying the MINIBALL γ-detector array. The values of ^{124,126}Cd and ^{138,142,144}Xe have been determined for the first time, whereas for ^{140}Xe the ambiguity of the two contradicting published $B(E2)$ values has been solved. The relative uncertainty of the $B(E2)$ value of ^{122}Cd could be reduced significantly. For ^{140,142}Xe the Coulomb excitation cross section for the $2_1^+ \rightarrow 4_1^+$ transition has also been determined. Further, the deorientation effect and the influence of the quadrupole deformation on the Coulomb excitation cross section have been taken into account for $^{138-142}$Xe. It could be shown that the latter plays an important role for the determination of the $B(E2)$ values.

Assuming only a small or even vanishing quadrupole moment, all measured $B(E2)$ values agree with the expectations and no sign for a quenching of the $N = 82$ gap could be seen.

Zusammenfassung

In dieser Arbeit wurde die Entwicklung der $B(E2)$-Werte um den $N = 82$ Schalenabschluss untersucht. Die $E2$ Übergangswahrscheinlichkeit vom Grundzustand in den ersten angeregten 2^+ Zustand gilt als wichtiger Indikator für die Kollektivität von gg-Kernen. Frühere experimentelle und theoretische Untersuchungen wiesen darauf hin, dass die $B(E2)$-Werte für Kerne mit $N > 82$ systematisch niedriger sein könnten als erwartet und stellten das bisherige Verständnis kollektiver Anregungen in Frage.

Da auch die vorgeschlagene Reduktion der Energielücke bei $N = 82$ für Kerne unterhalb des doppelt-magischen ^{132}Sn experimentell bislang noch nicht eindeutig bestätigt oder widerlegt werden konnte, erschien eine systematische Untersuchung neutronenreicher Kerne um diesen Schalenabschluss notwendig.

Daher wurden die $B(E2)$-Werte von $^{122-126}$Cd ($N < 82$) und $^{138-144}$Xe ($N > 82$) mittels Coulombanregung in inverser Kinematik bei REX-ISOLDE am CERN gemessen. Die dabei emittierte γ-Strahlung wurde mit dem MINIBALL Spektrometer detektiert. Die $B(E2)$-Werte von ^{124,126}Cd sowie von ^{138,142,144}Xe wurden erstmals gemessen und das Problem der zwei widersprüchlichen $B(E2)$-Werte von ^{140}Xe in der Literatur konnte aufgelöst werden. Der $B(E2)$-Wert von ^{122}Cd wurde mit deutlich besserer Genauigkeit bestimmt. Ausserdem konnte für ^{140,142}Xe der Wirkungsquerschnitt für die $2_1^+ \rightarrow 4_1^+$ Coulombanregung bestimmt werden.

Bei der Analyse der Daten von $^{138-142}$Xe wurde darüberhinaus die anisotrope Emission der γ-Strahlung sowie der Einfluss eines nicht-verschwindenden Quadrupolmoments berücksichtigt. Es zeigt sich, dass letzteres eine signifikante Rolle bei der Bestimmung der $B(E2)$-Werte spielt.

Unter der Annahme eines kleinen bzw. verschwindenden Quadrupolmoments konnte gezeigt werden, dass die gemessenen $B(E2)$-Werte mit den Erwartungen übereinstimmen und es keinen Hinweis auf eine Reduktion der $N = 82$ Energielücke gibt.

Contents

—Die Neugier steht immer an erster Stelle eines Problems, das gelöst werden will.

Galileo Galilei (1564-1642)

1 The Nuclear Landscape

1.1 The Nuclear Chart

It is known since the famous scattering experiments by Geiger and Marsden (1909) and the interpretation of its results by Rutherford (1911) that all positive charge of the atom and almost all its mass is concentrated in its center – the *nucleus* – with negatively charged electrons surrounding it. The size of the nucleus was estimated by Geiger to about 10 fm[1] which is about 10^4 times smaller than the typical size of an atom. But it was not until the discovery of the neutron (Chadwick, 1932) that the constituents of the nucleus were identified correctly. Since then the nucleus is known to consist of positively charged protons and electrically neutral neutrons.

In order to describe this nucleus Heisenberg (1932) introduced the *isospin* concept: protons and neutrons are therefore merely two different states of the same elementary particle - the *nucleon*. This concept is formally similar to the concept of intrinsic spin. The isospin of a nucleon is then $T = 1/2$ and its projection is $T_z = +1/2$ for neutrons (n) or $T_z = -1/2$ for protons (p). A two-nucleon system can then have a total isospin of $T = 1$ (triplet) or $T = 0$ (singlet). In the triplet state the projected isospin can either have values of $T_z = +1$, 0 or -1 for the pp-, pn- or nn-system, respectively. However, only the pn system can appear in the singlet state with $T_z = 0$, so pn has a $T = 0$ as well as a $T = 1$ component.

The nucleus is then determined by its *charge number* Z (i.e. its number of protons) and its number of neutrons N (or its *mass number* $A = Z + N$). It is usually noted ${}^{A}_{Z}X_N$ with X being the chemical symbol. Today, there are nearly 3000 nuclei known, out of which less than 300 are stable. In a *nuclear chart*, all these nuclei are drawn corresponding to their Z and N values. In figure 1.1 such a nuclear chart is shown with the valley of stability indicated in black and the area of known nuclei indicated in yellow. Also shown in this figure is the area where the existence of nuclei is assumed,

[1] 1 fm (femtometer) = 10^{-15} m. It is often called 1 fermi in honour of Enrico Fermi.

but not yet proven (the so-called *terra incognita*). Although there is little or nothing known about these nuclei, neither experimentally nor theoretically, their existence is essential for understanding the production of heavy nuclei.

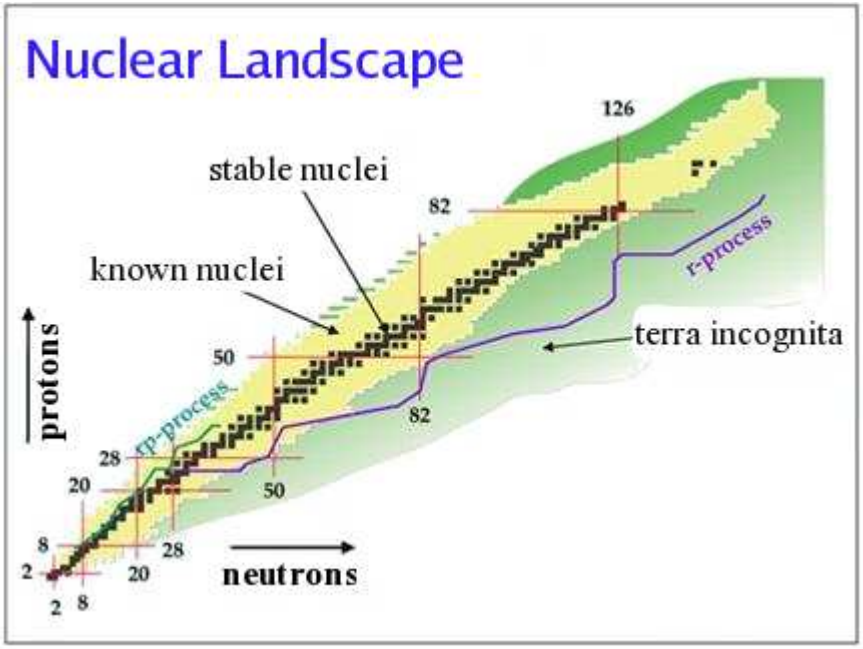

Figure 1.1: The nuclear landscape with the valley of stability (black), the area of known but unstable nuclei (yellow) and the region where the existence of nuclei is assumed (green). The paths of two nucleosynthesis processes are indicated. The magic numbers are shown by red lines (see text for details). Taken from the Argonne National Laboratory website.

Since in the early universe only the lightest elements like H and He were present, the production of heavier elements (*nucleosynthesis*) has to be explained by several different nuclear processes. Only elements up to iron can be produced by fusion reactions (*burning*) in stars (e.g. by the famous CNO-cycle in our sun) and later distributed to the interstellar medium. The production of nuclei beyond iron is due to nuclear capture reactions which have to compete with β-decays.

(i) In the slow neutron capture process (*s-process*) the neutron capture time τ_n is larger than the corresponding β-decay time τ_β, hence this process runs through or close to the valley of stability. The abundances of s-process elements are inversely proportional to the neutron capture cross sections which is consistent with a steady flow of neutrons.

(ii) The rapid neutron capture process (*r-process*) occurs in environments with high temperatures and extreme neutron fluxes, e.g. core-collapse supernovae. Here, τ_n is much shorter than τ_β. Hence, more and more neutrons are added before the nucleus can decay and the r-process runs through the extremely neutron-rich nuclei far from stability. It is worth mentioning here that this process stalls at nuclei with certain (*magic*) neutron numbers due to their low neutron absorption cross section. The neutron shell closure at $N = 82$ (see next section) is supposed to be correlated

with the $A \approx 130$ peak in the solar-system abundance of heavy elements.

(iii) The rapid proton capture process (*rp-process*) can occur especially in hydrogen-rich environments at high temperatures (Wallace and Woosley, 1981). It is considered to play a substantial role in the production of nuclei on the neutron-deficient side of stability, e.g. it explains very well the observed abundances of neutron-deficient nuclei with $A \lesssim 100$ (Schatz et al., 1998).

Among the most important nuclear properties for understanding and modeling these processes are nuclear half-lives, separation energies (or masses) and neutron capture cross sections. Since experimental data far off stability is scarce, these properties often have to be deduced from nuclear models. The aim of nuclear structure physics is then to improve these models by gathering further experimental data on these nuclei, describing and interpreting nuclear properties and by probing the interaction between nucleons.

There are two complementary approaches to describe the nucleus:

(i) a microscopic approach, where nucleons are treated as independent particles moving in a central potential arising from the interaction of each nucleon with all other nucleons. One of the simplest such models is the so-called Fermi gas model in which the nucleons are considered as non-interacting particles in a 3-dimensional square well potential. This leads to energy eigenvalues $E \propto (n/d)^2$ where n is the radial quantum number and d the size of the well. The total kinetic energy of this system is then $E_{tot} \propto (N-Z)^2$ which is consistent with the stable nuclei having $N \approx Z$. For $A \gtrsim 40$ the repulsive Coulomb interaction between the protons leads to a neutron excess. This model can be seen as predecessor of the successful *shell model* (see next section).

(ii) a macroscopic approach where the nucleus is treated like a macroscopic (or geometric) object. One of the earliest nuclear models, the liquid drop model (first described by Gamow (1930)), belongs in this category. There, the nucleus is described similar to a drop of an incompressible liquid. The observed masses and binding energies can be well deduced from it (von Weizsäcker, 1935). In this model the nucleus has a surface and a shape and excitations can be described in terms of collective vibration and rotation. These ideas are also essential in the *collective* model by Bohr and Mottelson (1975).

For more details about both approaches see also Heyde (1999).

1.1.1 Properties of Nuclei and the Nuclear Force

From the fact that bound nuclei exist it can be seen that there must be an attractive interaction between the nucleons which is stronger than the repulsive Coulomb force between the protons – the *nuclear force*. On the other hand it is known from scattering experiments that the nuclear density is nearly constant. This shows that there must be a repulsive core at very short distances. The volume of the nucleus then has to increase as $V \propto A$, hence the mean nuclear radius can be defined as $R = R_0 \cdot A^{1/3}$ with R_0 being a constant between 1.2 fm and 1.3 fm.

The mass of a nucleus can be expressed as the sum of the masses of the nucleons

minus its binding energy[2]

$$M = Z \cdot m_p + N \cdot m_n - E_b.$$

It is interesting to note that for $A \gtrsim 20$ the binding energy per nucleon E_b/A saturates to about 8 MeV (cf. figure 1.2). This can be explained by assuming that nucleons

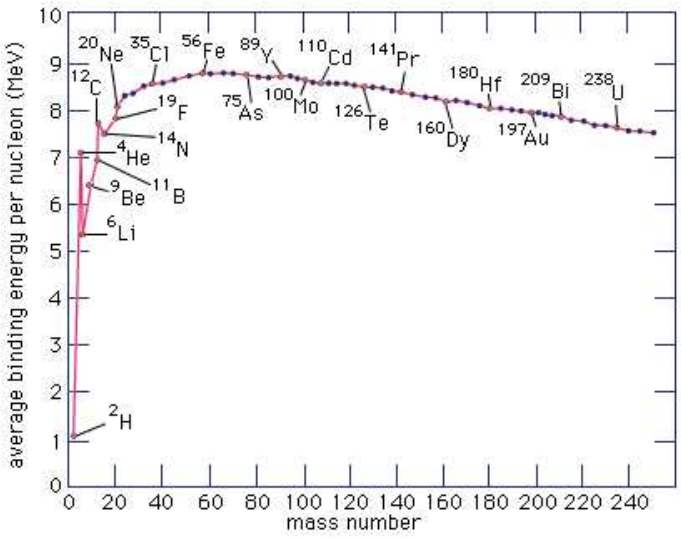

Figure 1.2: Nuclear binding energy per nucleon. The saturation and its slight decrease above iron can be seen (©2007 Encyclopædia Britannica, Inc.).

interact only with their nearest neighbours, i.e. the range of the nuclear force is only of the order of 1 fm.

Related to the binding energy are the neutron (proton) separation energies S_n (S_p). These are defined as the energies needed to remove a neutron (proton) from a nucleus ${}^{A}_{Z}X_N$ to infinity. Hence, they are equal to the difference in binding energies between ${}^{A}_{Z}X_N$ and ${}^{A-1}_{Z}X_{N-1}$ (${}^{A-1}_{Z-1}X_N$). In general, the separation energies decrease with an increasing number of like nucleons and increase with an increasing number of unlike nucleons (cf. figure 1.3). For certain values of Z or N the separation energies show large and sudden drops. These values turn out to be the so-called *magic numbers* (see section 1.2). This behaviour is similar to the behaviour ionizationion energies in atoms and already hints to a certain analogy in structure. And just as a lot of knowledge on atoms was gained by studying their excited states, a lot about nuclear structure can be learned by studying nuclear excited states, their energies, spins and parities (the latter are usually denoted as J^π). As an example, the energies of the first excited states are highest for nuclei with magic nucleon numbers and reach their minimum in the mid-shell region which is another evidence for magicity in nuclei.

The behaviour of the separation energies shows that there is a strong attractive p-n-interaction, whereas the residual interaction between like nucleons is repulsive.

[2]Masses and energies are used equivalently and factors of c^2 are skipped throughout this thesis.

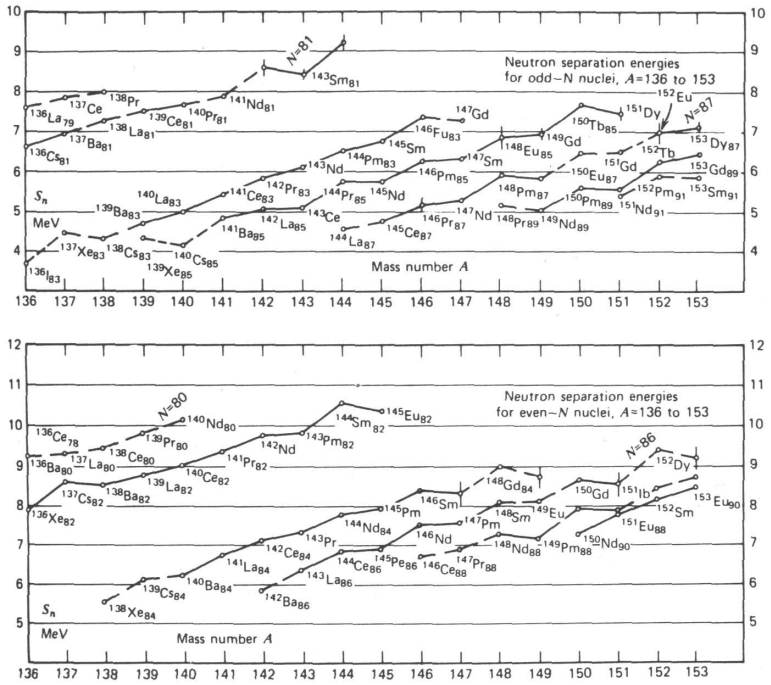

Figure 1.3: Neutron separation energies near the N=82 magic number (from Casten (2000)).

However, looking closer at S_n (S_p), an oscillation between odd and even numbers of neutrons (protons) can be seen. This hints to an attractive *pairing* interaction coupling neutrons (protons) to $J^\pi = 0^+$. Hence, the ground state in even-even nuclei is always $J^\pi = 0^+$.

More information on the nucleon-nucleon-interaction can be gained from data on mirror nuclei. These are nuclei where the proton and neutron number exchange, e.g. $^{27}_{13}\mathrm{Al}_{14}$ and $^{27}_{14}\mathrm{Si}_{13}$. The similarity of their level schemes (energies, spins and parities of their excited states) suggests that the nuclear force is charge independent, i.e. *p*-*p*-, *p*-*n*- and *n*-*n*-interactions are equal. However, this is only true for triplet state ($T = 1$). The $T = 0$ component of the nuclear interaction can be very different. With the example of the deuteron it can be shown that the interaction of two unlike nucleons is more attractive in the $T = 0$ state than in the $T = 1$ state (cf. Casten (2000)).

1.2 Nuclear Shell Model

The most important and successful model to describe nuclei microscopically is the shell model. As mentioned in the section above the shell model is a development of the independent particle model in which the nucleons are considered as non-interacting particles moving in a central potential $U(\vec{r})$. The main difference to the description of electrons in atomic physics stems from the fact that the central potential is produced by the nucleons itself. Therefore, the basis for this potential has to be the two-body

nucleon-nucleon interaction V_{ik}. The resulting Hamiltonian is then:

$$H = \sum_{i=1}^{A} -\frac{\hbar^2}{2m_i}\Delta_i + \sum_{i>k=1}^{A} V_{ik}(\vec{r_i} - \vec{r_k}). \tag{1.1}$$

Since this Hamiltonian becomes practical unsolvable for increasing A it needs to be simplified. This is done by introducing a *mean field* in which all nucleons move:

$$H = \left[\sum_{i=1}^{A} -\frac{\hbar^2}{2m_i}\Delta_i + U_i(\vec{r})\right] + \left[\sum_{i>k=1}^{A} V_{ik} - \sum_{i=1}^{A} U_i(\vec{r})\right] = H_0 + H_{res}. \tag{1.2}$$

The central potential $U(\vec{r})$ is chosen such that H_{res} is a small perturbation compared to H_0. This can be achieved in a self-consistent approach, starting from effective nucleon-nucleon interaction, by Hartree-Fock methods. With a reasonable nuclear potential the solutions of the Schrödinger equation for the unperturbed Hamiltonian H_0 should reproduce the observed magic numbers:

$$\left[\sum_{i=1}^{A} -\frac{\hbar^2}{2m_i}\Delta_i + U_i(\vec{r})\right]\Psi(\vec{r}) = \left[\sum_{i=1}^{A} h_0^{(i)}\right]\Psi(\vec{r}) = E\Psi(\vec{r}). \tag{1.3}$$

The single-particle equations are then given by $h_0^{(i)}\psi_i = \epsilon_i\psi_i$ with

$$\Psi(\vec{r}) = \prod_i \psi_i \qquad \text{and} \qquad E = \sum_i \epsilon_i.$$

In spherical coordinates the equation is usually simplified by separating the wave function in its radial and angular coordinates. The resulting wave function is then given by

$$\psi(\vec{r}) = R_{nl}(r)Y_{lm}(\theta, \phi)$$

with $-l \leq m \leq l$ and energy eigenvalues E_{nl} (see e.g. Heyde (1999) for details). The radial solutions of the Schrödinger equation $R_{nl}(r)$ show that states with higher n have higher energy and that – for the same n – states with higher l have higher energies. These two effects can counterbalance and lead to the grouping of levels at similar energies with larger gaps in-between. A reasonable first approximation for the central potential is the harmonic oscillator potential

$$U(r) = \frac{1}{2}m\omega^2 r^2 \tag{1.4}$$

which results in energy eigenvalues

$$E_{nl} = \left(2n + l - \frac{1}{2}\right)\hbar\omega = \left(N + \frac{3}{2}\right)\hbar\omega \tag{1.5}$$

with $N = 2(n-1) + l$ being the principle quantum number. The energy levels are degenerated multiplets defined by the values of $2n + l$.

Including the intrinsic spin of the nucleons $s = 1/2$ the total angular momentum quantum number can be defined as $j = l \pm 1/2$. The number of nucleons per orbit is then limited to $2j + 1$. The magic numbers resulting from this potential are

2, 8, 20, 40, 70, 112 ... which deviates from observation for $A \geq 40$. Therefore, some modifications to this potential are necessary. Since nucleons with angular momentum experience a centrifugal force, an additional term U_{cent} appears in the potential

$$U_{cent} = \int m\omega^2 r^2 dr = \int \frac{L^2}{mr^3} dr = \frac{l(l+1)\hbar^2}{2mr^2}$$

which is proportional to $\hat{l}^2$. This term effectively flattens the potential in the center which is quite reasonable since nucleons in the center are uniformly surrounded by other nucleons and should feel no net force. This modification breaks some of the degeneracy of the simple harmonic oscillator potential levels, but still does not reproduce the observed magic numbers.

It was the ground-breaking idea of Mayer (1950) and – independently – Haxel et al. (1950) that the potential should include a spin-orbit coupling term $U_{\hat{l}\hat{s}}(r) = \alpha(r)\hat{l} \cdot \hat{s}$. Here, $\hat{l}$ is the orbital angular momentum operator and $\hat{s}$ the intrinsic spin operator. This term stems from a quantum relativistic effect and is more difficult to describe intuitively. However, as nucleons in the center feel no net force, the spin-orbit force can be regarded as a surface phenomenon with $\alpha(r) = -U_{ls} \cdot \frac{\partial}{\partial r} U(r)$. It is worth emphasizing here that absolute strength of the spin-orbit coupling must be of the same magnitude as the central potential itself to reproduce the correct magic numbers.

The coupling term can be rewritten using the total angular momentum operator $\hat{j} = \hat{l} + \hat{s}$. There are then two slightly different potentials and hence different energy eigenvalues for the different values of j:

$$\epsilon_{nlj} = \left\{ 2n + l - \frac{1}{2} \right\} \hbar\omega + \alpha \begin{cases} -l: & j = l + 1/2 \\ l+1: & j = l - 1/2 \end{cases} \tag{1.6}$$

With this approach the resulting magic numbers are 2, 8, 20, 28, 50, 82, 126 in accordance with the experimental data (see figure 1.4). However, it should be noted that the harmonic oscillator potential is infinite and has the wrong asymptotic behaviour. In practice, finite potentials like the more realistic Woods-Saxon potentials of the form

$$U(r) = \frac{U_0}{1 + exp[(r - R_0)/a]} + U_{ls}(r)$$

are often used.

1.2.1 Collectivity & Deformation

In practice the use of the shell model is rather limited. It works best for nuclei with only one or a few nucleons[3] outside a closed shell, i.e. *valence nucleons*. However, the more valence nucleons are present the more important residual interactions become and nuclear structure physics today concentrates a lot on the nature of these interactions and their effects on the level scheme.

The residual interactions, described by the term H_{res} in eq. 1.2, can be expanded in its multipoles. The monopole term describes the single particle energies of the nucleons whereas the higher-order terms will be responsible for the excitation spectrum of the nucleus. Among these excitations it is the electric quadrupole $(E2)$[4] mode which is

[3] These could also be holes in this sense.

[4] The nomenclature used here is EL or ML for electric or magnetic transitions of multipole order 2^L.

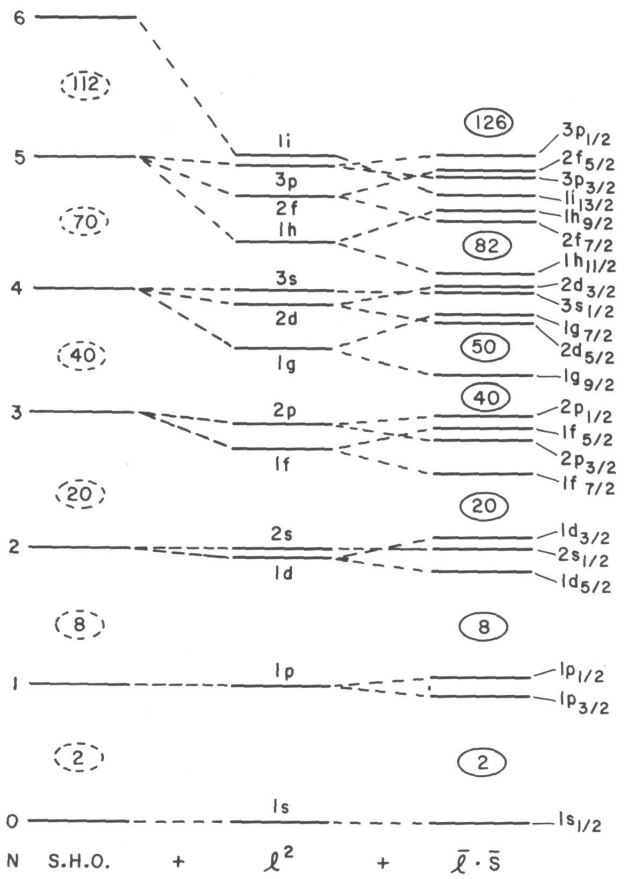

Figure 1.4: Level scheme of the shell model: on the left for the simple harmonic oscillator potential, in the middle modified by the $\hat{l}^2$ term and on the right including the spin-orbit coupling term. Taken from Casten (2000).

of peculiar interest for this work. The low-energy $E2$ excitations can be interpreted as vibrational and rotational modes of the nucleus. This oscillation in shape can be described by a new parametrization of the nuclear radius in the intrinsic frame

$$R_{osc} = R \cdot \left[1 + \sum_m \alpha_m Y_{2m}(\theta, \phi)\right] \tag{1.7}$$

with R being the mean nuclear radius as mentioned in section 1.1, Y_{2m} being spherical harmonics of order 2 and m being the magnetic substates. The expansion coefficients α_m can be expressed as

$$\alpha_0 = \beta \cos\gamma \quad \text{and} \quad \alpha_2 = \alpha_{-2} = \frac{1}{\sqrt{2}}\beta \sin\gamma.$$

The other two coefficients $\alpha_{\pm 1}$ are zero in the intrinsic frame. Here, β represents the quadrupole deformation and γ describes the axial asymmetry. Most nuclei are (almost) axially symmetric, i.e. $\gamma = 0°$.

For mid-shell nuclei with many valence nucleons alternatives to the shell model are inevitable. Two further developments are worth mentioning here, both involving the concept of a nonspherical shape. In the deformed shell model (or *Nilsson model*) the independent particle motion in a field of nonspherical shape is considered whereas in the *collective* model the macroscopic motions and excitations of a nucleus having this shape are described. As pointed out above the residual interactions are responsible for the deformation from spherical shape and for the collective behaviour of the nucleus. Among the residual interactions the pairing interaction (see section 1.1) should once more be emphasized here: it couples like nucleons to $J^\pi = 0^+$ states, hence the ground-state in all even-even nuclei is a 0^+ state and the first excited state in (almost) all even-even nuclei is a 2^+ state. Therefore, the transition from the ground-state to the first excited state (and vice versa) is an electric quadrupole ($E2$) transition. Since collective effects in low-lying states are of quadrupole character the study of these transitions is of great interest for nuclear structure physics (see also Casten (2000)).

1.3 Evolution of Nuclear Structure

When studying nuclear structure over a wide range in the nuclear chart, e.g. from shell closures up to mid-shell regions, one studies the increasing influence of residual interactions and collective properties become more important. The degree (and type) of collectivity can be expressed in terms of the energy ratio of the first 4^+ state to the first 2^+ state, i.e. $\mathcal{R}_{42} = E(4_1^+)/E(2_1^+)$. This ratio is one of the key signatures for nuclear structure and ranges from values well below 2.0 near closed shells, between 2.0 and 2.5 for nuclei with vibrational excitations and up to values at ~ 3.33 for nuclei with purely rotational excitations. In table 1.1 the values $\mathcal{R}_{42}$ for the isotopes that will be studied within the framework of this thesis are summarized. Note that all can be regarded as vibrators, with ^{144}Xe being in the beginning of the transitional region between vibrators and rotors. Other key observables for studying the evolution of

Energy Ratios of Nuclei of Interest

Isotope	$E(2_1^+)$ $[keV]$	$E(4_1^+)$ $[keV]$	$\mathcal{R}_{42}$
^{122}Cd	569.45	1329.15	2.33
^{124}Cd	612.8	1385.1	2.26
^{126}Cd	652.0	1467.0	2.25
^{138}Xe	588.83	1072.53	1.82
^{140}Xe	376.66	834.29	2.21
^{142}Xe	287.2	690.7	2.40
^{144}Xe	252.6	644.3	2.55

Table 1.1: The energies of the first excited 2^+ and 4^+ states and the ratio $\mathcal{R}_{42}$ of these for the isotopes under investigation.

nuclear structure are the energy of the first excited state and the transition strength to it. As stated above, even-even nuclei are well suited for investigating the evolution of

collectivity. The first excited state is then the 2_1^+ state and the strength of the $0_1^+ \rightarrow 2_1^+$ transition is expressed in terms of the reduced $E2$ matrix element (see chapter 2 for details):

$$B(E2 : J_i \rightarrow J_f) = \frac{1}{2J_i + 1} |\langle \Psi_f || E2 || \Psi_i \rangle|^2. \tag{1.8}$$

In figure 1.5 the $B(E2)$ values as well as the energies of the first excited 2_1^+ state for isotopes around the neutron shell closure $N = 82$ are shown. As expected, the energy of the first excited state is increasing towards the closed shell and the probability to excite a nucleus is increasing with the number of valence nucleons available to create the excited state. Note that two contradicting $B(E2)$ values for ^{140}Xe exist in the literature. The value of $B(E2) = 0.324\ e^2b^2$ has been published in Cheifetz et al. (1980) whereas the higher value of $B(E2) = 0.547\ e^2b^2$ has been determined from a lifetime measurement by Lindroth et al. (1999). The general trend that an increasing $E(2_1^+)$ is accompanied by a decreasing transition strength, i.e. $B(E2) \propto 1/E(2_1^+)$, can be derived from the liquid drop model for vibrational states (see Ring and Schuck (2000)). The systematic behaviour of these two observables has originally been studied by Grodzins (1962) for a wide range of even-even nuclei. Further refinement has been done by Raman et al. (2001) and Habs et al. (2002), resulting in a phenomenological rule that states that the product of $B(E2)$ and $E(2_1^+)$ depends only on powers of Z and A:

$$E(2_1^+) \cdot B(E2; 0^+ \rightarrow 2^+) = 3.242 \cdot Z^2 A^{-2/3} \cdot [1.000 - 0.0608(N - \bar{N})]. \tag{1.9}$$

Here, Z denotes the charge number, N the neutron number and $A = Z + N$ the mass number of the nucleus under investigation. The term $(N - \bar{N})$ is a measure for the neutron excess of the isotope with $\bar{N}$ being the neutron number for which the nuclear mass reaches its minimum within an isobaric chain. The parameters have been fitted to values known for nuclei with $48 \leq Z \leq 70$ and $\mathcal{R}_{42} \geq 1.8$. In this thesis eq. 1.9 will referred to as *modified Grodzins rule*.

1.4 Nuclei far from Stability

When going away from stability to nuclei with extreme N/Z ratios new phenomena can occur, either due to changes of the spin-orbit coupling or due to residual interactions which become stronger. Among the latter, the so-called *tensor force* (i.e. a spin-isospin dependent part of the nucleon-nucleon interaction) has been recognized to play a major role for the evolution of shell structure towards exotic nuclei.

Otsuka et al. (2001) showed that the tensor force can change the shell structure significantly for nuclei with large N/Z ratios. His calculations showed that the well-known $N = 20$ shell gap at $Z \approx 14$ decreases and even disappears when going to smaller charge numbers and a new magic number $N = 16$ appears at $Z = 8$, predicting ^{24}O to be a doubly-magic nucleus. This has just recently been confirmed experimentally (Kanungo et al., 2009)).

The tensor force has also been shown to modify nuclear shell structure throughout the nuclear chart (Otsuka et al., 2005) and to cause a reduction of the spin-orbit

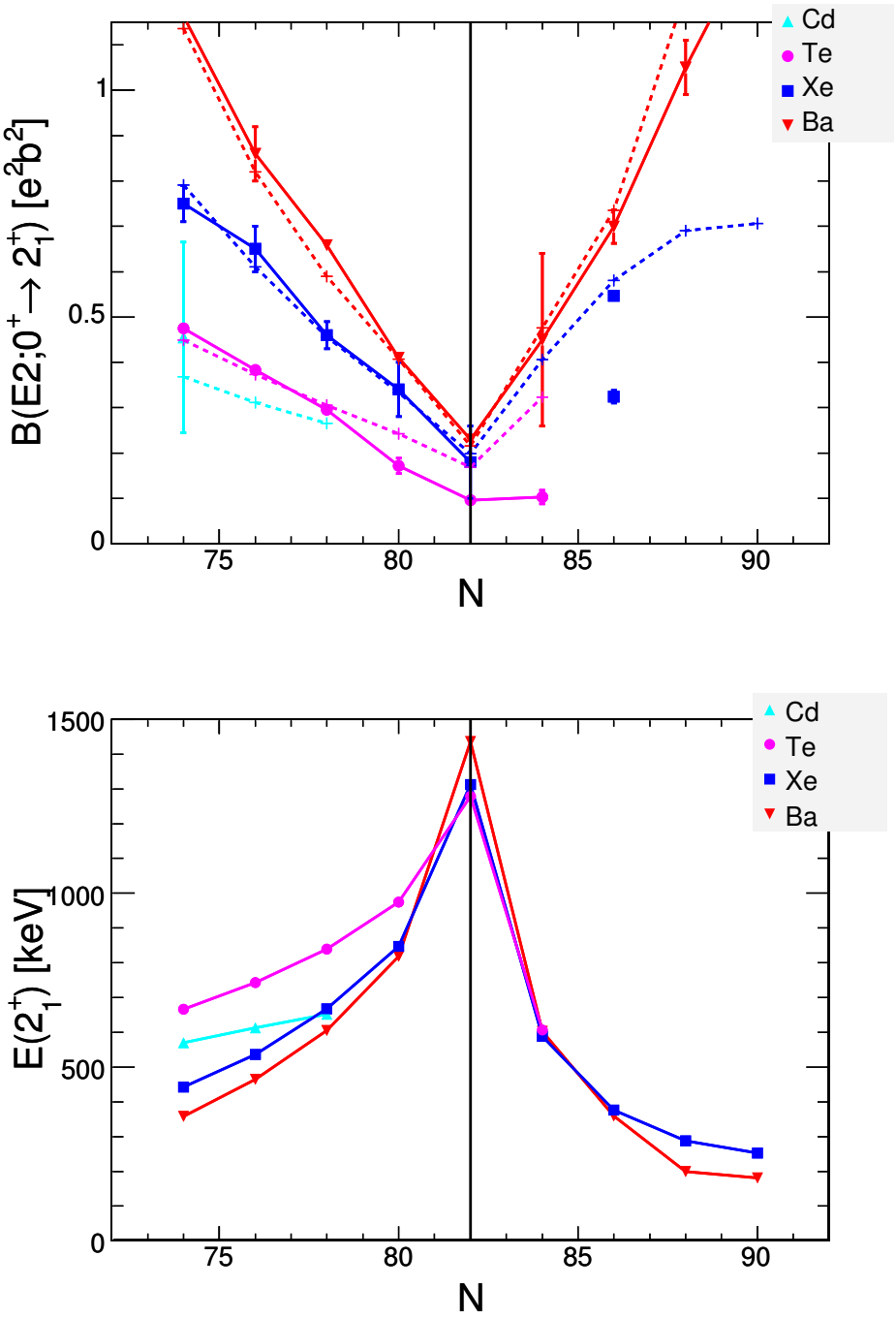

Figure 1.5: Top: The $B(E2)$ values for selected isotopes around $N = 82$ are shown along with the values derived from the modified Grodzins rule (dashed lines; see text for details). Bottom: The energies of the first excited state in the same selection of isotopes. The lines emphasize the systematic distribution around the shell closure.

splitting with increasing neutron excess (Otsuka et al., 2006). The latter can also be explained by a larger surface diffusiveness in neutron-rich exotic nuclei.

Schiffer et al. (2004) have shown that the spin-orbit splitting is decreasing with increasing neutron excess by comparing the binding energies of the last proton outside the closed shell in $Z = 51$ nuclei and the binding energy of the last neutron in $N = 83$ isotones. The question whether this is due to the tensor force or due to a surface effect remains open. Probing the stability of shell closures in exotic nuclei has therefore become one of the major issues in nuclear structure physics.

As mentioned before, the nucleosynthesis processes slow down at nuclei with closed neutron shells due to their low neutron absorption cross sections. These particular nuclei are called *waiting-point* nuclei. Since the r-process involves very neutron-rich nuclei, its modeling is very sensitive to changes in the shell structure in that region of the nuclear chart. β- and γ-spectroscopic decay studies of the $N = 82$ r-process waiting-point nucleus ^{130}Cd performed at ISOLDE (see chapter 3) showed evidence for the theoretical predicted $N = 82$ shell quenching (cf. Dillmann et al. (2003)) whereas recent observation of the γ-decay of excited states in ^{130}Cd at GSI did not show signs for this shell quenching (Jungclaus et al., 2007).

The region around $N = 82$ has also drawn attention since the measurement of the $B(E2)$ values of ^{132,134,136}Te by Radford et al. (2002). As can be seen in figure 1.5 these values deviate significantly from the prediction of the modified Grodzins rule. It is especially the very low $B(E2)$ value of the $N = 84$ nucleus ^{136}Te that is puzzling as its corresponding 2_1^+ energy drops as much as those of the other isotopes shown. It would be expected that a decreasing $E(2_1^+)$ goes along with an increasing $B(E2)$ value. The anomalous behaviour in the Te isotopes has been explained with a reduced neutron pairing above the $N = 82$ shell closure by Terasaki et al. (2002).

In order to shed further light on the behaviour of $B(E2)$ values around $N = 82$, hence probing the stability of the shell closure and the evolution of collectivity around it, a systematic study of $B(E2)$ values both below and above the shell gap seems necessary. In this thesis, the measurement of $B(E2)$ values for $^{122-126}$Cd as well as for $^{138-144}$Xe by means of Coulomb excitation experiments is reported.

In chapter 2 the theoretical framework of Coulomb excitation along with its application to this work is explained. The experimental setup is described in chapter 3 and the process of data analysis for all reactions can be found in chapter 4. The results are summarized and discussed in chapter 5.

—For knowledge, too, itself is power.
Francis Bacon (1561-1626)

2
Coulomb Excitation

The possibility of exciting nuclei by the long-range electromagnetic interaction was calculated and realized already in the 1930s (Weisskopf, 1938). A major impetus to Coulomb excitation experiments occurred, however, with the suggestion of the nuclear rotational and vibrational model by Bohr and Mottelson in 1952 (Bohr and Mottelson, 1975). Experimental evidence even preceded this suggestion, but was unrecognized as such until repeated with several different nuclei (McClelland and Goodman, 1953). Since then, Coulomb excitation developed into an important tool for investigating low-lying nuclear states. In the case of pure (or *safe*) Coulomb excitation, the only nuclear properties which enter into the theory are the matrix elements of the electromagnetic multipole moments of the initial and final states involved in the transition. Hence, one of the great advantages of Coulomb excitation is that it depends solely on the electromagnetic coupling, which is one of the best understood phenomena in present day physics.

2.1 Semi-Classical Treatment

In the semi-classical picture the relative motion of the nuclei is treated classically whereas the excitation process is treated quantum mechanically. Therefore, the projectile travels along a hyperbolic orbit which can be described by the charge numbers, the energy and the scattering angle ϑ. The distance between projectile and target for a **C**enter-of-**M**ass (CM) scattering angle ϑ is given by

$$b(\vartheta) = a_0 \left(1 + \frac{1}{sin(\vartheta/2)}\right) \tag{2.1}$$

with $a_0 = \frac{Z_1 Z_2 e^2}{2E_{CM}}$ and $E_{CM} = \frac{1}{2}\mu v_\infty^2 = \frac{A_2}{A_1+A_2}E_1$ the energy of the reaction in the CM system[1] (cf. figure 2.1). Here, the subscript 1 (2) denotes variables belonging to the projectile (target). A sufficient requirement for ensuring that the projectile does not

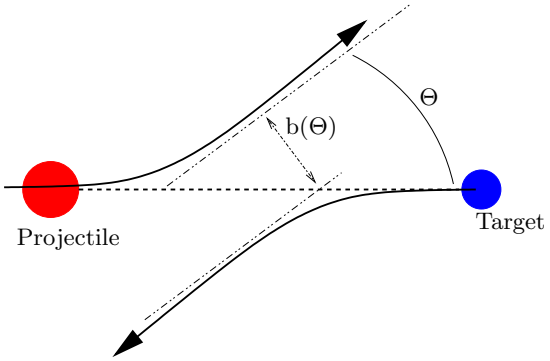

Figure 2.1: Coulomb Scattering in the Center-of-Mass System

penetrate the target nucleus (*safe Coulomb excitation*) is that its deBroglie wavelength $\bar{\lambda}$ is smaller than half the distance of closest approach:

$$\frac{b(\vartheta = 180°)}{2\bar{\lambda}} = \frac{Z_1 Z_2 e^2}{\hbar v_\infty} =: \eta \gg 1. \tag{2.2}$$

The parameter η is called *Sommerfeld parameter* (Sommerfeld, 1931). The differential cross section for exciting a nucleus from an initial state $|i\rangle$ to a final state $|f\rangle$ is given by

$$\left(\frac{d\sigma}{d\Omega}\right)_{if} = \left(\frac{d\sigma}{d\Omega}\right)_{Ruth} \cdot P_{if}$$

where P_{if} is the transition probability and $\left(\frac{d\sigma}{d\Omega}\right)_{Ruth} = \left(\frac{a_0}{2}\right)^2 sin^{-4}(\vartheta/2)$ is the well-known Rutherford cross section. The excitation process can be described with the time dependent Schrödinger equation

$$i\hbar\frac{\partial}{\partial t}|\Psi(t)\rangle = \{H_0 + V(\vec{r}(t))\}|\Psi(t)\rangle \tag{2.3}$$

where $V(\vec{r}(t))$ is the operator of the electromagnetic interaction and H_0 the Hamiltonian of the free nucleus. Solving this equation with the initial condition that at $t = -\infty$ the nucleus is in its ground state, i.e. $|\Psi(-\infty)\rangle = |0\rangle$, leads to the wave function of the nucleus after the collision:

$$\Psi(\vec{r}, t) = \sum_f \alpha_{if}(t)\Psi_f(\vec{r}) = \sum_f \alpha_{if}(t)|f\rangle. \tag{2.4}$$

Here, the sum is over all possible final states and the coefficients α_{if} are the excitation amplitudes. The probability for a transition $|i\rangle \to |f\rangle$ is then

$$P_{if} = |\alpha_{if}|^2. \tag{2.5}$$

[1] μ is the reduced mass of the target and projectile nuclei, v_∞ denotes the relative velocity of these at large distances.

So far the energy loss

$$\Delta E = E_f - E_i$$

has been neglected. For the validity of the semi-classical picture it has to be shown that this energy loss does not modify the orbit significantly, i.e. $\Delta E/E_{CM} \ll 1$. A nucleus can only be excited to the state $|f\rangle$ if the collision time $\tau_{col} = a_0/v$, i.e. the time it takes the projectile to travel the distance of closest approach, is shorter or equal to the excitation time $\tau_{exc} = \hbar/\Delta E$. This can be described by the *adiabaticity parameter* ξ:

$$\xi = \frac{\tau_{col}}{\tau_{exc}} = \frac{a_0 \Delta E}{\hbar v} \leq 1. \tag{2.6}$$

If the collision time is longer the nucleus is able to follow the perturbation caused by $V(\vec{r}(t))$ adiabatically and the excitation probability decreases exponentially with ξ. The abovementioned energy loss can now be rewritten as

$$\Delta E/E_{CM} = 2\xi/\eta.$$

If $\eta \gg 1$ and $\xi \leq 1$ the usage of the semi-classical picture is reasonable. In a similar manner it can be shown that the angular momentum transfer does not alter the orbit significantly. The total orbital angular momentum can be written as $l \approx \mu v a_0 = \hbar\eta$ and the difference before and after the collision is given by $\Delta l = L\hbar$ (here, L is the multipolarity of the transition). Hence, $\Delta l/l \ll 1$ is automatically fulfilled for safe Coulomb excitation. In table 2.1 the values of the relevant parameters for the different experiments performed in the framework of this thesis are given. Since the scattering

Coulomb Excitation Reaction Parameters

Reaction	η	ξ	$\Delta_{min}[fm]$	$\frac{\Delta E}{E_{CM}}[10^{-3}]$
^{108}Pd(^{122}Cd,^{122}Cd)^{108}Pd	206	0.36	9.1	3.5
^{104}Pd(^{124}Cd,^{124}Cd)^{104}Pd	206	0.39	10.6	3.8
^{96}Mo(^{138}Xe,^{138}Xe)^{96}Mo	212	0.39	8.9	3.6
^{96}Mo(^{140}Xe,^{140}Xe)^{96}Mo	212	0.25	8.8	2.3
^{96}Mo(^{142}Xe,^{142}Xe)^{96}Mo	212	0.19	8.6	1.8
^{96}Mo(^{144}Xe,^{144}Xe)^{96}Mo	218	0.18	11.4	1.6
^{64}Zn(^{124}Cd,^{124}Cd)^{64}Zn	135	0.34	7.3	5.1
^{64}Zn(^{126}Cd,^{126}Cd)^{64}Zn	135	0.37	7.2	5.4

Table 2.1: Relevant parameters for the experiments described in this work (see text for details). The minimum distance Δ for the experimental range in ϑ is given.

process is treated semi-classically the condition for safe Coulomb excitation can be interpreted geometrically such that the nuclei should always be kept at a certain *safety distance* Δ of at least ≈ 5 fm (Wilcke et al., 1980). This is fulfilled if always

$$b(\vartheta) \geq R_1 + R_2 + \Delta$$

with $R_i = 1.25 A_i^{1/3} fm$ (i=1,2). In figure 2.2 it is shown that in the experiments described in this work the safety distance is always larger than 7 fm.

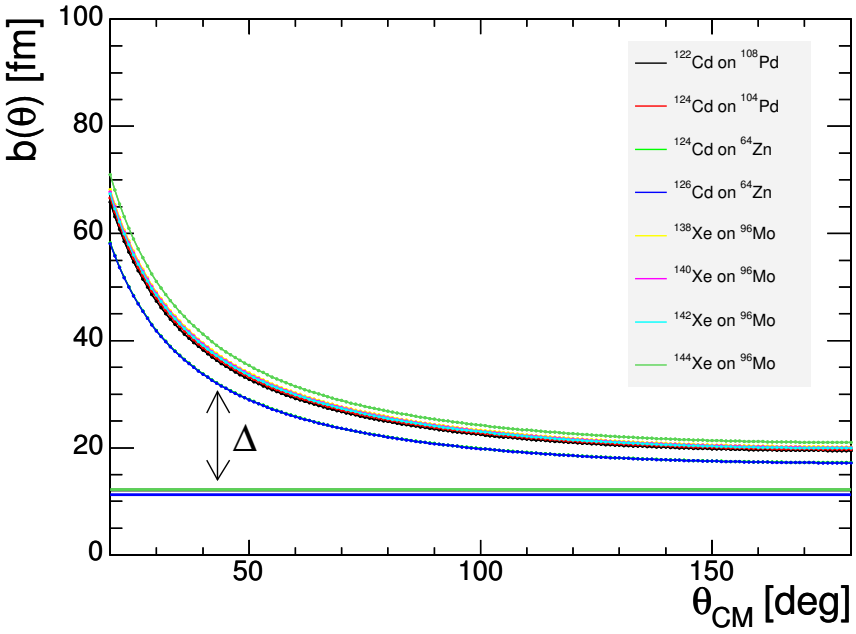

Figure 2.2: The distance $b(\vartheta)$ and $R_1 + R_2$ for the different experiments is shown. It can be seen that the distance Δ is always larger than 5 fm.

2.2 First Order Perturbation Theory

The strength of the interaction potential $V(\vec{r}(t))$ between projectile and target can be expressed in terms of the matrix elements of the *action integral* (measured in units of $\hbar$ (Alder and Winther, 1975)):

$$\begin{aligned} \chi_{if}(\vartheta) &= \langle f| \int_{-\infty}^{+\infty} V(\vec{r}(t))dt|i\rangle \\ &\approx \langle f|V(b(\vartheta))|i\rangle \tau_{col} \end{aligned} \tag{2.7}$$

which has been estimated by the value of V at closest approach and the collision time. It is convenient to define this parameter for $\vartheta = \pi$ as

$$\chi_{if} = \pm\sqrt{P_{if}(\vartheta = \pi, \xi = 0)}.$$

If this parameter is small compared to unity, i.e. if the interaction V is weak, the excitation amplitudes can be calculated using a first-order perturbation approximation. They are then given by

$$\alpha_{if} = \frac{1}{i\hbar} \int_{-\infty}^{+\infty} \langle f|V(\vec{r}(t))|i\rangle exp(i\omega t)dt \tag{2.8}$$

with $\Delta E = \hbar\omega$. The electromagnetic interaction between target and projectile can be decomposed in its multipole components. The monopole-monopole part leads to elastic (or Rutherford) scattering whereas the monopole-multipole and multipole-multipole

components induce inelastic scattering and hence the excitation of the nuclei. Correspondingly the parameter χ can be decomposed into partial sums

$$\chi = \sum_L \chi^{(L)},$$

where each term belongs to the part of $V(\vec{r})$ which has multipole order L. The excitation amplitudes are then factorized into a part that depends only on the matrix elements of the multipole components and a part that depends only on the parameters of the classical orbit. It can be shown (Alder and Winther, 1975) that

$$\alpha_{if} \propto \sum_{L,M} \frac{1}{2L+1} \langle i|\mathcal{M}(EL,M)|f\rangle^* R_{EL}(\vartheta,\xi) \tag{2.9}$$

for electric excitation. Here, the dimensionless orbital integrals $R_{EL}(\vartheta,\xi)$ have been introduced. These depend on the adiabaticity parameter ξ and will vanish in the adiabatic limit $\xi \gg 1$ as $R_{EL} \propto exp(-\xi)$. They measure the excitation probability relative to the case of $\vartheta = \pi$ and $\xi = 0$. The matrix elements are defined generally as

$$\mathcal{M}(EL,M) = \int \rho(\vec{r}) r^L Y_{L,M}(\hat{r}) d^3r \tag{2.10}$$

with $\rho(\vec{r})$ the charge density and $Y_{L,M}$ the spherical harmonics. With the definition of the reduced transition probability (see eq. 1.8)

$$\begin{aligned} B(EL; J_i \to J_f) &= \sum_{M,M_f} |\langle J_f M_f|\mathcal{M}(EL,M)|J_i M_i\rangle|^2 \\ &= \frac{1}{2J_0+1} |\langle J_f||\mathcal{M}(EL)||J_i\rangle|^2 \end{aligned} \tag{2.11}$$

the differential cross section turns out to be

$$d\sigma_{EL} = \left(\frac{Z_1 e}{\hbar v}\right)^2 a_0^{-2L+2} B(EL) df_{EL}(\vartheta,\xi). \tag{2.12}$$

The function df_{EL} holds the relation $df_{EL} \propto R_{EL}^2(\vartheta,\xi) sin^{-4}(\vartheta/2) d\Omega$. The total electric excitation cross section is then given by

$$\sigma_{EL} = \left(\frac{Z_1 e}{\hbar v}\right)^2 a_0^{-2L+2} B(EL; J_i \to J_f) f_{EL}(\xi). \tag{2.13}$$

2.3 Higher-order Perturbation Theory

If the parameter χ is larger than or comparable to unity the Coulomb excitation process must be treated by directly solving the time dependent Schrödinger equation (eq. 2.3). However, in practice the deviation from first-order can often be described by second order corrections. The perturbation expansion is a series expansion in χ and is expected

to converge for χ at most of the order of 0.5. The excitation amplitudes α_{if} are then given by (Alder and Winther, 1975)

$$\alpha_{if} = \alpha_{if}^{(1)} + \sum_z \alpha_{izf}^{(2)} \tag{2.14}$$

where the first term is the known first-order excitation amplitude and

$$\alpha_{izf}^{(2)} = \left(\frac{1}{i\hbar}\right)^2 \int_{-\infty}^{+\infty} \langle f|V(\vec{r}(t))|z\rangle exp(i\omega t)dt \times \int_{-\infty}^{t} \langle z|V(\vec{r}(t'))|i\rangle exp(i\omega' t')dt' \tag{2.15}$$

with $\hbar\omega = E_f - E_z$ and $\hbar\omega' = E_z - E_i$. Here, a summation over a complete set of intermediate nucular states $|z\rangle$ is performed. Two cases of second order effects are worth mentioning here:

Two Step Excitation

The final state $|f\rangle$ may be excited directly or through a low-lying state $|z\rangle$ (cf. figure 2.3). In practice, a two-step excitation is realized if the direct excitation $|i\rangle \rightarrow |f\rangle$ is small or forbidden, i.e. $\chi_{if} << \chi_{iz} \cdot \chi_{zf}$. An interesting case is that of a two-step excitation from the 0^+ ground state to a 4^+ state through an intermediate 2^+ state. Since the direct excitation can only take place via an $E4$ transition - which is usually quite weak - the two-step excitation process strongly dominates. The excitation probability is then $P_{if}^{(2)} \propto |\chi_{iz}^{(2)}|^2 \cdot |\chi_{zf}^{(2)}|^2$.

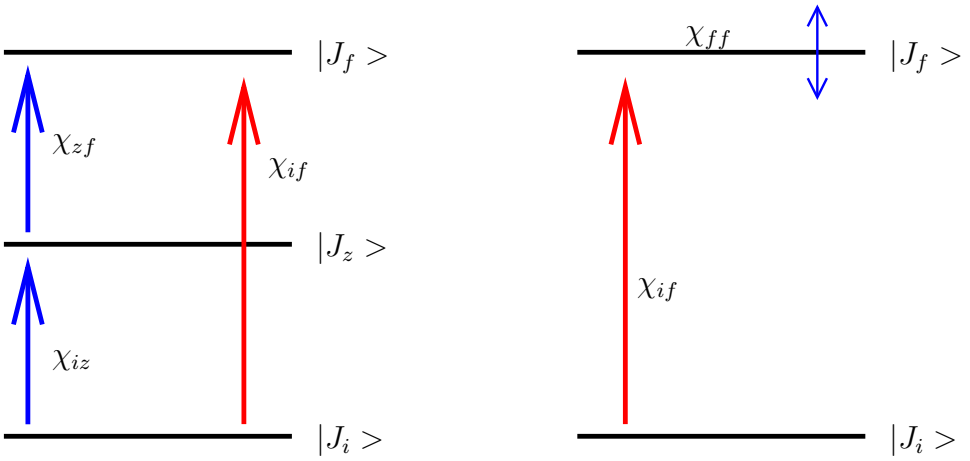

Figure 2.3: Left: Schematic view of a two-step excitation through an intermediate state $|z\rangle$. Right: If the intermediate state is identical to the final state transitions between the magnetic substates of $|f\rangle$ are taken into account by the diagonal matrix element (see text for details).

Reorientation Effect

In cases where the intermediate state is identical to the initial or final state an interaction with the quadrupole moment of that state occurs (cf. figure 2.3 (right)). Considering the excitation of a 2^+ state in an even-even nucleus the strength of this

interaction depends on $\chi^{(2)}_{2\to 2}$. This property is proportional to the intrinsic quadrupole moment Q_0 of the 2^+ state:

$$\chi^{(2)}_{2\to 2} = \frac{4}{15}\sqrt{\frac{\pi}{5}}\frac{Z_1 e}{\hbar v}\frac{1}{a_0^2}\langle 2||\mathcal{M}(E2)||2\rangle \quad \text{with} \tag{2.16}$$

$$\langle 2||\mathcal{M}(E2)||2\rangle = \sqrt{\frac{7}{2\pi}}\frac{5}{4}eQ_0. \tag{2.17}$$

Note that the quadrupole moment is related to the deformation parameter β (see section 1.2) via

$$eQ_0 = \frac{3}{\sqrt{5\pi}}ZR_0^2 e\left(\beta + 0.16\beta^2\right). \tag{2.18}$$

A positive deformation parameter $\beta > 0$ corresponds to *prolate* deformation whereas a negative value $\beta < 0$ corresponds to *oblate* deformation.

The change in the angular distribution of the γ-rays resulting from the second-order treatment is caused by transitions between different magnetic substates of the excited state. The excitation probability in second order is then given by (Schwalm et al., 1972; Alder and Winther, 1975)

$$P^{(2)}_{02} = P^{(1)}_{02}(1 + qK(\xi, \vartheta)) \tag{2.19}$$

with

$$q = \frac{\mu\Delta E}{Z_2}\langle 2||\mathcal{M}(E2)||2\rangle \tag{2.20}$$

and $P^{(1)}_{02}$ the excitation probability in first order. For projectile excitation, Z_2 has to be replaced by Z_1. The excitation energy ΔE is given in MeV, while the reduced matrix element $\langle 2||\mathcal{M}(E2)||2\rangle$ is given in $e \cdot b$. The quantity $K(\xi, \vartheta_1)$ depends only slightly on the adiabaticity parameter ξ, but increases significantly with increasing scattering angle. Typical values for K are of the order of unity.

2.4 Application to Experiment

The aim of the experiments described in this work is to determine the $B(E2)$ values for the $0^+_1 \to 2^+_1$ and – in some cases – also the $2^+_1 \to 4^+_1$ transitions of the projectile nuclei. This has been achieved by measuring the gamma yields N_γ following the corresponding disexcitation of both the projectile and the target nucleus. This gamma yield is

$$N^{(1),(2)}_\gamma \propto \sigma^{(1),(2)}_{ce} \cdot \epsilon^{(1),(2)}_\gamma \cdot I_{Beam}$$

with ϵ_γ being the total photopeak efficiency of the gamma detector array and I_{Beam} the beam intensity. A relative measurement of the Coulomb excitation cross section of the projectile nucleus to the known cross section for target excitation reduces the systematic error stemming from uncertainties in these factors. The projectile excitation

cross section is then given by:

$$\sigma_{ce}^{(1)} = \frac{N_\gamma^{(1)}}{N_\gamma^{(2)}} \times \frac{\epsilon_\gamma^{(2)}}{\epsilon_\gamma^{(1)}} \times \sigma_{ce}^{(2)} \quad \text{and} \tag{2.21}$$

$$\frac{\Delta\sigma_{ce}^{(1)}}{\sigma_{ce}^{(1)}} = \sqrt{\left(\frac{\Delta N_\gamma^{(1)}}{N_\gamma^{(1)}}\right)^2 + \left(\frac{\Delta N_\gamma^{(2)}}{N_\gamma^{(2)}}\right)^2 + \left(\frac{\Delta\sigma_{ce}^{(2)}}{\sigma_{ce}^{(2)}}\right)^2}. \tag{2.22}$$

The variables $N_\gamma^{(1),(2)}$ and $\epsilon_\gamma^{(1),(2)}$ can be extracted from the experiment (see also section 3.5 and chapter 4). Note that the uncertainties in the photopeak efficiency are of the order of $\frac{\Delta\epsilon_\gamma}{\epsilon_\gamma} \sim 10^{-3}$ whereas the uncertainties in σ_{ce} and N_γ are 1-2 orders of magnitude larger. Therefore, the contribution of $(\Delta\epsilon/\epsilon)^2$ has been neglected here. Since the target matrix elements - and therefore its Coulomb excitation cross section $\sigma_{ce}^{(2)}$ - are known, it is now possible to determine the projectile Coulomb excitation cross section $\sigma_{ce}^{(1)}$. This cross section has to be reproduced by a theoretical calculation performed with the code CLX (see section 2.6) depending on the matrix elements as input parameters. Therefore, the $B(E2)$ values of interest can be determined via linear interpolation between calculated cross sections $\sigma_{CLX}^{(1)}$ for different matrix elements. These calculations have to be corrected for the non-isotropic angular distribution of γ-rays (see section 2.5). Of course, in eq. 2.21 it is assumed that only the isotope of interest is responsible for target excitation. For possible beam contaminations the gamma yield $N_\gamma^{(2)}$ has to be corrected.

2.5 Angular Distribution

Since the magnetic substates of $|f\rangle$ are not populated equally in Coulomb excitation, the emission of γ-rays is non-isotropic. A detailed discussion on the γ-ray angular distribution can be found in Alder et al. (1956) or Alder and Winther (1975). Here, the results concerning the experiments in this work are described. It can be shown that the angular distribution of the emitted γ-rays can always be written in the form

$$\begin{aligned} W(\theta_\gamma, \phi_\gamma) &= \sum_{k,k'} A_{kk'}^*(\vartheta) Y_{kk'}(\theta_\gamma, \phi_\gamma) \\ \text{with} \qquad A_{kk'}^*(\vartheta) &= \sum_{\kappa,\kappa'} \rho_{\kappa\kappa'}^C(\vartheta) K_{kk',\kappa\kappa'} \end{aligned} \tag{2.23}$$

and ϑ being the scattering angle of the emitting particle. $Y_{kk'}(\theta_\gamma, \phi_\gamma)$ are the spherical harmonics, $\rho_{\kappa\kappa'}^C(\vartheta)$ is a statistical tensor which is the equivalent to the density matrix $\rho_{\kappa\kappa'}^C \propto \langle f|\rho|i\rangle$. $K_{kk',\kappa\kappa'}$ describes the effects of unobserved γ-rays, conversion electrons and other attenuating factors. If the particle is detected in a ring counter the angular distribution is independent of ϕ_γ. For the case of an $E2$ transition the above formula simplifies to

$$W_{E2}(\theta_\gamma) = 1 + a_2 P_2(cos\theta_\gamma) + a_4 P_4(cos\theta_\gamma) \tag{2.24}$$

with $P_n(cos\theta_\gamma)$ being the Legendre polynomials.

Deorientation

An important phenomenon concerning the angular distribution of disexcitation γ-rays is the nuclear deorientation effect. The initial nuclear alignment produced via Coulomb excitation may not be retained during the lifetime of the nuclear state. Hence, an attenuation of the angular distribution can be caused by hyperfine interactions between the nucleus and the surrounding electron configuration. This leads to a modification of eq. 2.24 by introducing time-dependent attenuation factors:

$$W_{E2}(\theta_\gamma, t) = 1 + a_2 G_2(t) P_2(cos\theta_\gamma) + a_4 G_4(t) P_4(cos\theta_\gamma). \tag{2.25}$$

Assuming that the mean time between fluctuations of the electron configuration is small compared to the lifetime of the nuclear state τ_N and small compared to the precession time of the nuclear magnetic moment Abragam and Pound (1953) introduced the following parametrization for these attenuation factors:

$$G_k(t) = \exp\left[-\lambda_k t\right] \quad \text{and} \tag{2.26}$$

$$G_k = \int_0^\infty e^{-t/\tau_N} G_k(t) dt/\tau_N = \frac{1}{1+\lambda_k \tau_N}. \tag{2.27}$$

The integrated attenuation factors can be expressed in terms of a single relaxation time scale

$$\tau_2 = \lambda_2^{-1} \propto \frac{1}{g^2 \mu_N^2 \langle H^2 \rangle^{1/2}}$$

with H being the magnetic field at the nucleus (cf. Danchev et al. (2005)). They are then given by

$$G_2 = \frac{\tau_2}{\tau_2 + \tau_N} \quad \text{and} \quad G_4 = \frac{0.3\tau_2}{0.3\tau_2 + \tau_N}. \tag{2.28}$$

In this work eq. 2.25 has been taken into account by means of the parameter λ_2 as input parameter for the coupled-channel code CLX (see section 2.6).

2.6 Coulomb Excitation Calculations with CLX

The Coulomb excitation calculations for this thesis were performed using the coupled-channel code CLX, originally written by H. Ower, adapted by J. Gerl and further modified by Th. Kröll. This code was used to calculate the differential and integrated excitation cross sections of the projectile and target nuclei. It follows the nomenclature of Alder and Winther (1975).

Its input parameters include

- the charge and mass numbers Z,A of the projectile and target nuclei
- the number of states involved in the calculation
- the spin, parity and energy for each of these states
- the beam energy
- the range in ϑ_p over which to integrate the cross section

- the transitions $|i\rangle \rightarrow |f\rangle$ under consideration together with their matrix elements ME($i \rightarrow f$) and their multipolarities[2]
- the positions(s) of the gamma detector(s)
- the conversion coefficients taken from Hager and Seltzer (1968)

The output of CLX provides the user with integrated as well as differential excitation cross sections for all transitions under consideration, possibly normalized to the corresponding Rutherford cross section. It is further possible to define *windows* in the particle scattering range over which to integrate the Coulomb excitation cross sections. In figure 2.4 the calculated Coulomb excitation cross section of ^{96}Mo with respect to ϑ_{CM} is shown. The angular range has been divided in windows of 5° width. The other parameters are taken from the ^{96}Mo(^{140}Xe,^{140}Xe*)^{96}Mo* experiment (see chapter 4).

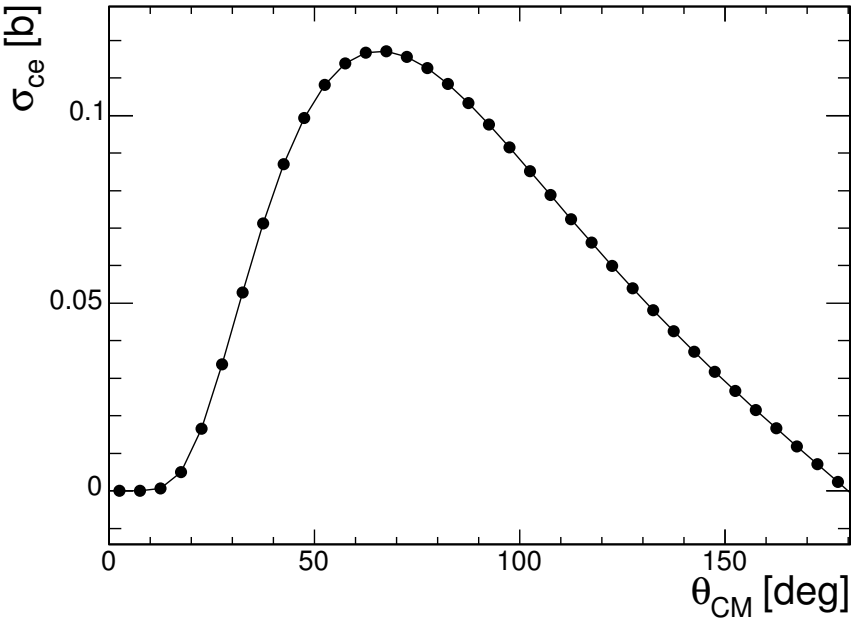

Figure 2.4: The Coulomb excitation cross section for the $0_1^+ \rightarrow 2_1^+$ transition in ^{96}Mo in the CM system.

[2]The nomenclature ME($i \rightarrow f$) is used for the **M**atrix **E**lements $|\langle J_f||\mathcal{M}(E2)||J_i\rangle|$ in this thesis.

—There is nothing new to be discovered in physics now. All that remains is more and more precise measurement.

William Thomson, Lord Kelvin
(1824-1907)

3 Experimental Setup

For the investigation of nuclei far away from stability (*exotic nuclei*) the development of **R**adioactive **I**on **B**eams (RIBs) is necessary. The isotopes of interest are created by nuclear reactions such as fission, fragmentation, spallation and fusion. The latter produces proton-rich nuclei whereas the others can lead to the neutron-rich side of the nuclear chart.

3.1 Methods of Producing RIBs

The development of RIB facilities with reaccelerated beams opened a new field of nuclear physics since the 1990's. Two different techniques of producing RIBs are used in current RIB facilities: (i) the **I**n-**F**light projectile fragmentation (IF) method and (ii) the **I**sotope **S**eparation-**O**n-**L**ine (ISOL) method which is used for the experiments described in this work. These techniques are very complementary regarding, e.g., their energy range.

3.1.1 In-Flight Method

The IF method consists of a high-energy beam of heavy nuclei impinging on a thin ($\sim g/cm^2$) target. Part of the beam particles collide with the target nuclei which leads to projectile fragmentation or fission and other nuclear reactions. The reaction products basically keep the forward momentum of the primary beam. The isotope of interest can be selected by applying electromagnetic and kinematical separators.

The advantage of this method is that the produced nuclei are available almost instantly and without chemical selectivity. Hence, isotopes with lifetimes down to a few μs can be investigated. The beam energy - ranging from about 10 A·MeV up to the order of 1 A·GeV - is well suited for nuclear reaction studies, but makes studies of low-lying nuclear structure or astrophysics experiments very difficult. The beam is also of only modest quality concerning its beam spot size, energy precision and spread and

angular divergence. Facilities which make use of the IF method are e.g. NSCL (USA), GANIL (France), GSI (Germany) or RIKEN (Japan).

3.1.2 Isotope Separation On-Line

The ISOL method uses a light beam (e.g. protons) that impinges on a thick production target. In principle, the same kind of nuclear reactions can take place as above, but this time the reaction products are thermalized in the target. They diffuse out of the target and are ionized, accelerated again and mass separated. Due to the second acceleration a much higher beam quality can be achieved and the beam energy can be varied from a few A·keV up to some A·MeV and higher.

This technique is especially suitable for nuclear structure and astrophysics experiments. The main drawback is the slow release time from the primary target, hence one cannot use this method for isotopes with life times $\tau \leq 10\ ms$. The diffusion out of the target depends also on the chemical properties of the element (e.g. refractory elements do not come out of the source). The ISOL method is used e.g. at ISOLDE (CERN), HRIBF (USA), ISAC (Canada) or SPIRAL (France).

3.2 The ISOLDE Facility

ISOLDE is an on-line isotope separation facility located at CERN[1] with about 40 years of experience in the production of low-energy radioactive ion beams. Today, more than 600 isotopes of more than 60 elements are available.

A beam of 1.4 GeV protons provided by the PSB[2] impinges on a primary target (e.g. UC_x), where fission and spallation takes place. The reaction products diffuse out of the target and are subsequently ionized to a 1^+ state, possibly also as molecules. Different ion sources are used, depending on the element of interest.

After extraction the beam is mass separated and distributed to the different experiments in the hall (see figure 3.1).

3.2.1 The PS Booster

The PS Booster (PSB) is a stack of four small synchrotrons where protons are pre-accelerated before injection into the CERN Proton Synchrotron (PS) (see figure 3.2). The PSB delivers short pulses ($\sim 2.4\mu s$) of high intensity (up to 3.2×10^{13} p/pulse). About six pulses in a PS supercycle of typically 12 pulses are available for ISOLDE which is equivalent to a DC proton current of about $2\mu A$. These protons are then transfered to one of the two target zones of ISOLDE.

3.2.2 Targets and Ion Sources

For the experiments described in this work a UC_x primary target has been used. During the Cd runs, a tungsten rod has been applied close to the target. The protons, now impinging on this so-called *proton-to-neutron converter*, create fast reaction neutrons

[1] **C**onseil **E**uropéen pour la **R**echerche **N**ucléaire
[2] **P**roton **S**ynchrotron **B**ooster

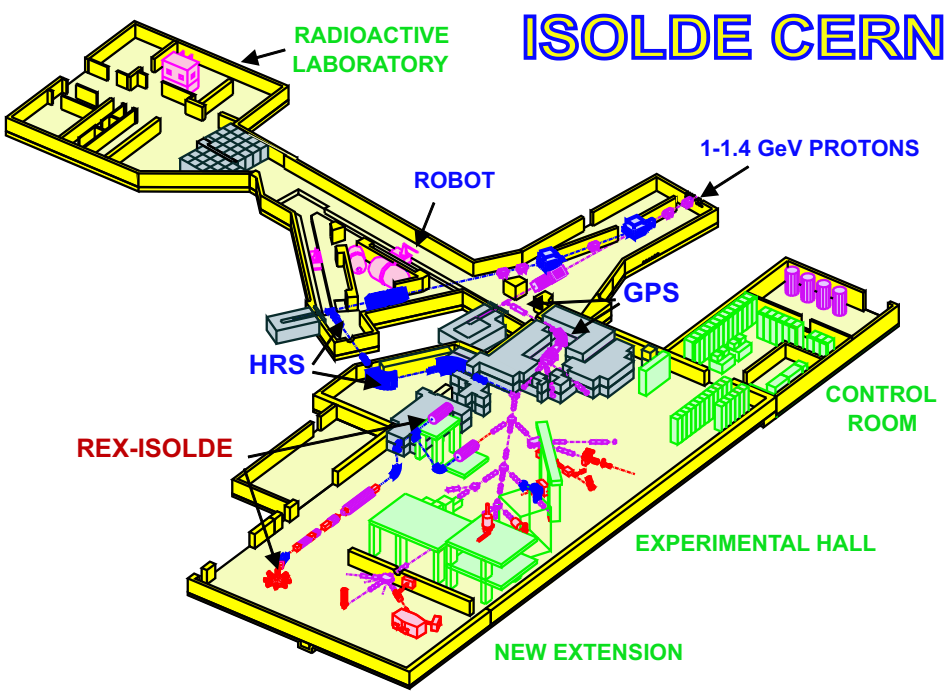

Figure 3.1: View of the ISOLDE experiment hall after 2006 (taken from `http://isolde.web.cern.ch/isolde/`).

which induce fission in the UC_x target. This method helps to suppress proton-rich isobaric spallation products and therefore improves the beam purity.

The diffusion time depends strongly on the chemical properties of the ions of interest and on the target temperature which can be increased up to about $2000°C$. For the subsequent ionization several different ion sources are available at ISOLDE:

Surface Ion Source: The surface ion source is the simplest setup for ionizing atoms produced in the target. It consists only of a tube (*transfer line*) made of a metal which has a higher work function than the atoms ionization potential (e.g. tantalum or tungsten). A more recent development is a transfer line made of quartz, which improved the beam purity during the ^{124,126}Cd experiments described in section 4.2. The transfer line can be heated up to $\sim 2400°C$ to avoid long sticking times of the atoms on the surface and to ensure that ions are repelled from the surface.

Hot Plasma Ion Source: The plasma ion source is used to ionize atoms that cannot be surface ionized. The plasma is produced by a gas mixture (e.g. Ar and Xe) that is ionized by impact of accelerated electrons.

Cold Plasma Ion Source: For the production of noble gas isotopes the above setup is modified such that the transfer line between target and plasma is cooled by a continuous water flow and therefore the isobaric contamination in the ISOLDE ion beams is reduced. This has been used for the Xe beam experiments described in this thesis.

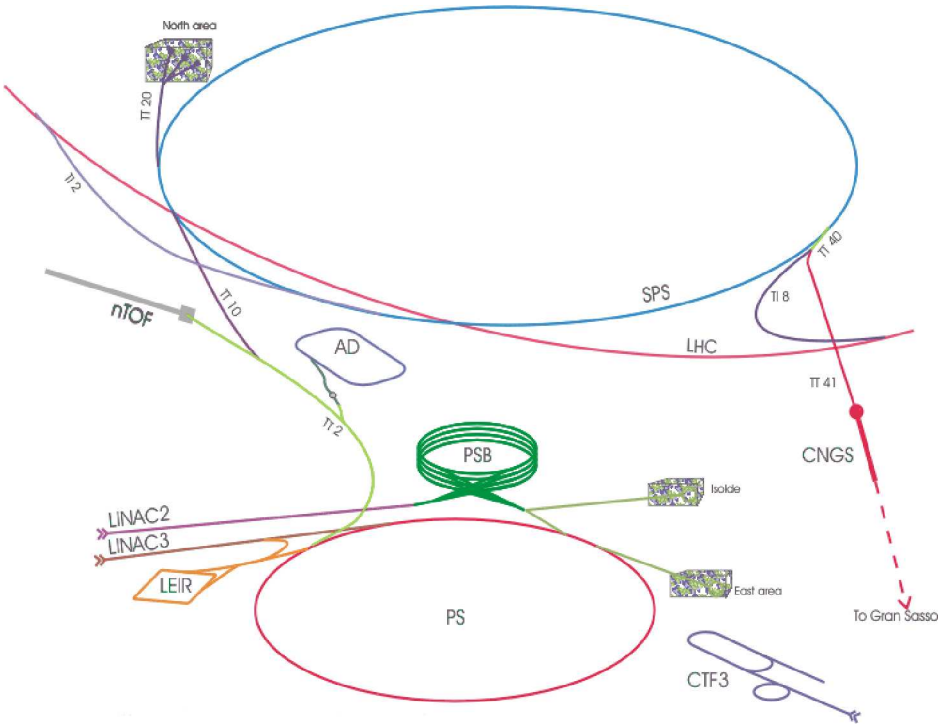

Figure 3.2: Schematic representation of the CERN accelerator complex (taken from `http://isolde.web.cern.ch/isolde/`)

Laser Ion Source: A more sophisticated technique now in use is the **R**esonant **I**onization **L**aser **I**on **S**ource (RILIS). A laser beam is tuned precisely to the energy of a strong atomic transition in the isotope of interest and a second laser beam is used to excite an electron from that state to the continuum. Since the second beam does not have enough energy to excite an electron from the ground state, the RILIS can select not only a specific isotope but even isomeric states. Sometimes, as in the Cd runs described in this work, a 3-step ionization scheme is used where the first two beams excite the isotope of interest from the ground state to subsequently higher lying states and the third beam excites the electron to the continuum (see figure 3.3).

It is possible to operate the RILIS in two different modes: (i) the "laser off" mode, where only surface-ionized contaminants are seen in the beam and (ii) the "laser on" mode, where additionally the laser-ionized isotope of interest is seen. By comparing the data between these two modes the amount and kind of beam contamination can be estimated.

3.2.3 The Mass Separators

After ionization the particles are extracted with typically 60 kV producing a 60 keV beam. For selecting the ions of interest, two different mass separators are available at

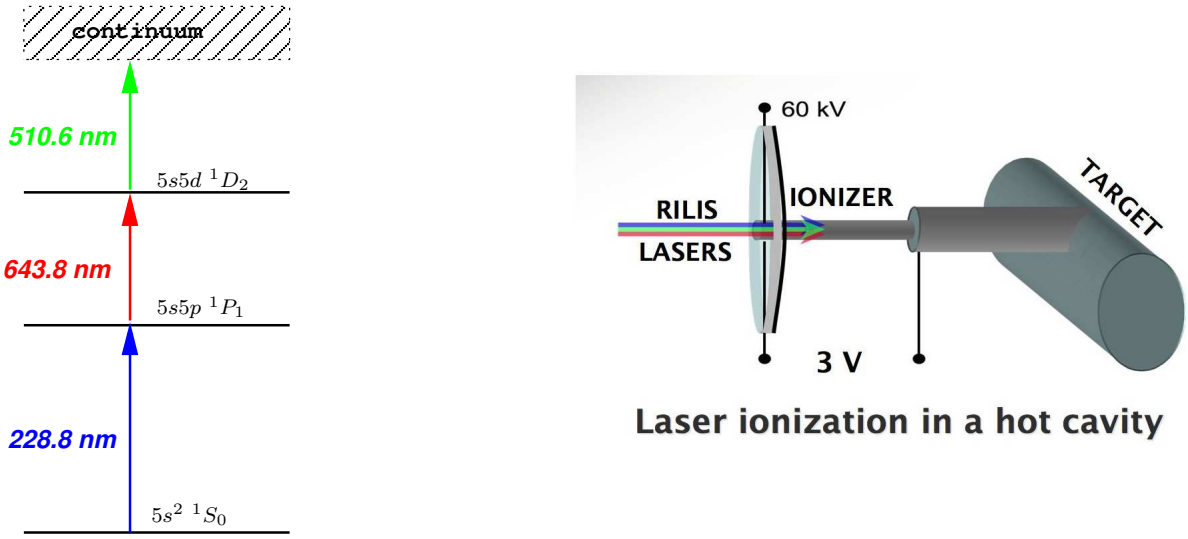

Figure 3.3: Ionization scheme for Cd and schematic view of the RILIS (taken from `http://isolde.web.cern.ch/isolde/`).

ISOLDE, each with its own target. The so-called **G**eneral **P**urpose **S**eparator (GPS) is designed to allow three ion beams within a mass range of $\pm 15\%$ and a mass resolution of $\frac{M}{\Delta M} = 2400$ to be selected and delivered to the experimental hall. The **H**igh-**R**esolution **S**eparator (HRS) is designed for selecting one ion beam with a mass resolution of $\frac{M}{\Delta M} \approx 5000$.

3.3 REX-ISOLDE

The **R**adioactive Beam **EX**periments (REX) facility was developed for bunching, charge breeding and post accelerating the singly ionized RIBs coming from ISOLDE. In the following, the REXTRAP, the EBIS and the REX linac are presented. A detailed description can be found in Ames et al. (2005). A schematic view of its components is shown in figure 3.4.

3.3.1 REXTRAP

The REXTRAP is a Penning trap which was developed for accumulating, bunching and cooling of the singly-charged ions from the separators. Accumulation and bunching is required for the ion injection into the subsequent charge breeder. Since the trap potential is 60 kV, the incoming ions have just enough energy to climb the first potential threshold. Once inside the trap, the ions are slowed down by collisions with a buffer gas (typically Argon or Neon at a pressure of $\sim 10^{-3}$ mbar). After cooling, the ions are extracted to the EBIS in a bunch by lowering the ions potential threshold (see figure 3.5).

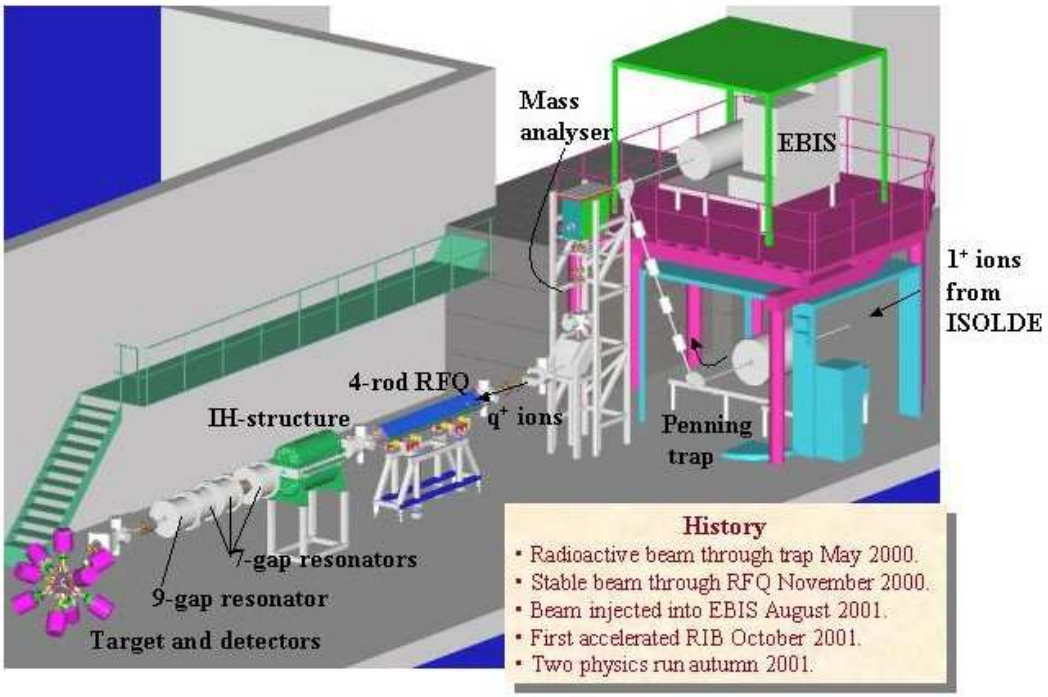

Figure 3.4: Schematic view of the different parts of REX: the incoming beam is first accumulated in the trap, then charge bred in the EBIS and finally reaccelerated in the linac (taken from `http://isolde.web.cern.ch/isolde/`).

3.3.2 EBIS

The singly charged ions from the REXTRAP are injected into the **E**lectron **B**eam **I**on **S**ource (EBIS) in bunches. Inside the EBIS they are confined by the negative space charge of the electrons and by potential barriers established by cylindrical electrodes. For the injection into the linear accelerator (*linac*) a mass-to-charge ratio of $A/q < 4.5$ is required. The trapped ions will therefore undergo stepwise ionization from 1^+ to n^+ via electron impact until a sufficient number of ions has reached this A/q value. For this, a mono-energetic electron beam from an electron gun focused by a strong magnetic field ($\sim$ 2T) is used. The energy of this beam is adjustable between 3 - 6 kV.

For the ionization process, an excellent vacuum ($\sim 10^{-10}$ mbar) inside the EBIS is required. However, residual gas is still often seen as a contaminant in the subsequent experiments. To obtain a high breeding efficiency, the phase space overlap of injected ions and the electron beam has to be large. Hence, a rather low extraction emittance from the Penning trap is needed. Unlike the trap, the potential of the EBIS platform is pulsed between injection and extraction from 60 to about 20 kV, allowing for a fixed ion extraction velocity independent of the A/q-value.

The total breeding time can range from a few to a couple of hundreds of milliseconds. In table 3.1 these parameters are given for the experiments performed in the framework of this thesis.

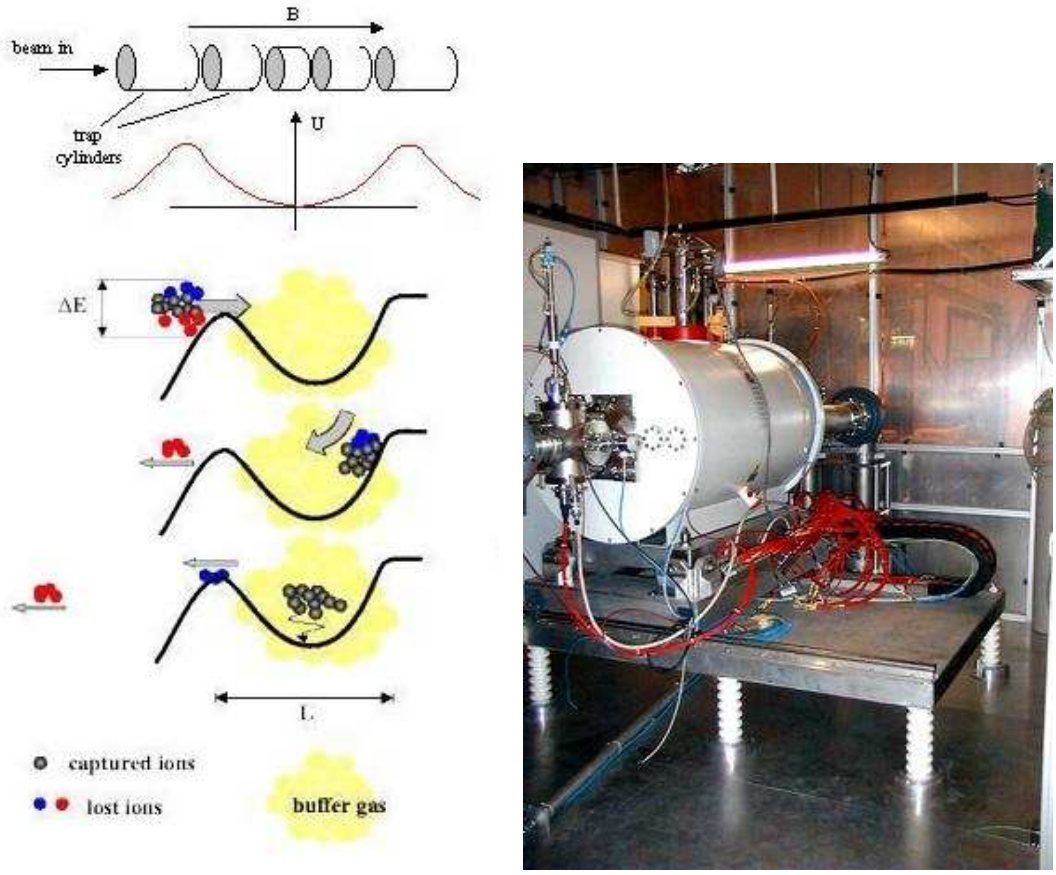

Figure 3.5: Schematic view of the trapping process and picture of the REXTRAP (taken from `http://isolde.web.cern.ch/isolde/`).

Experiment Parameters

Reaction	$q[e^+]$	A/q	$\tau_{Breed}[ms]$	$E_{Beam}[A \cdot MeV]$
^{108}Pd(^{122}Cd,^{122}Cd)^{108}Pd	31	3.935	153.8	2.85
^{104}Pd(^{124}Cd,^{124}Cd)^{104}Pd	30	4.133	154.0 - 158.6	2.85
^{96}Mo(^{138}Xe,^{138}Xe)^{96}Mo	34	4.059	204.1	2.86
^{96}Mo(^{140}Xe,^{140}Xe)^{96}Mo	34	4.118	204.1	2.86
^{96}Mo(^{142}Xe,^{142}Xe)^{96}Mo	34	4.176	204.1	2.86
^{96}Mo(^{144}Xe,^{144}Xe)^{96}Mo	34	4.235	204.1	2.7
^{64}Zn(^{124}Cd,^{124}Cd)^{64}Zn	30	4.133	255.1	2.84
^{64}Zn(^{126}Cd,^{126}Cd)^{64}Zn	31	4.065	255.1	2.84

Table 3.1: REX parameters for the experiments described in this work (see text for details).

3.3.3 REX Linac

As the intensity of radioactive ions out of the EBIS is much smaller than the intensity of residual gas ions, a mass separator prior to the linac is required. This mass separator is of the so-called Nier-spectrometer type (Nier and Roberts, 1951) and has reached q/A-resolutions of ~ 150. However, there will still be contaminants from residual gas isotopes with the same or similar A/q-values as the ion of interest in the beam. These can typically be ^{14,15}N,^{16,18}O,^{20,22}Ne,^{12,13}C and ^{36,40}Ar.

The linear accelerator consists of 4 different sections for stepwise accelerating the ions extracted from the EBIS (cf. figure 3.6). The 5 A·keV ions from the EBIS are accelerated to 300 A·keV by a **R**adio **F**requency **Q**uadrupole (*RFQ*). The RF quadrupole field provides transverse focussing while a modulation of the four rods bunches and accelerates the injected beam. The following IH (**I**nterdigital-**H**-type)-structure accelerates the ions from 0.3 A·MeV to an energy between 1.1 and 1.2 A·MeV. The output of the IH structure is matched to the first out of three 7-gap resonators with a triplet lens. Between the first and the second resonator there is an additional doublet lens for focussing. The three *7-gap resonators* can accelerate the ions up to 2.3 A·MeV. Until 2003 this has been the maximum beam energy at REX-ISOLDE.

These first three sections operate at 101.28 MHz, which is half the frequency of the CERN proton linac. In spring 2004 an energy upgrade up to 3 A·MeV has been achieved by installing an additional *9-gap resonator* which operates at 202.56 MHz. This upgrade has proven to be crucial for the ongoing Coulomb excitation experiments with exotic nuclei, since it increases the Coulomb excitation cross section significantly which compensates for the low beam intensities when going away from stability. The REX linac has a very compact design with a total length of only about 12m, since space was limited before the extension of the experimental hall in 2006.

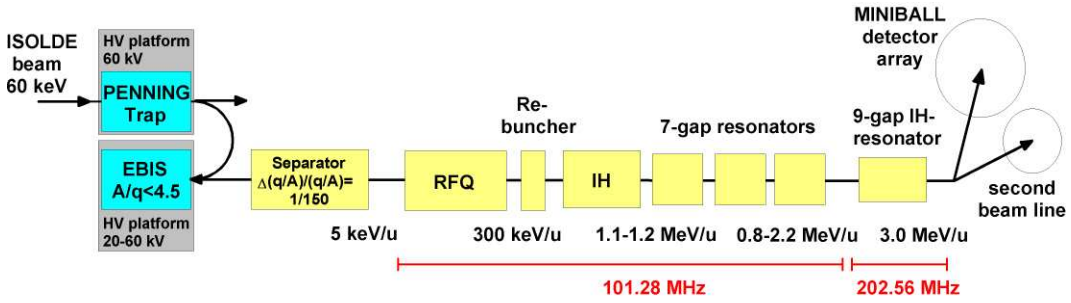

Figure 3.6: Schematic view of the different parts of REX and the linac (taken from `http://isolde.web.cern.ch/isolde/`).

3.4 The MINIBALL experiment

3.4.1 The Gamma Detector

The post-accelerated ion beam from REX is distributed to the experimental setup including the γ-ray detector array MINIBALL (see figure 3.7). MINIBALL consists of

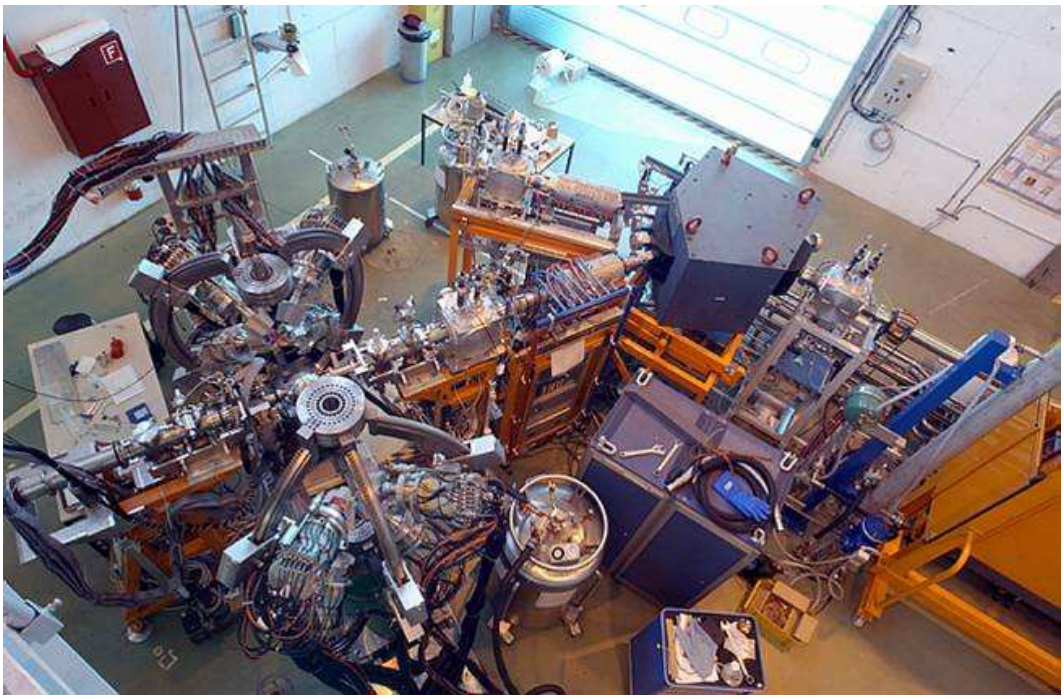

Figure 3.7: Bird view on the MINIBALL experimental site. On the right the end of the linac and the bending magnet can be seen. On the left the opened MINIBALL frame with the clusters can be seen (taken from Niedermaier (2005)).

24 individually encapsulated HPGe[3] detectors which are arranged in 8 triple clusters (cf. Eberth et al. (2001)). These clusters are mounted on six moveable arcs (the MINIBALL *frame*) so that their position in θ and ϕ can be optimized with respect to solid angle coverage or experimental specific constraints (see figure 3.8). The clusters can also be rotated around their axis by an angle α. In the setup used for this work the solid angle coverage was $\sim 60\%$ of the full 4π at a target-detector distance of about 10 cm (cf. figure 3.9).

Since the beam coming from REX will have velocities up to $\beta \sim 0.1$, the emitted γ-rays will be Doppler shifted. Therefore, a large granularity of the detector is required for a reasonable Doppler correction. To achieve this, each detector is electronically 6-fold segmented so that the overall granularity is $8 \times 3 \times 6 = 144$ (cf. figure 3.10). The electronic segmentation is achieved by shielding parts of the crystal sides during implantation of Boron n-type impurities. In this way, only parts of the crystal are connected and can be read out separately. The central electrode (the *core*), to which the depletion voltage is applied, will always detect an interacting γ-ray. It depends on the interaction point in the crystal which segment will detect it. It is assumed that the first interaction is also the main interaction, i.e. the interaction in which most of the energy is deposited. This plays a crucial role for the Doppler correction. In the so-called addback procedure the energies which are deposited in more than one crystal within a cluster by one γ-ray are added and linked to the position of the first

[3] **H**igh **P**urity **Ge**rmanium

Figure 3.8: The MINIBALL frame with its arms is shown (taken from `http://isolde.web.cern.ch/isolde/`).

Figure 3.9: Close-up of the MINIBALL clusters surrounding the target chamber. The different colours indicate the three crystals per cluster and the different shades of each colour indicate the segments (taken from `http://isolde.web.cern.ch/isolde/`).

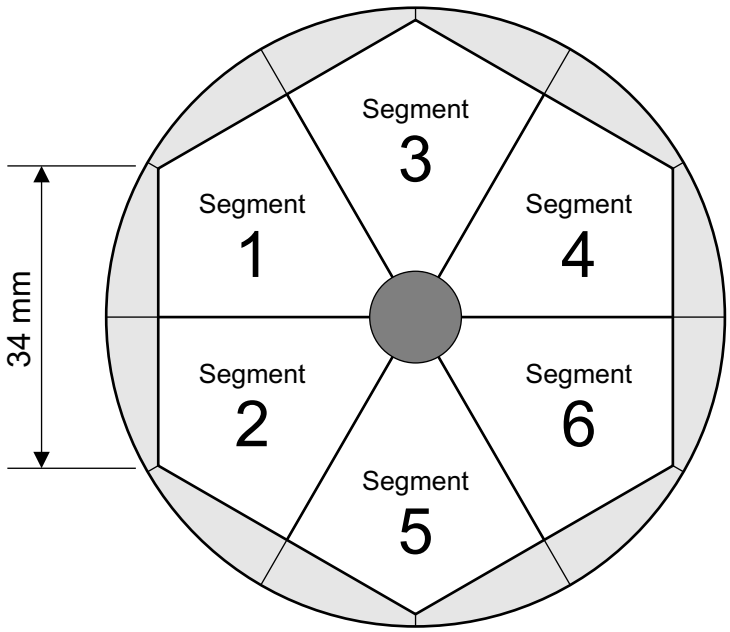

Figure 3.10: Schematic view of a cut through a MINIBALL crystal. The segments are indicated (by courtesy of Eppinger (2006)).

interaction. This increases the full energy peak efficiency, which is important when working with low-intensity RIBs. For more details on the MINIBALL spectrometer see also Weißhaar (2003).

Typical depletion voltages are around 2.5 - 4.5 kV. The crystals are kept at liquid nitrogen (LN2) temperature by attaching dewars to each of the 8 clusters which are connected with an autofill system.

3.4.2 The Particle Detector

For detecting the scattered beam particles as well as the target recoils, a **D**ouble **S**ided **S**ilicon **S**trip **D**etector (*DSSSD*) has been mounted in the target chamber. This so-called CD detector consists of four quadrants, each of which is read out independently. The front side is segmented in 16 annular strips for measuring ϑ whereas the back side consists of 24 sector strips which were linked into pairs for measuring φ. The annular strips have a width of 1.9 mm and a 2.0 mm pitch, the paired sector strips have a pitch of 6.8° (cf. figure 3.11). Each quadrant covers a range in φ of 81.6° and - at a target distance of 33 mm - the CD covers a range in ϑ_{lab} of $15° \lesssim \vartheta \lesssim 51°$.

During the $^{138-142}$Xe experiments the inner four rings of the CD were covered by a plug in order to prevent the CD from damage due to high count rates of elastically scattered particles occurring at small scattering angles and to reduce the dead time of the particle detector. In the ^{124,126}Cd and ^{144}Xe experiments the CD has been shielded by a degrader foil to reduce the energy of the detected particles.

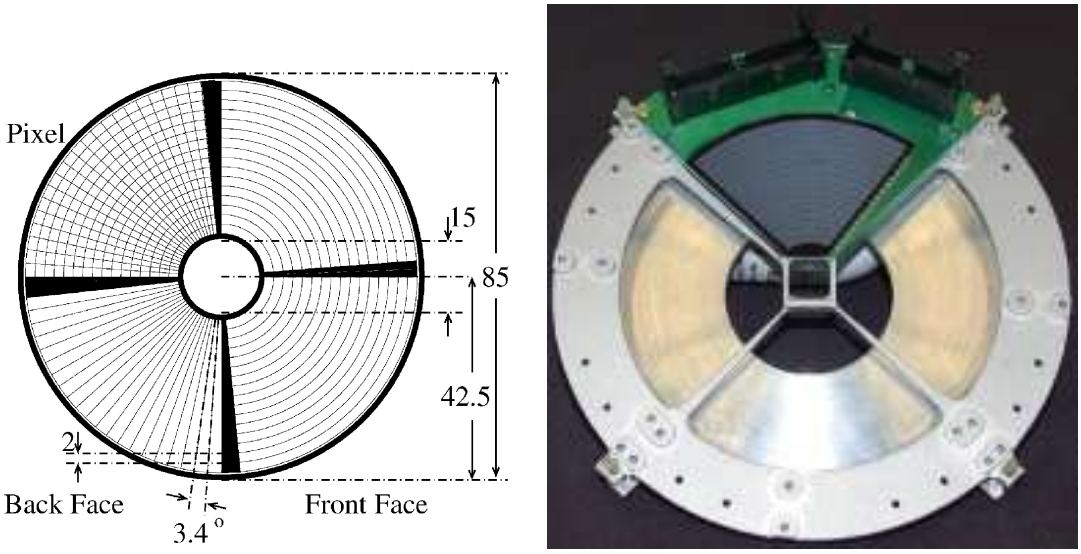

Figure 3.11: Schematic view of the CD detector and its segmentation (see text) and picture of one mounted quadrant (taken from Niedermaier (2005)).

3.4.3 Electronics and Data Acquisition

MINIBALL

The signals from the gamma detectors are integrated and amplified by the MINIBALL preamplifiers and then fed into the XIA DGF[4] modules (XIA, 2007) where they are digitized with a sampling frequency of 40 MHz. Since each DGF has four input channels two modules are needed per crystal (one channel for the core signal and six more channels for the segment signals, the remaining one stays empty). The digitized signal is further processed in an FPGA[5] where digital filter operations are used to gain energy and time information. The FPGA generates an event trigger if a useable event is present. The pulse is then fed into the DSP[6] and data read-out is forced. A detailed description can be found in Lauer (2004).

CD Detector

For each quadrant the signals from the 16 front and 12 back strips are fed into RAL 108 preamplifiers and from there into RAL 109 shapers where both a **C**onstant **F**raction **T**iming (CFT) and Gaussian-like shaping is performed. The logical OR of the timing signals as well as the energy signals from each strip are fed into a CAEN V785 ADC[7] module which generates the CD quadrant signal. The ORed timing signals are also fed into a time stamp DGF which runs with the same 40 MHz clock as the DGF modules used for MINIBALL. This is necessary for linking particle and gamma data, e.g. defining a time difference between the detection of particles and γ-rays (see also figure 4.10).

[4] **X**-ray **I**nstruments **A**ssociates, **D**igital **G**amma **F**inder
[5] **F**ield **P**rogrammable **G**ate **A**rray
[6] **D**igital **S**ignal **P**rocessor
[7] **A**nalog to **D**igital **C**onverter

Now for each particle event as well as for each gamma event an energy and a time stamp is stored. During the *event building* process the particles and the γ-rays with identical time stamps can be put together into one *event*.

Another important timing signal is the EBIS signal which marks the injection of ions from the EBIS into the linac. This signal starts a time gate (the so-called *On-beam* window) during which data is taken. The end of the On-beam window triggers the data read-out after which a second time gate with the same length (the so-called *Off-beam* window) is opened during which again data is taken. This data can be used to determine background radiation. Note that this data has to be read out before the next EBIS pulse.

Other timing signals that are available are the PS signal, indicating the start of a PS supercycle, the T1 signal indicating that the proton beam impinges on the ISOLDE target and the T2 signal indicating that the ions are allowed into the trap.

More important, for experiments which make use of the RILIS (as those performed with Cd beams for this thesis) a *Laser flag* signal indicating whether the laser was 'On' or 'Off' is also stored.

The data acquisition is performed with Marabou which writes the raw data to `.med` files (Lutter et al., 2009). This file format is based on the GSI MBS event structure. A code developed at the MPI in Heidelberg (cf. Niedermaier (2005)) is used to transform these into `.root` files containing a ROOT tree *rt* (see also Brun et al. (2009)).

3.5 Application to Experiment

The standard setup for all experiments described in this work consists of the MINIBALL gamma detectors, the particle detector, a PPAC[8] for beam monitoring and a beam dump gamma detector at the end of the beam line (cf. figure 3.12). The isotope under investigation is delivered as radioactive ion beam by REX whereas a suitable target is chosen individually for each experiment (cf. table 3.2).

Several aspects are taken into account for this choice: (i) the target nucleus should have a large enough and well-known Coulomb excitation cross section, (ii) the γ-energies of the transitions involved should differ significantly from those in the projectile nucleus, so that the resulting peaks in the γ-spectra are separable and (iii) the mass A of the target nucleus should be chosen such that the target recoils can be separated from the projectiles kinematically. Of course, it can be rather difficult to fulfill all of these aspects with an available target material.

For the determination of the $B(E2)$ values the γ-ray yields from the ejectile and target disexcitation peaks are needed. Since these γ-rays are emitted in-flight they have to be Doppler corrected. For the Doppler correction the energies and scattering angles of both the emitting particle and the γ-ray are needed and the following formula has to be applied:

$$E'_\gamma = \Gamma \times E_\gamma \times \{1 - \beta [\cos(\theta)\cos(\vartheta) + \sin(\theta)\sin(\vartheta)\cos(\delta\phi)]\} . \tag{3.1}$$

with $\delta\phi = \varphi - \phi$, $\Gamma = 1/\sqrt{1-\beta^2}$ and $\beta = \sqrt{2E/M}$ (E being the particle energy). The angles θ and ϕ belong to the γ-rays whereas ϑ and φ belong to the emitting particles.

[8] **P**arallel **P**late **A**valanche **C**ounter

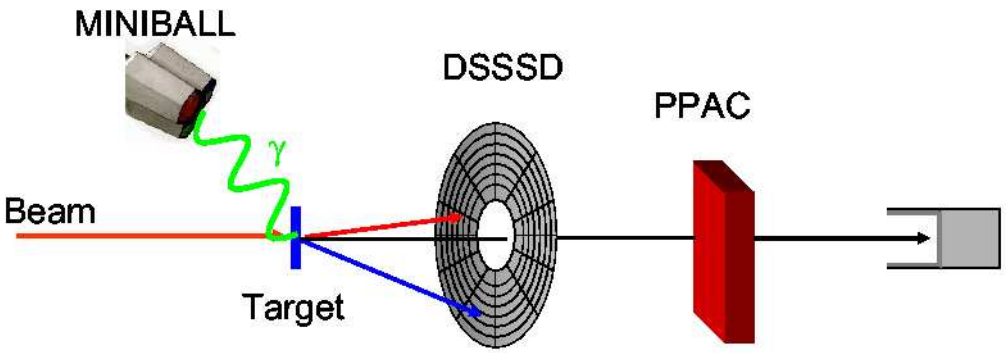

Figure 3.12: Schematic view of the experimental setup. The detection of projectiles and target recoils in the CD detector is indicated.

Targets of the Experiments

Beam	Target	Thickness $[mg/cm^2]$	ME($0 \rightarrow 2$) $[eb]$
^{122}Cd	^{108}Pd	2.0	0.872(13)
^{124}Cd	^{104}Pd	2.0	0.731(24)
^{124,126}Cd	^{64}Zn	1.8	0.400(19)
$^{138-144}$Xe	^{96}Mo	1.7	0.520(4)

Table 3.2: The targets chosen for the experiments described in this work along with their thicknesses and transitional matrix elements.

3.5.1 Position Calibration of the Gamma Detector

The angles (θ, ϕ, α) of the MINIBALL clusters - and therefore the positions of the crystals - are determined using the 1-neutron pick-up reaction d(^{22}Ne,^{23}Ne)p. In this reaction the first excited state in ^{23}Ne $\left(J^\pi = \frac{1}{2}^+\right)$ at 1017 keV is populated. It disexcites in-flight while the ejectile essentially moves in beam direction. Thus, the observed Doppler shift of the γ-ray can be used for the position calibration of the Ge detectors. The angular coordinates are varied recursively until (i) the FWHM[9] of the Doppler corrected peak in one cluster is minimized and (ii) the Doppler corrected peaks in the 6 segments are aligned (see also van de Walle (2006)).

3.5.2 Position Calibration of the Particle Detector

In the Coulomb excitation experiments the angles of the particles can be determined from the position sensitive CD detector. Of course, an uncertainty in this determination remains. The uncertainty $\Delta\vartheta$ in the scattering angle is of great importance for the further analysis, since it is not only needed in the Doppler correction, but also for the

[9] **F**ull **W**idth **H**alf **M**aximum

angular range over which the CLX calculations have to be integrated and for estimating the CD efficiency.

The position of the detected particle on the CD can be described by polar coordinates (r,φ) where the radius r is determined from the annular strip (*ring*) on the front side and the angle φ from the radial strip on the back side. It is then

$$\vartheta = \arctan\left(\frac{r}{d}\right) \tag{3.2}$$

$$\Delta\vartheta = \frac{\sqrt{\left(\frac{\Delta r}{r}\right)^2 + \left(\frac{\Delta d}{d}\right)^2}}{1 + \left(\frac{r}{d}\right)^2} \times \frac{r}{d} \tag{3.3}$$

with $\Delta r = \sqrt{\Delta r_{ring}^2 + \Delta r_{spot}^2}$ and d being the distance between the target and the CD detector. The beam spot size is estimated to be $\Delta r_{spot} = 1\ mm$, the uncertainty due to the ring width is $\Delta r_{ring} = 1\ mm$ and the uncertainty in the distance is $\Delta d = 1\ mm$. The calculated uncertainty $\Delta\vartheta$ for each ring and an applied polynomial fit are shown in figure 3.13. The angular range of the CD detector in this setup is then $\vartheta_{lab} = 15(2)^\circ - 51(1)^\circ$.

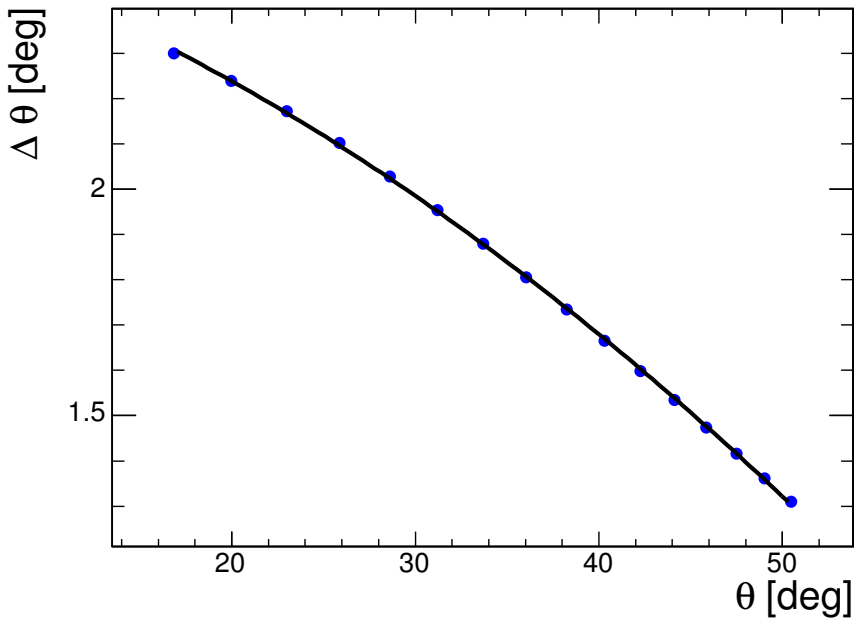

Figure 3.13: The uncertainty of the scattering angle is calculated for each ring. A polynomial fit of order 2 has been applied.

3.5.3 Energy Calibration of Particle Detector

The other variable determined from the CD and needed for the Doppler correction is the particle energy. The CD detector was therefore calibrated using a triple α-source,

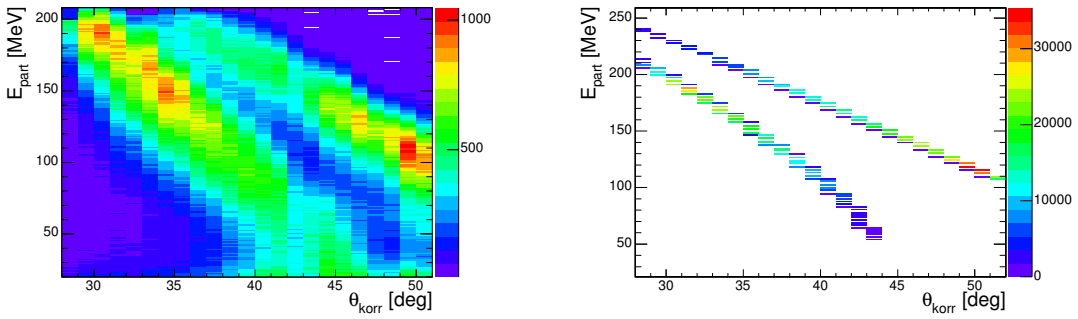

Figure 3.14: Particle energies for ^{140}Xe and ^{96}Mo as detected in the CD (left) and based on kinematic calculations (right) vs. the corrected scattering angle in degrees. The correction has been applied due to a shift of the beam spot with respect to the center of the CD (see chapter 4).

consisting of ^{239}Pu, ^{241}Am and ^{244}Cm with α-energies of 5.156 MeV, 5.486 MeV and 5.805 MeV, respectively. Of course, the extrapolation of these energies to energies of the order of $\sim 10^2$MeV (as occur in the experiments described in this work) is problematic. This is one of the reasons why in the later analysis the scattering angle ϑ has been used to assign the particle energy via a look-up table based on kinematic calculations including the energy loss in the target. Another reason is that the range of the preamplifiers of the CD detector is limited to about 200 MeV and that the degrader foil used in later campaigns further distorts the energy signal. For the detection of intermediate-mass and heavy ions, one has also to take care of the so-called *pulse height defect* (see Knoll (1979)). This states that the charge produced by a heavy ion in silicon is significantly less than the charge produced by a light ion depositing the same energy and that this effect increases with the atomic number of the ion. A comparison between the detected and the tabulated energy can be seen in figure 3.14.

3.5.4 Energy Calibration and Relative Efficiency of the Gamma Detectors

For the energy calibration of the MINIBALL array source measurements with ^{60}Co and ^{152}Eu were used. The sources were placed at target position. First, the two prominent lines of ^{60}Co at 1173 keV and 1332 keV were used for a rough calibration of the MINIBALL channels. Subsequently, the most prominent γ-lines in the ^{152}Eu spectrum (ranging from 122 keV to 1408 keV) have been used for a fine tuning of this calibration.

The ^{152}Eu source measurement has also been used to determine the relative photopeak efficiencies ϵ_γ of the MINIBALL spectrometer. The efficiency is defined as $\epsilon_\gamma = N_\gamma / I_\gamma$ with N_γ being the yield in one line of the spectrum and I_γ their relative intensity. Plotting these efficiencies for the most prominent lines versus the corresponding line energies shows the dependence of ϵ_γ from E_γ. For the determination of σ_{ce} the efficiencies at the energies of the transitions under investigation are needed (see eq. 2.21). These

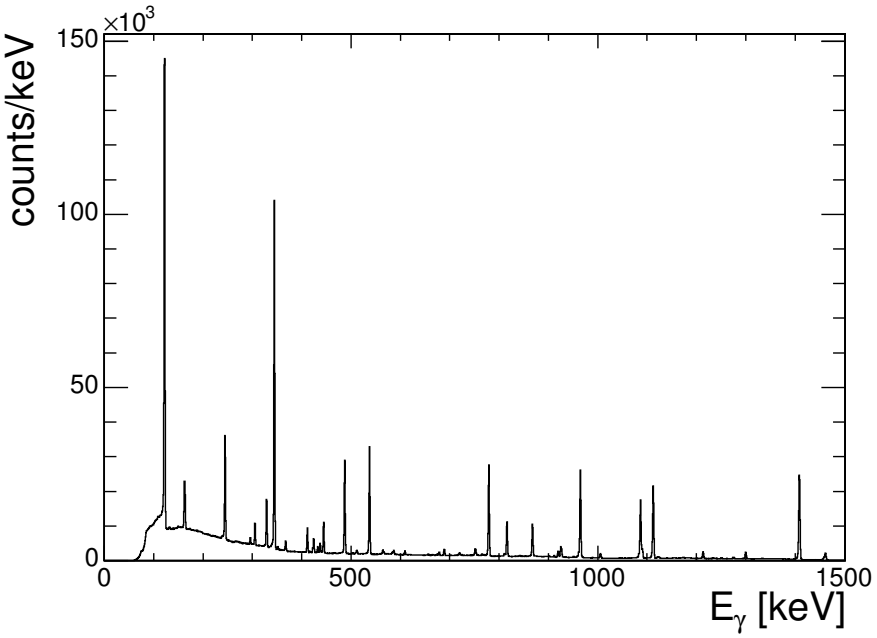

Figure 3.15: The γ-ray spectrum from the ^{152}Eu source in the energy range of the most prominent lines.

are determined by fitting a power law function[10] (cf. Knoll (1979)) to the measured efficiencies and evaluating this function at the corresponding energies. The efficiencies ϵ_γ for the different beam times investigated in this work are summarized in table 3.3. Note that the relative uncertainty is of the order of $\frac{\Delta\epsilon_\gamma}{\epsilon_\gamma} \sim 10^{-3}$ and will therefore be neglected in the further analysis.

[10] This function looks like $f(x) = \exp\left[\sum_{i=0}^{3} p_i x^i\right]$ with $x = \log_{10}(E_\gamma)$. The γ-energy is given in MeV.

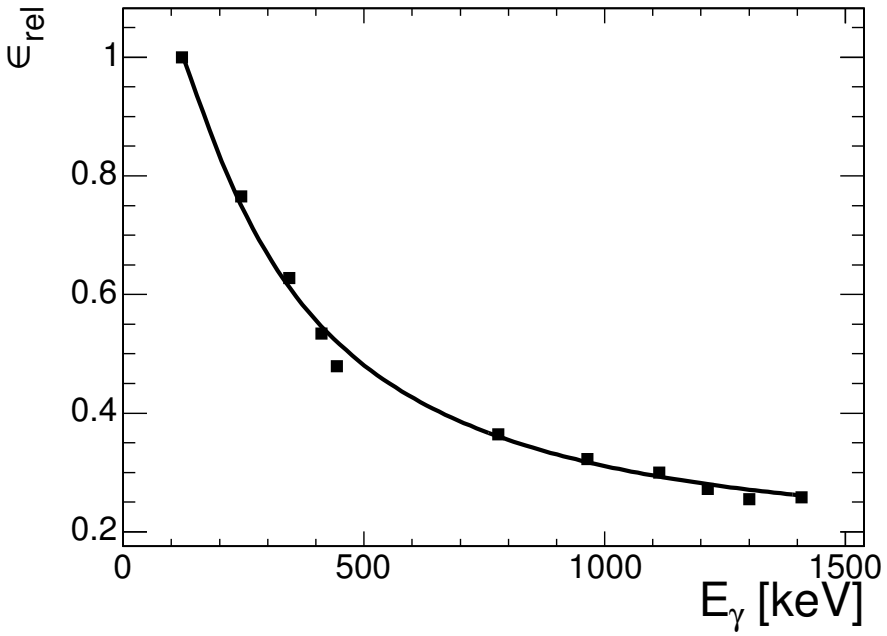

Figure 3.16: The relative efficiency of MINIBALL. Note that ϵ_γ is normalized to the 122 keV line.

Photopeak Efficiencies for the different Transitions

Isotope	Transition	Energy $[keV]$	ϵ_γ
^{122}Cd	$2_1^+ \rightarrow 0_1^+$	569.5	0.455
^{124}Cd	$2_1^+ \rightarrow 0_1^+$	613.2	0.434
^{108}Pd	$2_1^+ \rightarrow 0_1^+$	433.9	0.545
^{104}Pd	$2_1^+ \rightarrow 0_1^+$	555.8	0.464
^{138}Xe	$2_1^+ \rightarrow 0_1^+$	588.8	0.432
^{140}Xe	$2_1^+ \rightarrow 0_1^+$	376.7	0.580
	$4_1^+ \rightarrow 2_1^+$	457.6	0.518
^{142}Xe	$2_1^+ \rightarrow 0_1^+$	287.2	0.687
	$4_1^+ \rightarrow 2_1^+$	403.5	0.559
^{96}Mo	$2_1^+ \rightarrow 0_1^+$	778.2	0.361
^{124}Cd	$2_1^+ \rightarrow 0_1^+$	613.2	0.426
^{126}Cd	$2_1^+ \rightarrow 0_1^+$	652	0.409
^{64}Zn	$2_1^+ \rightarrow 0_1^+$	991.6	0.314
^{144}Xe	$2_1^+ \rightarrow 0_1^+$	252.6	0.753
^{96}Mo	$2_1^+ \rightarrow 0_1^+$	778.2	0.365

Table 3.3: The relative gamma efficiencies of MINIBALL at the energies of the transitions analyzed in this work.

—Imagination is more important than knowledge. For knowledge is limited.

Albert Einstein (1879-1955)

4 Data Analysis

4.1 Analysis of the ^{122,124}Cd Data

In this beam time the Coulomb excitation cross sections for the first excited states in ^{122,124}Cd have been determined via the reactions ^{108}Pd(^{122}Cd,^{122}Cd*)^{108}Pd* and ^{104}Pd(^{124}Cd,^{124}Cd*)^{104}Pd*, respectively.

4.1.1 Particle Spectra

The raw energy spectra per ring and strip for each sector are used to examine the condition of the CD detector. During this campaign the CD detector was fully functional. In figure 4.1 the detected particle energy is plotted versus the laboratory scattering angle. Unfortunately the ejectile and the target recoil cannot be separated kinematically.

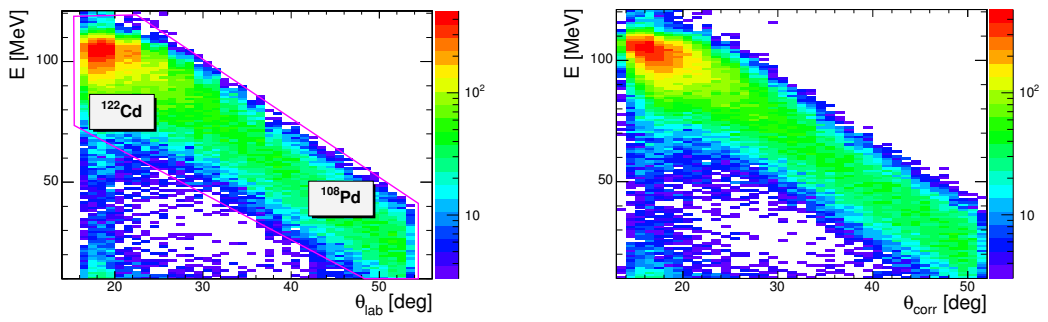

Figure 4.1: The measured particle energy versus scattering angle for ^{122}Cd is shown before (left) and after (right) the beam shift correction. The cut on the elastically scattered projectiles and recoils is also shown (magenta line).

Therefore, a graphical cut on both is used for the further analysis. According to the

number of particles detected in this cut different types of events can be distinguished (see table 4.1). The number of events according to its event type for the ^{122}Cd beam

Definition of Event Types	
Event Type	Particle Multiplicity
0	0
1	1
2	2
3	> 2

Table 4.1: Definition of the *event types* (ET) according to the number of particles detected in the graphical cut.

time is plotted in figure 4.2. Note that about 86% of all events are of type 1 whereas only about 0.1% are of type 3, which are considered unphysical. Only events of type 1 or 2 are used in the analysis. For events of type 2 a consistency check is done by evaluating the difference of the azimuthal angle of both particles. For the ejectile and the recoil this should be $\Delta\varphi = 180°$ which is indeed the experimental result (cf. figure 4.2).

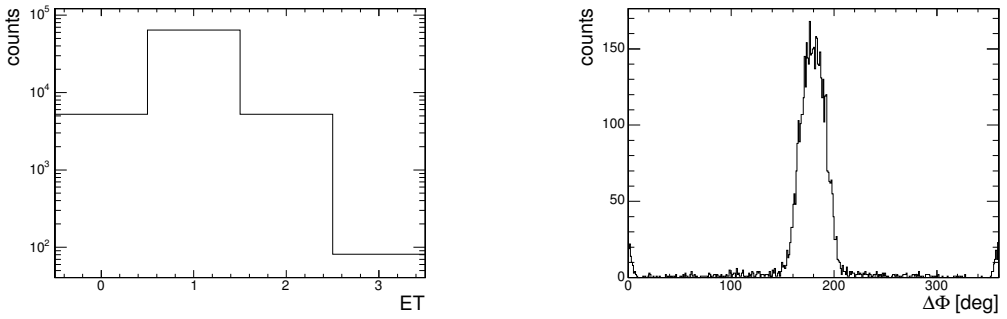

Figure 4.2: The number of different event types (left) and the difference in φ of two detected particles (right) for the ^{122}Cd run are shown. $\Delta\varphi$ centers at $(180 \pm 11)°$ as expected.

Beam Shift Correction

The next step of the data analysis is the determination of the shift of the beam spot with respect to the center of the CD detector. If the beam was centered, the intensity of elastically scattered particles in one ring, i.e. in a constant interval $[\vartheta,\vartheta + d\vartheta]$, would be constant. Since this is obviously not the case (cf. figure 4.3) the beam spot position is shifted in radial steps of 1 *mm* and angular steps of 3.75° (which is half the ring width and half the strip width) until the deviation of $I(\varphi)$ from the mean value is minimized. The mean value $< I(\varphi) >$ is defined as

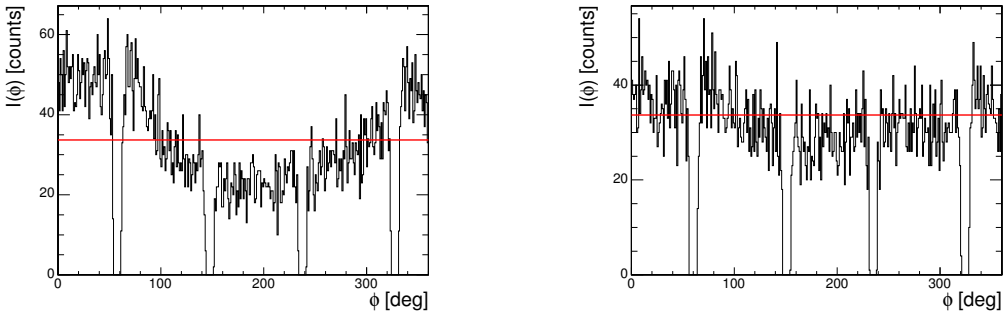

Figure 4.3: The intensity of elastically scattered particles in the range $21° \leq \vartheta \leq 25°$ before (left) and after (right) correction due to the beam shift for ^{122}Cd. The mean intensity is also shown (red line).

$$< I(\varphi) >= \frac{1}{n} \sum_{j=1}^{n} I_j(\varphi) \tag{4.1}$$

with n being the number of bins with non-zero content in the shown histogram. The deviation is then defined as

$$\Delta < I(\varphi) >= \frac{1}{n-1} \sum_{j=1}^{n} (I_j(\varphi) - < I(\varphi) >)^2 \,. \tag{4.2}$$

The resulting beam shifts are summarized in table 4.2. Of course, these shifts are not necessarily constant over time and they cannot be measured more accurate than the segmentation of the CD detector allows. The corrected angles ϑ_{corr} are then used to

Beam Shift Parameters

Beam	$r[mm]$	$\varphi[°]$
^{122}Cd	1	18.75
^{124}Cd	1	30.0

Table 4.2: The offset of the beam spot with respect to the CD center in polar coordinates for the ^{122,124}Cd beams.

assign the particle energy (see section 3.5). The range of the scattering angle covered by the CD detector and the applied cut is $15.0(23)° \leq \vartheta_{corr} \leq 50.0(13)°$ in the laboratory system.

Beam Purity

Since there is a significant amount of isobaric contaminants in the ^{122,124}Cd beams the beam purity and beam composition have to be taken into account for the further analysis. In this beam time the RILIS (cf. section 3.2.2) has been used which allows a comparison between 'Laser On' and 'Laser Off' data. In the latter, only the contaminants reach the target chamber while in the former both the isotope of interest and the

contaminant can react with the target. Hence, two methods are applied to estimate the overall beam purity: (i) a comparison of the number of elastically scattered particles in the cut (i.e. beam-like particles) during 'Laser On' and 'Laser Off' runs and (ii) a comparison of the gamma yields from the target disexcitation during 'Laser On' and 'Laser Off' runs (cf. figure 4.4). For both it can be said that

$$N_{ON} = N_X + N_{Cd} \quad \text{and} \quad N_{OFF} = N_X$$

with X being the sum of all contaminants. The beam purity R is then given by

$$R = 1 - \frac{N_{OFF}}{N_{ON}}. \tag{4.3}$$

For the ^{122}Cd beam the numbers are given in table 4.3.

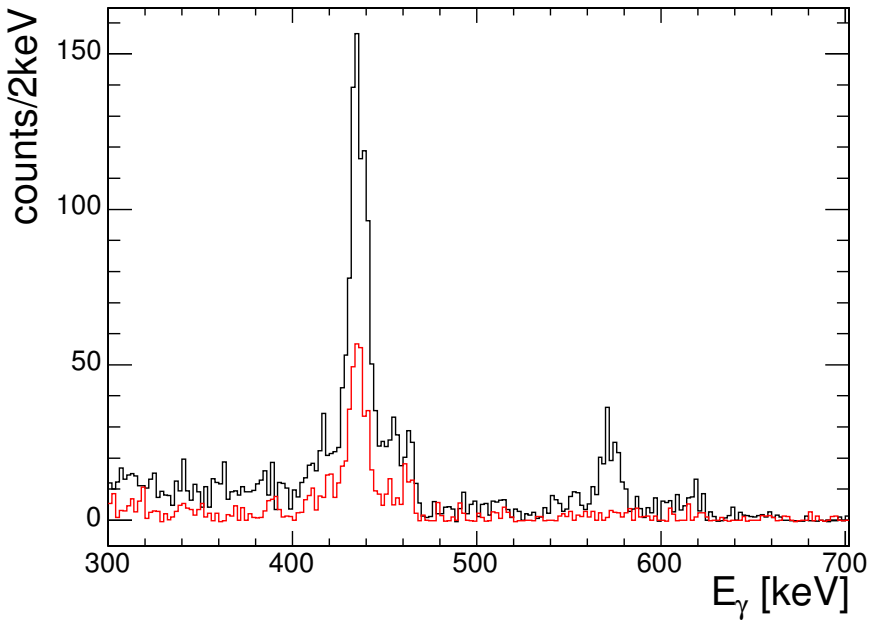

Figure 4.4: The peak from the $2_1^+ \rightarrow 0_1^+$ disexcitation of the ^{108}Pd target in 'Laser On' (black) and 'Laser Off' (red) mode can be seen at $E_\gamma \approx 435\ keV$. Note that the disexcitation peak of ^{122}Cd ($E_\gamma \approx 570\ keV$) vanishes in 'Laser Off' mode as expected. The FWHM of the peaks is 9 keV and 11 keV for Pd and Cd, respectively.

For the ^{124}Cd beam the amount of contamination is more ambiguous. Looking closer at the single runs taken in the 'Laser On/Off' mode (i.e. where a shutter switches the laser periodically on and off) it can be seen that the beam purity varies between about 7% and 70% and that there have been problems with the shutter not working properly. Therefore, the beam purity has been determined for each run by comparing the elastically scattered beam-like particles and a mean beam purity of $R = 22(5)\%$ has been established. The statistics in the target deexcitation peak is too low for analyzing in the single runs.

Beam Purity

Method	N_{ON}	N_{OFF}	R[%]
(i)	14153	5602	60.4(6)
(ii)	1255	489	60(2)

Table 4.3: Determination of the beam purity R for ^{122}Cd by comparing (i) the elastically scattered beam-like particles and (ii) the target excitation yields during 'Laser On' and 'Laser Off' runs.

Furthermore, the composition of the beam can be estimated from the γ-ray spectrum of the beam dump detector (cf. figure 4.5). There, the decay lines from the isotope of interest as well as from the contaminants can be observed. Dividing the yields of the identified lines by their relative intensities and plotting these values versus the line energies results in a plot that can be used to estimate the amounts of the identified isotopes in the beam. In the case of ^{122}Cd the following decay chains have to be taken into account:

- $^{122}\mathrm{Cd} \xrightarrow{5.14s} {}^{122}\mathrm{In}(1^+) \xrightarrow{1.5s} {}^{122}\mathrm{Sn}$
- $^{122}\mathrm{In}(5^+) \xrightarrow{10.3s} {}^{122}\mathrm{Sn}$
- $^{122}\mathrm{In}(8^-) \xrightarrow{10.8s} {}^{122}\mathrm{Sn}$
- $^{122}\mathrm{Cs}(1^+) \xrightarrow{21.2s} {}^{122}\mathrm{Xe} \xrightarrow{20.1h} {}^{122}\mathrm{I}$
- $^{122}\mathrm{Cs}(8^-) \xrightarrow{3.70m} {}^{122}\mathrm{Xe} \xrightarrow{20.1h} {}^{122}\mathrm{I}$

The values in brackets indicate the spin and parity J^π of the decaying state, the values above the arrows its half-life $T_{1/2}$.

Defining

$$\epsilon_x(E_\gamma) := \frac{N_\gamma(E_\gamma)_x}{I_\gamma(E_\gamma)_x}$$

as the gamma yield of a decay line at an energy E_γ belonging to the isotope x divided by its relative gamma intensity it can be assumed that

$$\frac{n_x}{n_y} \propto \frac{\epsilon_x(E_\gamma)}{\epsilon_y(E_\gamma)}.$$

Here, $n_{x(y)}$ denotes the relative amount of the isotope $x(y)$ in the beam and the values $\epsilon_{x(y)}$ are evaluated at the same energy E_γ. In figure 4.6 the values ϵ are plotted versus the γ-energy for several lines from different isotopes. One of the isotopes with a sufficient number of identified lines can be taken as reference isotope (e.g. $^{122}\mathrm{In}(5^+)$ in the $A = 122$ beam). A power law function (as in section 3.5) is fitted to its graph and evaluated at the energies of the decay lines from the other isotopes. Note that only the energy range between 800 keV and 2200 keV has been taken into account due to the

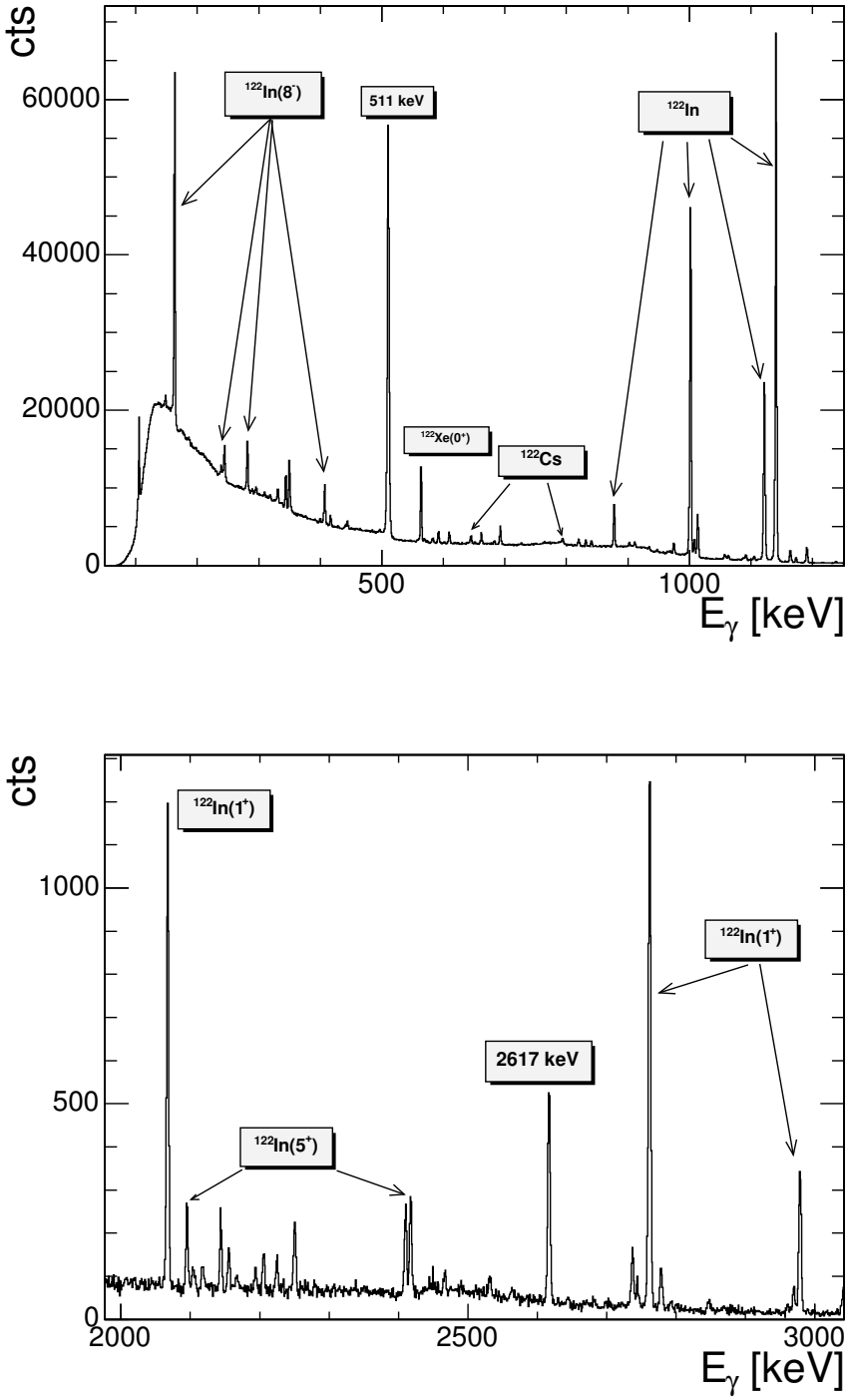

Figure 4.5: The γ-energy spectrum from the beam dump detector for the ^{122}Cd run in two energy ranges. Some of the identified decay lines are labelled corresponding to their parent nuclei. Note that the lines at 878 keV, 1002 keV, 1122 keV and 1140 keV can stem from all three J^π states of ^{122}In under consideration here. The line at 2617 keV results from the natural background decay ^{208}Bi $\rightarrow$ ^{208}Pb. The observed ^{122}Xe is the decay product of ^{122}Cs. There might also be a contribution of ^{122}Xe decay in the line at 282 keV.

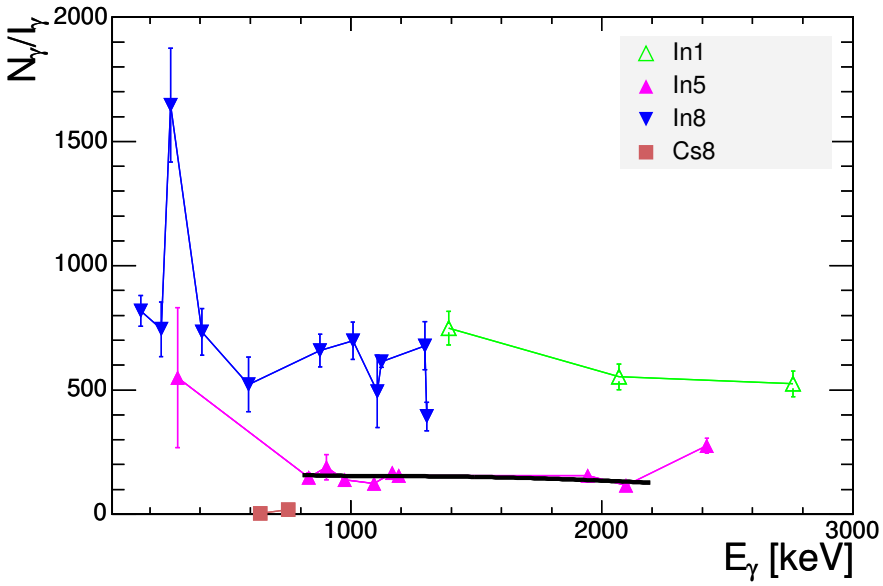

Figure 4.6: The ratios of the yields to the line intensities for the identified contaminants. The numbers in the legend correspond to the spins of the decaying states. The fit function is also shown (see text for details). The peculiar behaviour of ^{122}In(8^-) at 282 keV can be explained by an additional contribution from the decay of ^{122}Xe at this energy.

reliability of the determined intensities. These fit values $\epsilon_{fit}(E_\gamma)$ are then compared to the experimental determined values $\epsilon_x(E_\gamma)$ by defining

$$r_x(E_\gamma) := \frac{\epsilon_x(E_\gamma)}{\epsilon_{fit}(E_\gamma)}.$$

These ratios r_x are averaged over all suitable decay lines from the isotope x, resulting in mean ratios $< r_x >$. Let x,y and z be the only isotopes present and z be the reference isotope. It can then be shown that

$$\frac{n_x}{n_z} \propto \frac{\epsilon_x(E_0)}{\epsilon_z(E_0)} = \frac{\epsilon_x(E_0)}{\epsilon_{fit}(E_0)} =< r_x > \tag{4.4}$$

$$n_x =< r_x > \cdot n_z \tag{4.5}$$

$$n_x + n_y + n_z = 1 \tag{4.6}$$

$$\Rightarrow n_z = [1+ < r_x > + < r_y >]^{-1}. \tag{4.7}$$

With this procedure the relative amount of the isotopes in the beam can be estimated. Note that the beam isotope also decays so that some of the decay lines in the γ-energy spectrum of the beam dump detector do not stem from contaminants but rather from the isotope of interest.

For the ^{122}Cd beam the estimated beam composition is approx. 60% of ^{122}Cd, 25% of ^{122}In and 15% of ^{122}Cs. This is in agreement with the overall beam purity determined from the 'Laser On' and 'Laser Off' data. Note that these amounts are

only accurate to about a factor of ~ 1.5 due to uncertainties in the fit function as well as in the averaged ratios. For the ^{124}Cd beam this procedure did not result in a consistent beam composition due to difficulties in assigning the decay lines to a certain isotope. Hence, in the analysis of the data from the ^{124}Cd runs only the beam purity but not its composition has been taken into account.

Efficiency of the CD detector

For the determination of the relative efficiency of the CD detector and the applied cut an effective Rutherford cross section for this beam composition is used. In figure 4.7 a comparison of this effective $\sigma_{Ruth,eff}$ with that of a pure ^{122}Cd beam is shown. Since the beam components have similar charge numbers Z the difference in cross sections is at most approx. 5%.

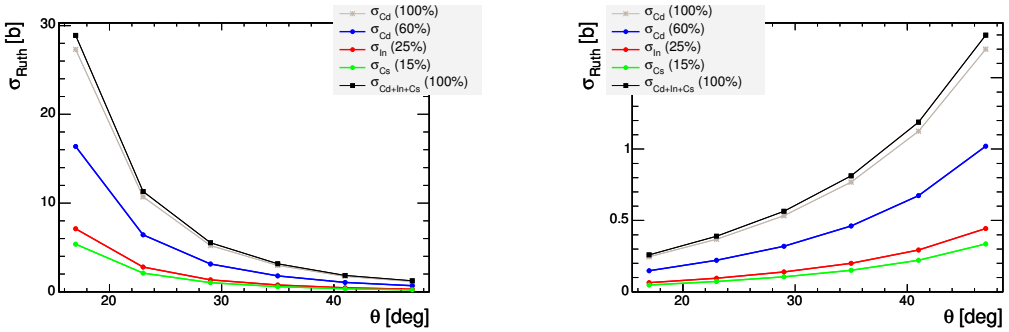

Figure 4.7: The effective Rutherford cross section per ϑ interval for the projectiles (left) and the recoils (right) in the ^{122}Cd experiment. A pure cross section is plotted for comparison as well as the relative contributions. Note that the cross section is much larger for Cd than for Pd for $\vartheta \lesssim 40°$.

The efficiency of the CD detector and the applied cut is determined by comparing the number of elastically scattered particles in small intervals of ϑ (cf. figure 4.9) to the effective Rutherford cross section. Since both the projectiles and the recoils are detected in the cut, the comparison has to be done with the sum of the corresponding cross sections (cf. figure 4.8):

$$\sigma^{tot}_{Ruth,eff} = \sigma^{Cd}_{Ruth,eff} + \sigma^{Pd}_{Ruth,eff}.$$

The relative efficiency is then given by

$$\epsilon_{rel}(\vartheta) = N_{el.}(\vartheta)/\sigma^{tot}_{Ruth,eff}(\vartheta).$$

This efficiency - normalized to one - is shown in figure 4.9 for the ^{122}Cd experiment. Note that it drops towards smaller scattering angles. The innermost intervals are affected by the beam shift and the finite beam spot leading to a fewer amount of detected particles than expected. Also, the uncertainty in ϑ increases with decreasing scattering angle whereas the Rutherford cross section becomes more sensitive (see figure 4.8).

The γ-ray spectra will then be weighted with these efficiencies according to the scattering angle of the detected particle. Since the relative uncertainties are of the order of $\frac{\Delta\epsilon}{\epsilon} \sim 10^{-1}$, they have to be taken into account in the further analysis.

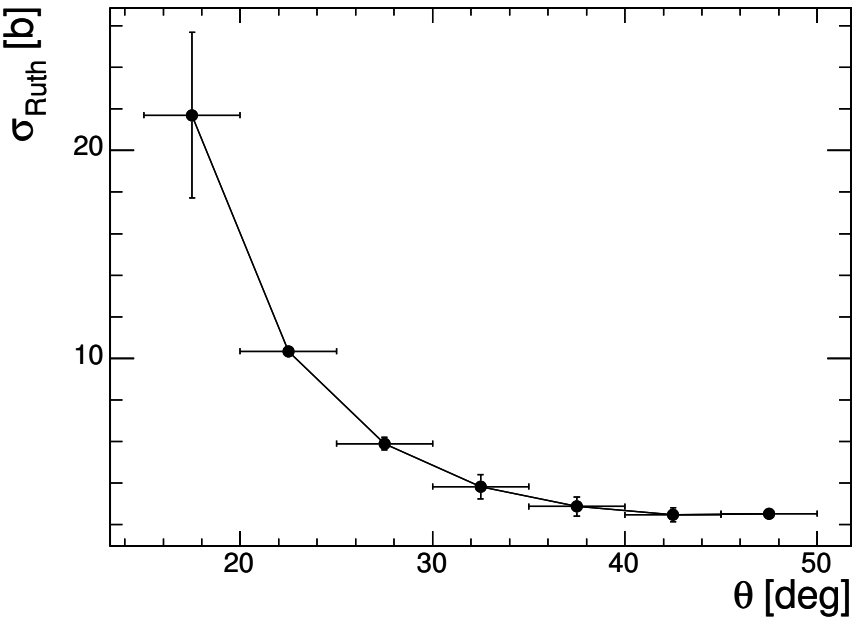

Figure 4.8: The sum of the two effective Rutherford cross sections from figure 4.7. The uncertainties $\Delta\epsilon$ include the statistical error as well as the uncertainty in the scattering angle ϑ.

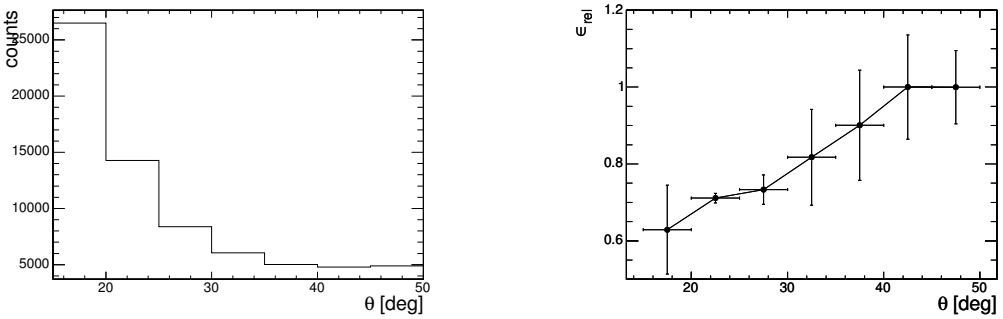

Figure 4.9: The number of elastically scattered particles in intervals of 5° ranging from $15° \leq \vartheta \leq 50°$ (left) and the relative efficiency of the CD detector and the applied cut in the ^{122}Cd run (right) is shown.

4.1.2 Gamma Ray Spectra

For the Doppler corrected γ-ray spectra the γ-rays emitted by the projectiles or recoils have to be identified and background radiation has to be suppressed. The γ-rays are detected with the MINIBALL spectrometer and the emitting particles are detected with the CD detector. Plotting the time difference between the detection of particles and γ-rays, a clear correlation between γ-rays emitted by the reaction partners (*prompt peak*)

and those from random background can be seen (cf. figure 4.10). The γ-ray spectra

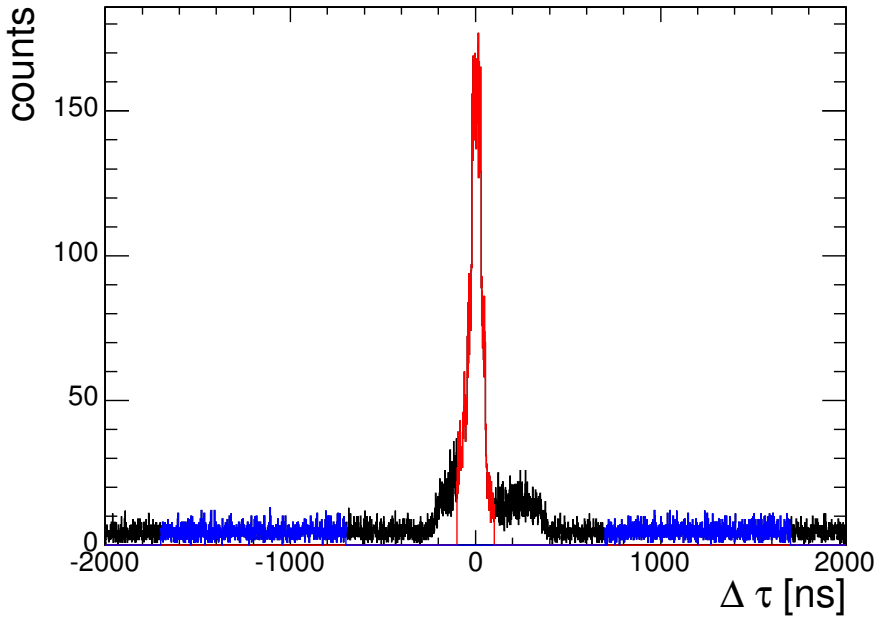

Figure 4.10: Time difference between detected particles and γ-rays in the ^{122}Cd experiment. The prompt peak (red) corresponds to γ-rays emitted by the reaction partners whereas the random time gate (blue) is used for background subtraction.

taken during the random time gate are then subtracted from those taken during the prompt time peak. Note that the random time gate is much longer than the prompt peak. The corresponding spectra will therefore be weighted with t_{prompt}/t_{random} before subtraction.

Since it is not possible to distinguish between projectiles and target recoils in the CD detector one has to check different assumptions. For events of type 1 it can be assumed either that the detected particle was Cd or Pd. The Doppler corrected γ-ray spectra for both assumptions are shown in figure 4.11. Note that the difference between them is small because both particles have similar velocities at the same scattering angle. The Doppler correction will therefore shift the γ-energies to a sharp line if the γ-ray was emitted by the detected particle.

It is also possible to reconstruct the angles and energy of the other particle, which was not detected, and to Doppler correct the γ-rays with respect to this particle. For events of type 2 it can be shown that it also makes hardly any difference which of the two particles is assumed to be Cd and Pd for the Doppler correction (see figure 4.11).

An alternative way is to plot the Doppler corrected γ-energies in a two-dimensional spectrum. For events of type 1 it is assumed that the detected particle was always Cd, due to the overall larger Rutherford cross section. For the same reason the particle with the lower scattering angle in events of type 2 is assumed to be Cd. The γ-energy corrected with respect to the assumed Cd is then plotted along the x-axis whereas

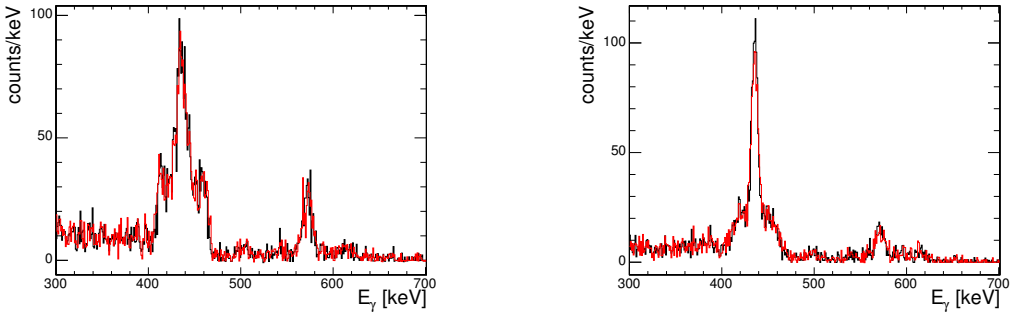

Figure 4.11: Left: Doppler corrected γ-ray spectrum for Event Type 1 assuming the detected particle was ^{122}Cd (black) or ^{108}Pd (red). Right: The same spectrum for events of type 2 assuming the first particle to be ^{122}Cd (black) or ^{108}Pd (red).

the γ-energy corrected with respect to the assumed Pd is plotted along the y-axis. In figures 4.12 and 4.13 it is shown that along both axes there are two peaks at the energies of the $2_1^+ \rightarrow 0_1^+$ transitions of ^{122,124}Cd and ^{108,104}Pd, respectively. The corresponding projections on the x- and y-axis are also shown. The advantage of this method can clearly be seen for the ^{124}Cd run (figure 4.13) where the peaks in the projection along one axis have a significant overlap due to the transition energy of both ejectile and target nuclei being very close. This makes it more difficult to integrate the gamma yield correctly. In the two-dimensional spectrum both peaks can be separated more clearly by applying cuts on these peaks separately for x and y as well as in total. It is

$$N_{hit} + N_{rec} = N_{tot} + N_{bg} \tag{4.8}$$

and therefore

$$N'_{hit} = N_{hit} - N_{bg} = N_{tot} - N_{rec} \tag{4.9}$$

$$\text{and} \quad N'_{rec} = N_{tot} - N_{hit} \tag{4.10}$$

with N_{hit} (N_{rec}) being the yield in the peaks along the x-axis (y-axis), N_{tot} being the yield in the total cut and N_{bg} being the wrongly corrected background. This formula is now applied to both peaks which results in three separate ways of determining the Coulomb excitation cross section. One can apply either

$$\text{(i)} \quad \frac{N'_{hit}(Cd)}{N'_{rec}(Pd)} \quad , \text{(ii)} \quad \frac{N'_{rec}(Cd)}{N'_{hit}(Pd)} \quad \text{or (iii)} \quad \frac{N_{tot}(Cd)}{N_{tot}(Pd)}$$

in eq. 2.21. Note that for the calculation of $\sigma_{ce}^{(Pd)}$ the angular range has to be adjusted to each of these ratios. The yield from the target excitation $N(Pd)$ has also to be multiplied with the beam purity R before the comparison. The results for the ^{122,124}Cd runs are summarized in table 4.4. The resulting matrix elements are in agreement within the uncertainties. A more thorough discussion of these results can be found in chapter 5.

The uncertainties of the Coulomb excitation cross sections of the Cd isotopes are, according to eq. 2.21, influenced by the statistical uncertainties of the gamma yields

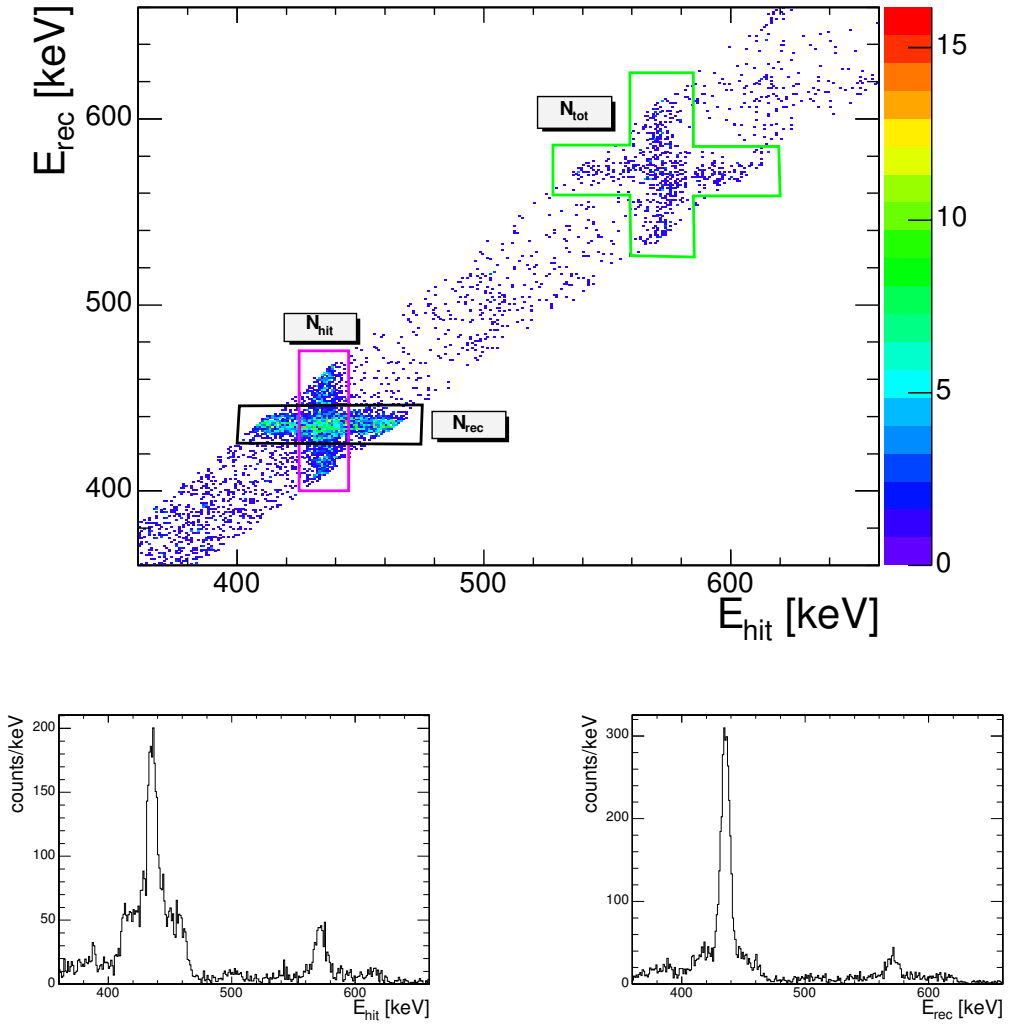

Figure 4.12: Top: the Doppler corrected γ-energies with respect to the assumed ^{108}Pd versus that with respect to the assumed ^{122}Cd is shown. Bottom: projection of these energies on the x-axis (left) and on the y-axis (right). The FWHM of the peaks are 8.6 keV at 435 keV (^{108}Pd) and 10 keV at 570 keV (^{122}Cd).

($\Delta N_\gamma / N_\gamma = 1/\sqrt{N_\gamma}$) and the uncertainties of the Coulomb excitation cross sections of the target nuclei. The latter stem from (i) an uncertainty in the transitional matrix element and (ii) the uncertainty in the range of the scattering angle.

Note that eq. 2.21 has to be modified to take into account the uncertainty of the CD detector efficiency and of the beam purity. Especially for ^{124}Cd the uncertainty of the beam purity is quite large and dominates the overall uncertainty of σ_{ce}^{Cd}. Hence, this nucleus has been investigated again in a later beam time (see section 4.2).

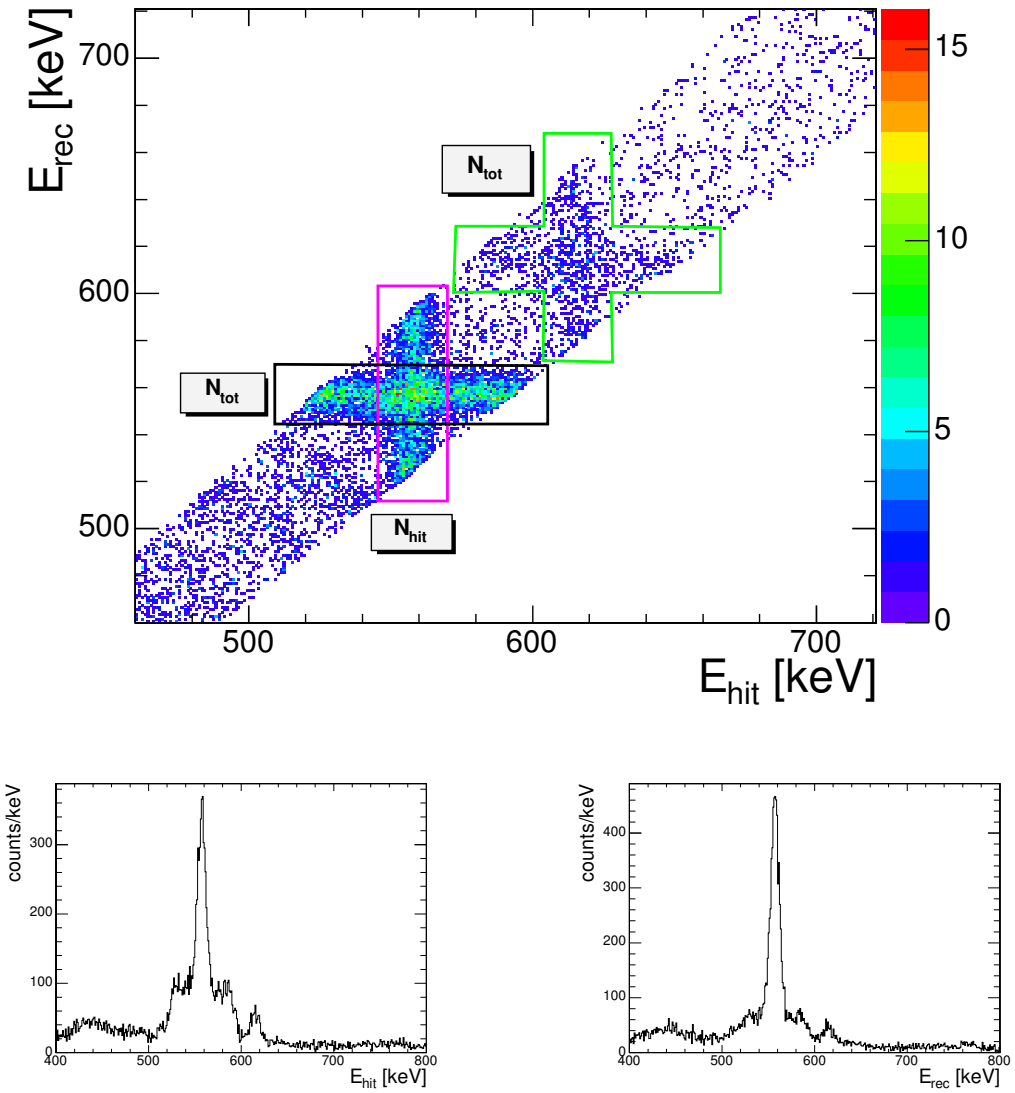

Figure 4.13: Top: the Doppler corrected γ-energies with respect to the assumed ^{104}Pd versus that with respect to the assumed ^{124}Cd is shown. Bottom: projection of these energies on the x-axis (left) and on the y-axis (right). The FWHM of the peaks are 10 keV at 557 keV (^{104}Pd) and 12 keV at 614 keV (^{124}Cd)

.

4.2 Analysis of the ^{124,126}Cd Data

In another attempt to measure Coulomb excitation cross sections for excited states in neutron-rich Cd isotopes, the reactions ^{64}Zn(^{124,126}Cd,^{124,126}Cd*)^{64}Zn* were used.

Results for ^{122,124}Cd

Beam	Method	N_{Cd}	N_{Pd}	ϑ_{CM} [°]	$\sigma_{ce}^{Pd}[b]$	$\sigma_{ce}^{Cd}[b]$	ME($0 \rightarrow 2$) $[eb]$
^{122}Cd	(i)	526	2975	32 - 110	2.78(22)	0.97(10)	0.61(7)
	(ii)	429	2320	80 - 150	1.59(12)	0.58(6)	0.59(7)
	(iii)	718	3882	32 - 150	3.50(20)	1.28(10)	0.61(4)
^{124}Cd	(i)	467	4540	33 - 116	1.58(14)	0.80(20)	0.58(10)
	(ii)	346	3453	80 - 150	0.926(81)	0.45(11)	0.55(10)
	(iii)	763	5633	33 - 150	1.92(14)	1.26(31)	0.67(13)

Table 4.4: Results from the integrated gamma yields for the ^{122,124}Cd runs. Method (i) compares $N'_{hit}(Cd)$ with $N'_{rec}(Pd)$, method (ii) compares $N'_{rec}(Cd)$ with $N'_{hit}(Pd)$ and method (ii) compares $N_{tot}(Cd)$ with $N_{tot}(Pd)$. The resulting transitional matrix elements agree with each other. Their derivation as well as the resulting $B(E2)$ values are discussed in chapter 5.

4.2.1 Particle Spectra

This time the back strips number 8, 9 and 10 in sector 1 and the ring number 14 in sector 2 of the CD detector were malfunctioning[1].

Furthermore, the CD was shielded with a Mylar foil of 1.6 mg/cm^2 to reduce the energy range of the detected particles such that it fits to the energy range of the preamplifiers (see section 3.4). In figure 4.14 the detected particle energy is plotted versus the laboratory scattering angle before and after the beam shift correction. Here, the detected projectiles can be separated from the detected target recoils. Therefore, two separate cuts have been applied.

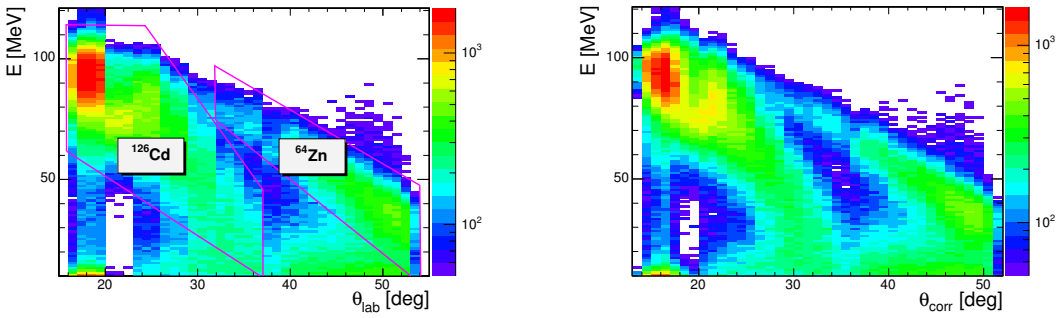

Figure 4.14: The measured particle energy versus scattering angle for ^{126}Cd is shown before (left) and after (right) the beam shift correction. The cuts on the elastically scattered projectiles and recoils are also shown. The missing ring can be seen as decreased intensity at about $\vartheta = 20°$.

The beam shift has been determined similarly to the description in section 4.1 (cf. figure 4.15). The results are summarized in table 4.5 and the corrected angles ϑ_{corr} are again used to assign the particle energy (see section 3.5). The range of the scattering angle that could be used in the analysis is $12.0(24)° \leq \vartheta_{corr} \leq 52.0(12)°$ and

[1]Note that the rings are numbered from 0 for the outermost ring to 15 for the innermost.

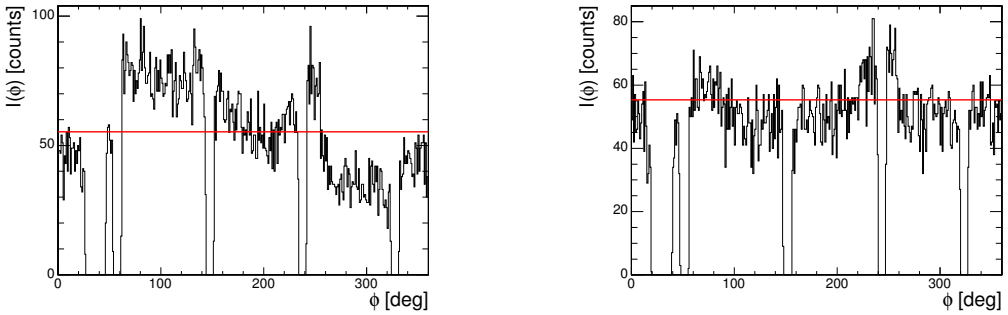

Figure 4.15: The intensity of elastically scattered particles in $24° \leq \vartheta \leq 27°$ before (left) and after (right) correction due to the beam shift for the ^{124}Cd beam. The mean intensity is also shown as red line.

Beam Shift Parameters

Beam	$r[mm]$	$\varphi[°]$
^{124}Cd	2	112.5
^{126}Cd	1	67.5

Table 4.5: The offset of the beam spot with respect to the CD center in polar coordinates for the ^{124,126}Cd runs.

$14.0(24)° \leq \vartheta_{corr} \leq 50.0(13)°$ for ^{124}Cd and ^{126}Cd, respectively. The *event types* are defined differently from the former Cd runs due to the two separate cuts applied here (cf. table 4.6). The number of events per event type are shown in figure 4.16. Only events of type 1, 2 or 3 are used in the further analysis.

Definition of Event Types

Event Type	Projectile Multiplicity	Recoil Multiplicity
0	0	0
1	1	0
2	0	1
3	1	1
4	> 1	> 1

Table 4.6: Different event types according to the number of particle hits in the projectile and recoil cut, respectively.

4.2.2 Beam Purity

The RILIS has again been used as ion source for the ^{124,126}Cd beams which allows the determination of the beam purity by comparing 'Laser On' and 'Laser Off' data.

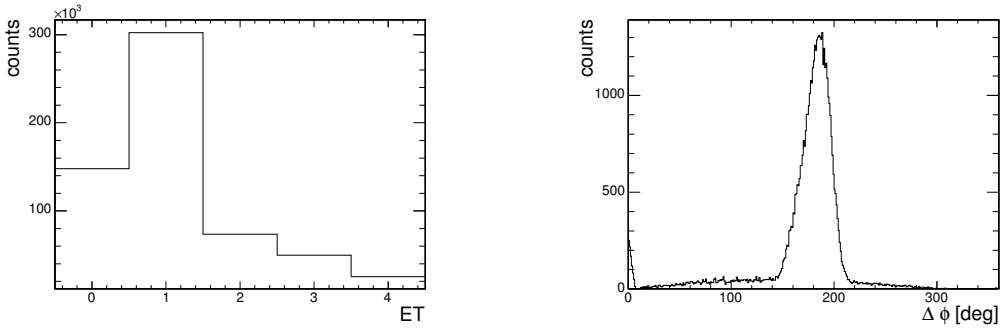

Figure 4.16: Left: The number of events per event type for the ^{126}Cd beam. Note that about 50% of all events are of type 1 whereas only about 4% are of type 4. Right: The difference in the azimuthal angle in case both particles have been detected. Note that $\Delta\varphi = 183 \pm 12°$.

Unfortunately, the yields from the target disexcitation are too small to be analyzed because most of the beam time has been dedicated to pure 'Laser On' runs. Therefore, only the number of elastically scattered beam-like particles (i.e. particles detected in the projectile cut) were used for the comparison (cf. table 4.7). The newly developed quartz transfer line enhanced the beam purity significantly compared to that of the former ^{122,124}Cd runs.

Beam Purity

Beam	N_{ON}	N_{OFF}	R[%]
^{124}Cd	4921	855	83(4)
^{126}Cd	36732	13433	63.4(6)

Table 4.7: Determination of beam purity for ^{124,126}Cd by comparing the elastically scattered beam-like particles during 'Laser On' and 'Laser Off' runs.

4.2.3 Efficiency of the CD Detector

The relative efficiency of the CD detector has been determined for each cut this time. Again the number of particles that have elastically been scattered into an interval $[\vartheta, \vartheta + d\vartheta]$ has been compared to the integrated Rutherford cross section over this interval (cf. figures 4.17 and 4.18).

The resulting efficiencies are shown in figure 4.19. Note that the innermost interval in ϑ is affected by the beam shift and the final beam spot size, hence it will not be covered fully by the active area of the detector. The two innermost intervals are additionally lowered in efficiency due to the missing ring in one sector. The outermost interval is also affected by the beam spot size and the beam shift. This effect is stronger for the ^{124}Cd run due to the larger beam shift. In the middle region the separation between Cd and Zn is not so obvious and the Zn cut gets narrower towards lower angles which is reflected in a decreasing efficiency. The Cd efficiency at about 30° is affected by the geometry of the cut which excludes the low-energetic Cd isotopes.

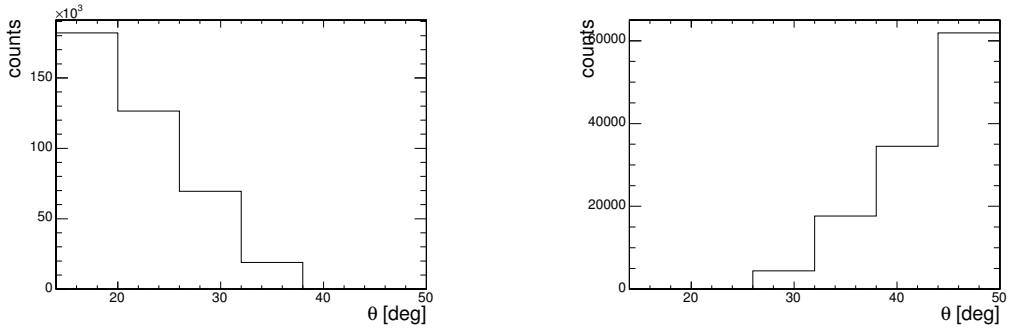

Figure 4.17: The number of elastically scattered projectiles (left) and recoils (right) per ϑ interval in the ^{126}Cd run.

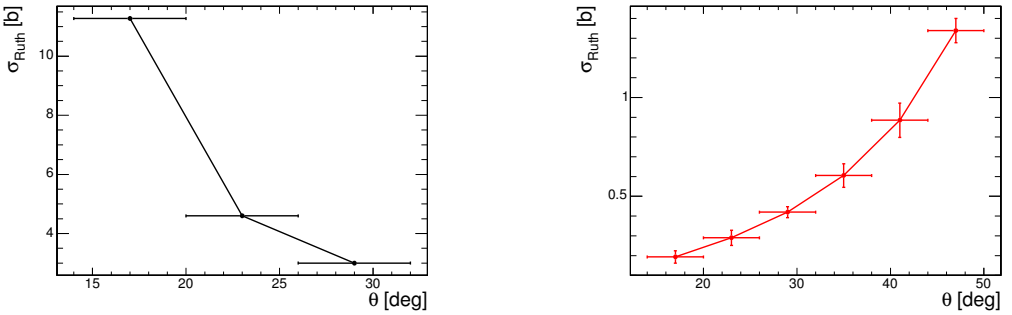

Figure 4.18: The Rutherford cross section for ^{126}Cd (left) and ^{64}Zn (right) integrated over each interval in ϑ.

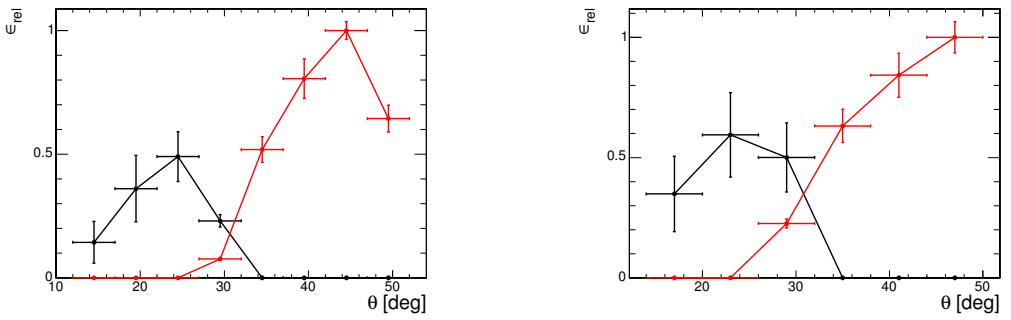

Figure 4.19: Left: The relative efficiencies of the CD detector for the Cd cut (black) and the Zn cut (red) in the ^{124}Cd run. The scattering angle ranges from $12° \leq \vartheta \leq 52°$ in intervals of 5°. Right: The relative efficiencies of the CD detector in the ^{126}Cd run. The scattering angle ϑ ranges from 14° to 50° in intervals of 6°.

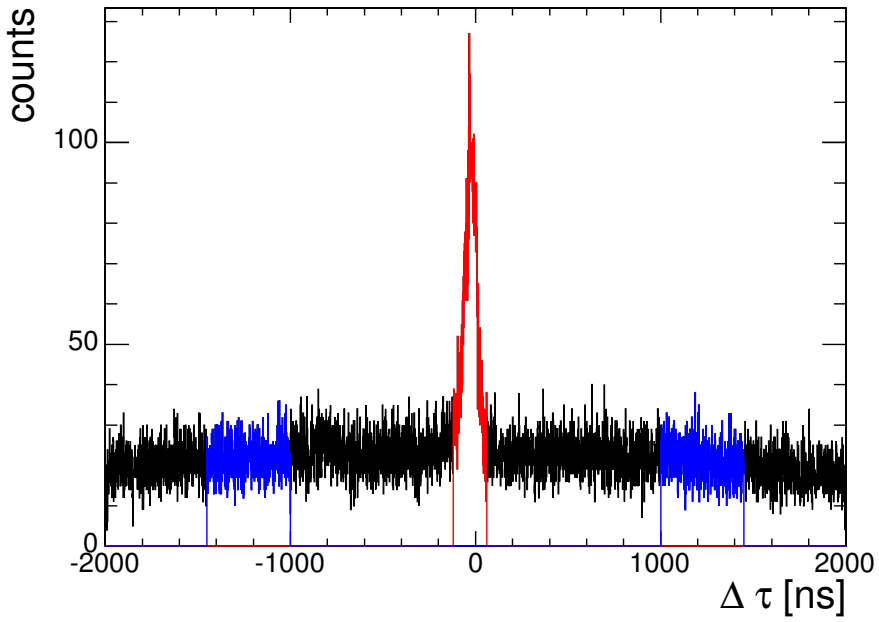

Figure 4.20: The time difference between the detection of particles and γ-rays for the ^{126}Cd run. The prompt peak (red) and the random time gate (blue) are indicated.

4.2.4 Gamma Ray Spectra

As in section 4.1 the time difference between the detection of particles and γ-rays is used to identify γ-rays emitted by the reaction partners (*prompt peak*) and random background radiation (cf. figure 4.20). Since the projectiles and the target recoils can be separated in the CD detector the γ-energies can be Doppler corrected with respect to the corresponding particle. If only one of the reaction partners has been detected (i.e. for event types 1 and 2) the direction and energy of the other one could be reconstructed kinematically and the corresponding γ-energies could be Doppler corrected as well. Depending on the scattering angle ϑ of the detected particle(s) the Doppler corrected γ-rays are weighted with the relative CD efficiency $\epsilon_{1(2)}(\vartheta)$ where the subscript 1 (2) stands for detected projectiles (recoils). The resulting γ-ray spectra can be seen in figure 4.21. The Coulomb excitation cross sections for the first 2^+ states in ^{124,126}Cd have been determined applying eq. 2.21. The gamma yields can be gained by integrating the corresponding peaks in the Doppler corrected γ-ray spectra and the Coulomb excitation cross section $\sigma_{ce}^{(2)}$ of the target nucleus has been calculated using CLX (see section 2.6 for details).

The resulting gamma yields, cross sections and transitional matrix elements for ^{124,126}Cd are summarized in table 4.2.4.

The uncertainties of the Coulomb excitation cross sections of ^{124,126}Cd are again influenced by the statistical errors of the gamma yields, the uncertainties of the CD detector efficiencies and the beam purities and by the uncertainties of σ_{ce}^{Zn}. The latter

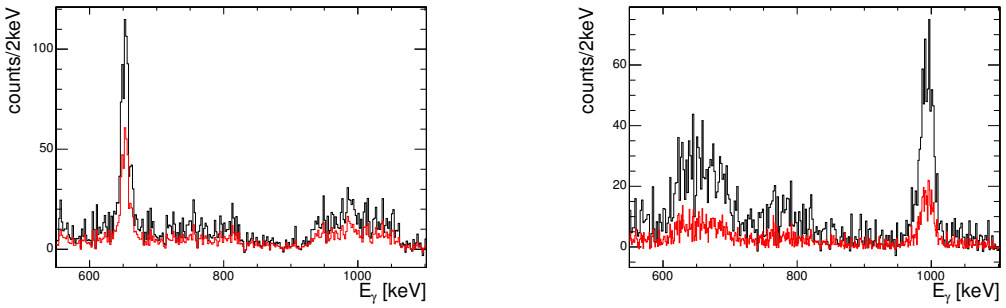

Figure 4.21: The Doppler corrected γ-ray spectra for ^{126}Cd (left) and ^{64}Zn (right). For comparison they are shown with (black) and without (red) efficiency weighting.

Results for ^{124,126}Cd

Beam	N_{Cd}	N_{Zn}	ϑ_{CM} [°]	$\sigma_{ce}^{Zn}[b]$	$\sigma_{ce}^{Cd}[b]$	ME($0 \rightarrow 2$) $[eb]$
^{124}Cd	1007	416	36 - 156	0.31(3)	0.68(9)	0.58(2)
^{126}Cd	965	784	42 - 152	0.31(4)	0.46(6)	0.53(1)

Table 4.8: Results from the integrated gamma yields for the ^{124,126}Cd runs. The resulting transitional matrix elements are also given. Their derivation as well as the resulting $B(E2)$ values are discussed in chapter 5.

depend on the uncertainties of the scattering angles and the transitional matrix element.

4.3 Analysis of the $^{138-142}$Xe Data

The Coulomb excitation cross sections for the first excited states of neutron-rich Xe nuclei with $N > 82$ were examined utilizing the reactions ^{96}Mo($^{138-142}$Xe,$^{138-142}$Xe*)^{96}Mo*.

4.3.1 Particle Spectra

For this beam time the condition of the CD detector has again been examined via the raw energy spectra per ring and strip for each sector. Only the rings number 2 and 5 in sector 0 of the detector were malfunctioning. Furthermore the inner 4 rings were covered by a plug to suppress the high count rates of elastically scattered particles occurring at small scattering angles. Therefore, only the range $30.0(20)° \leq \vartheta \leq 50.0(13)°$ has been used in the analysis. Plotting the particle energy versus the scattering angle allows to identify the projectiles and the target recoils and to apply graphical cuts on these (cf. figure 4.22). The event types are defined according to table 4.6. The number of events per event type is shown in figure 4.23.

The beam shift has been corrected utilizing the same method as for the Cd runs (see section 4.1). The resulting beam shifts (cf. figure 4.24) are summarized in table 4.9.

The particle energy again can be determined from the corrected angles ϑ_{corr} via a kinematical look-up table. In figure 3.14 the difference between the detected and the

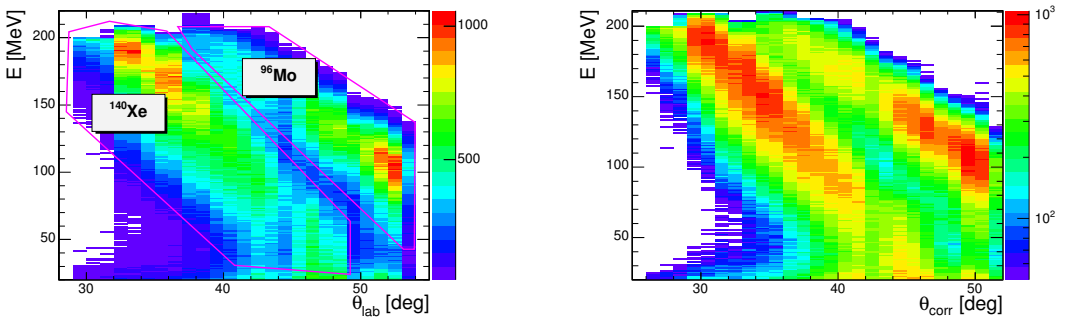

Figure 4.22: The measured particle energy versus scattering angle for ^{140}Xe is shown before (left) and after (right) the beam shift correction. Cuts on elastically scattered projectiles and recoils are also shown. The missing rings 2 and 5 can be seen at about 45° and 50° on the left picture.

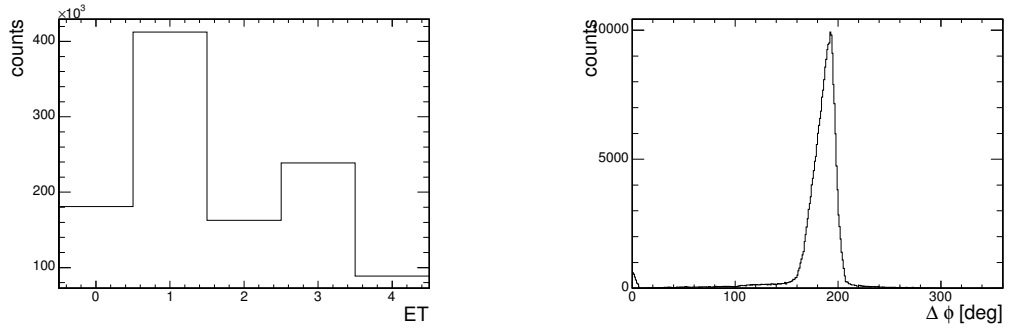

Figure 4.23: Left: The number of events per event type for the ^{140}Xe experiment. Note that 38% of all events are of type 1 whereas only 8% are of type 4 which is considered unphysical and neglected for the further analysis. Right: The difference in φ in case of ET 3 centers at $(180 \pm 10)°$.

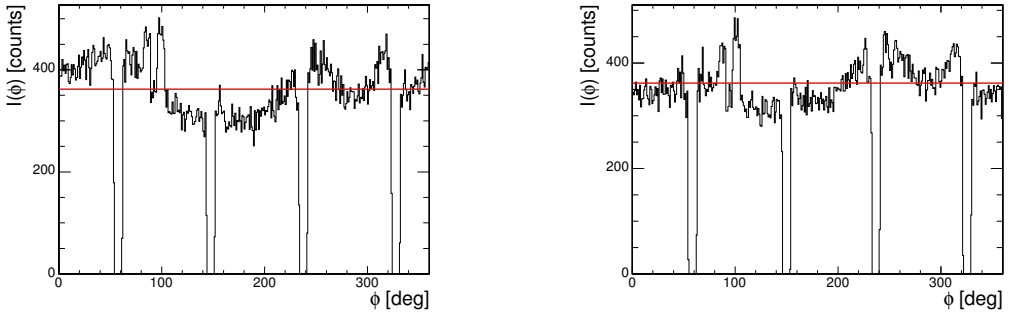

Figure 4.24: The measured intensity of elastically scattered projectiles (^{140}Xe) in $35° \leq \vartheta \leq 37°$ before (left) and after (right) the correction for the beam shift. The mean intensity is shown as red line.

Beam Shift Parameters

Beam		$r[mm]$	φ [°]
^{138}Xe		1	67.5
^{140}Xe	(i)	1	45.0
^{140}Xe	(ii)	1	52.5
^{142}Xe		1	67.5

Table 4.9: The beam shift parameters for the $^{138-142}$Xe runs in polar coordinates. Note that there were two separate runs of ^{140}Xe, (i) before and (ii) after the ^{142}Xe run.

calculated energy can clearly be seen.

The efficiency of the CD detector and the applied cuts on projectiles and recoils has also been determined by comparing the number of elastically scattered projectiles (recoils) in small intervals of ϑ to the corresponding Rutherford cross section $\sigma_{Ruth}(\vartheta)$ (cf. figures 4.25 and 4.26). The resulting relative efficiencies

$$\epsilon_{1(2)}(\vartheta) = N_{1(2)}(\vartheta)/\sigma_{1(2)}(\vartheta)$$

with the subscript 1 (2) standing for the cut on projectiles (recoils) and the maximum efficiency normalized to 1 are shown in figure 4.27. One can again see a drop in efficiency at small scattering angles which is due to the beam shift, the final beam spot size and the inner edge of the CD detector. Note that the energetic cut-off at $\sim$ 200 MeV (see figure 4.27) also reduces the efficiency for both the projectile cut and the recoil cut at lower angles. Furthermore the missing rings affect both efficiencies at $\vartheta \simeq 44°$ and the recoil efficiency at $\vartheta \simeq 48°$.

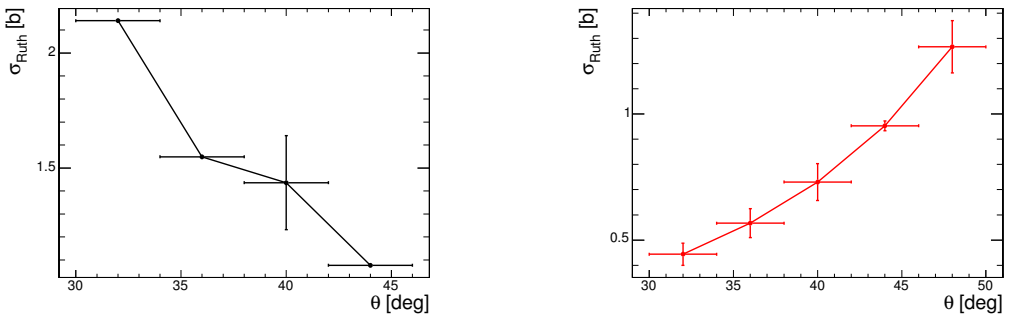

Figure 4.25: The Rutherford scattering cross sections for ^{140}Xe (left) and ^{96}Mo (right) per ϑ interval from 30° to 50°. Note that the projectiles cannot scatter into the outermost ϑ interval.

In order to check the consistency of the data the ratio of the number of elastically scattered projectiles (1) and recoils (2) per angular range $N_{1(2)}(\vartheta)$ is compared to the ratio of the corresponding Rutherford cross sections $\sigma_{1(2)}(\vartheta)$ for events where both the projectile and the recoil were detected. The resulting plot (including statistical errors for the experimental data and uncertainties in ϑ for the cross sections) shows agreement

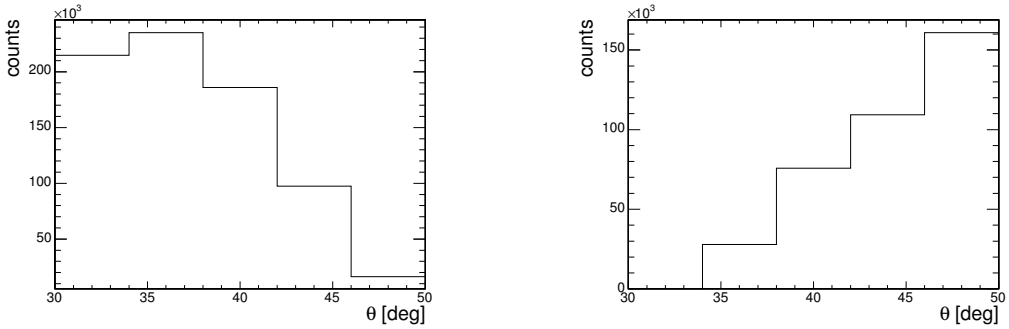

Figure 4.26: Number of elastically scattered projectiles (left) or recoils (right) per ϑ interval from 30° to 50° in the case of ^{140}Xe.

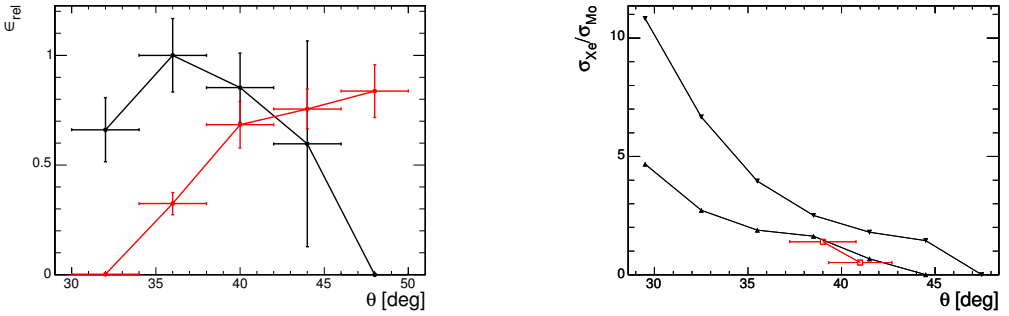

Figure 4.27: Left: Relative efficiency per ϑ interval for ^{140}Xe (black) and ^{96}Mo (red). Note that detected projectiles in the interval $42° \leq \vartheta \leq 46°$ are neglected in the further analysis. Right: Upper and lower limit of the ratio of the Rutherford cross sections (black) and ratio of number of scattered particles (red) for ^{140}Xe.

within the uncertainties between calculation and experimental data (cf. figure 4.27). At lower angles the cut-off in energy for the recoils leads to a greater ratio than expected.

4.3.2 Gamma Ray Spectra

For identifying the γ-rays emitted by the projectiles or recoils correctly the time difference between the detection of particles and γ-rays is shown in figure 4.28. The *prompt peak* and the random time gate are highlighted. As in the Cd runs the random background will be subtracted from the γ-ray spectra taken during the prompt peak. The γ-energies are Doppler corrected (see eq. 3.1) with respect to the projectile and the recoil, respectively. If one of the two reaction partners has not been detected (i.e. $ET = 1$ or 2) its direction and energy can be reconstructed kinematically.

For determining the Coulomb excitation cross section σ_{ce} of the isotope the gamma yields N_γ from the $2_1^+ \rightarrow 0_1^+$ transitions of both the projectile and the target recoil are needed. The Doppler corrected γ-ray spectra with and without background subtraction are shown in figures 4.29 and 4.30. Note that there is hardly any difference in the energy range of the transitions. These spectra have been created not only for the total angular

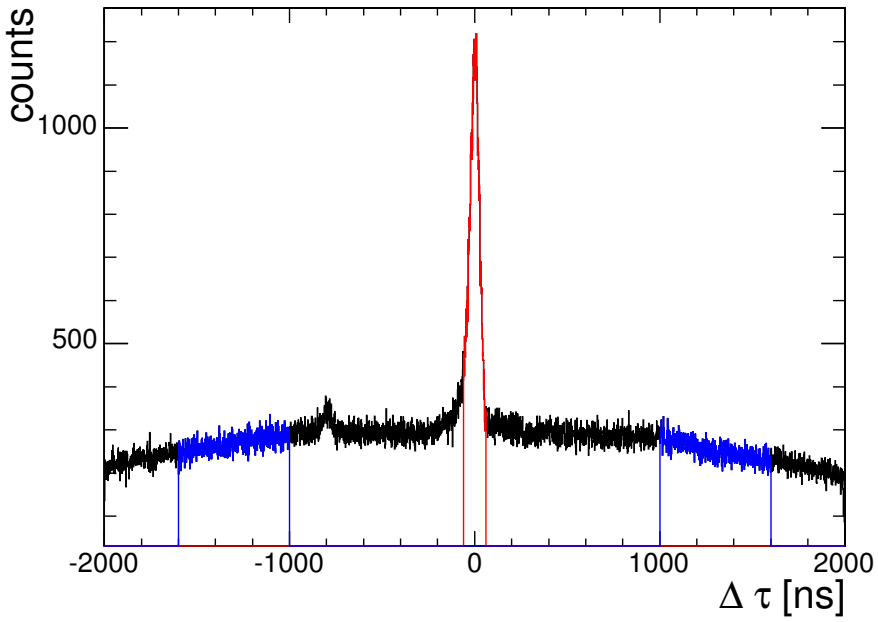

Figure 4.28: Time difference between detected particles and γ-rays for the ^{140}Xe run. The prompt peak (red) and the random time window (blue) are shown.

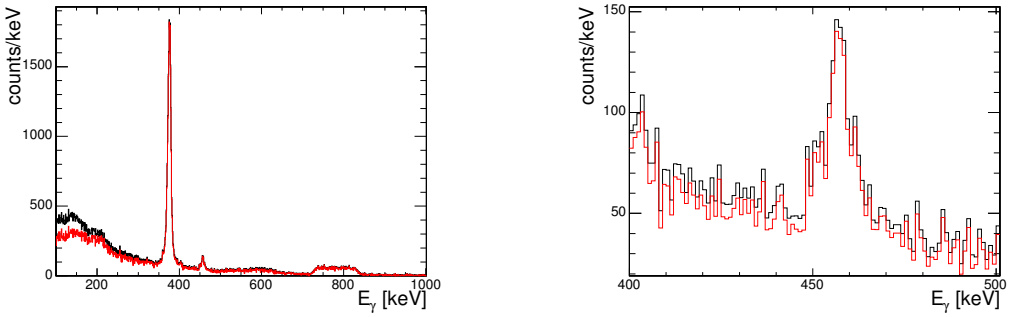

Figure 4.29: The Doppler corrected peaks from the $2_1^+ \rightarrow 0_1^+$ (left) and $4_1^+ \rightarrow 2_1^+$ (right) transition in ^{140}Xe with (red) and without (black) background subtraction.

range but also for intervals in ϑ and weighted with the corresponding particle efficiency $\epsilon_{1(2)}(\vartheta)$. Hence, it is possible to determine the angular distribution of the Coulomb excitation cross section $\sigma_{ce}(\vartheta)$.

In the ^{140,142}Xe case, the peak from the $4_1^+ \rightarrow 2_1^+$ transition can also be seen. Therefore, a determination of $\sigma_{ce}^{2\rightarrow4}$ is possible. The properties of the peaks for all three isotopes are summarized in table 4.10. Integrating these peaks gives the particle efficiency corrected yields N_γ over the total angular range as well as for each interval in ϑ. With this data the Coulomb excitation cross sections can be calculated by comparing

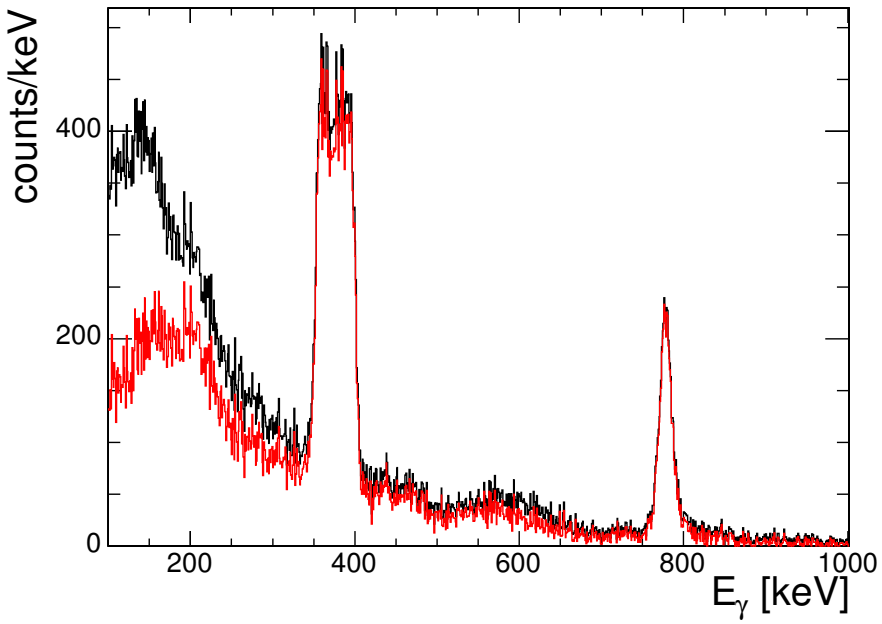

Figure 4.30: The Doppler corrected peak from the $2_1^+ \rightarrow 0_1^+$ transition in ^{96}Mo with (red) and without (black) background subtraction.

Energy Resolutions

Isotope	Transition	E_γ $[keV]$	FWHM $[keV]$
^{138}Xe	$2_1^+ \rightarrow 0_1^+$	588	11
^{140}Xe	$2_1^+ \rightarrow 0_1^+$	376	12
	$4_1^+ \rightarrow 2_1^+$	457	19
^{142}Xe	$2_1^+ \rightarrow 0_1^+$	286	8
	$4_1^+ \rightarrow 2_1^+$	403	8
^{96}Mo	$2_1^+ \rightarrow 0_1^+$	779	20

Table 4.10: Energies and widths of the Doppler corrected transition peaks of both the projectiles and recoils. Note that the $4_1^+ \rightarrow 2_1^+$ transition has been seen for ^{140,142}Xe.

the yields in the Xe peak and the Mo peak (cf. eq. 2.21). The results from the analysis of the data in the ϑ range from 30° to 50° are shown in table 4.11. The relative error of $\sigma_{ce}^{(Xe)}$ is consistent for each interval and in the total angular range. Note that the gamma yield $N_\gamma^{(Mo)}$ is only evaluated for the total range in ϑ and the Coulomb excitation cross section $\sigma_{ce}^{(Mo)}$ is calculated for this range using the Coulomb excitation code CLX. A thorough discussion on the angular distribution of the emitted γ-rays as well as on the resulting $B(E2)$ values is given in chapter 5.

The uncertainties in the Coulomb excitation cross sections of $^{138-142}$Xe are influ-

Results for $^{138-142}$Xe

Beam	ϑ_{lab} [°]	$N^{2\to0}_{\gamma,Xe}$	$N^{4\to2}_{\gamma,Xe}$	$N^{2\to0}_{\gamma,Mo}$	$\sigma^{0\to2}_{ce}[b]$	$\sigma^{2\to4}_{ce}[b]$	$\sigma^{(Mo)}_{ce}[b]$
	30 - 34	1156			0.31(9)		
	34 - 38	1041			0.28(8)		
^{138}Xe	38 - 42	940			0.26(7)		
	42 - 46	894			0.24(7)		
	30 - 50	4030		2031	1.10(32)		0.89(25)
	30 - 34	7031			0.90(27)		
	34 - 38	5906			0.75(23)		
^{140}Xe	38 - 42	5113			0.65(20)		
	42 - 46	1217			0.16(5)		
	30 - 50	19267	2484	4443	2.46(74)	0.317(95)	0.91(27)
	30 - 34	8205			1.23(12)		
	34 - 38	7090			1.06(10)		
^{142}Xe	38 - 42	6322			0.95(10)		
	42 - 46	368			0.06(2)		
	30 - 50	21986	2033	3412	3.29(32)	0.36(12)	0.98(31)

Table 4.11: Gamma yields and Coulomb excitation cross sections for the $^{138-142}$Xe runs. Note that the projectiles cannot scatter into $\vartheta_{lab} \geq 46°$.

enced by the statistical error of the gamma yields, the uncertainties of the efficiencies $\epsilon(\vartheta)$ of the CD detector and the uncertainties of $\sigma^{(Mo)}_{ce}$. The latter are calculated including the uncertainties in the range of ϑ, the uncertainty of the transitional matrix element and the uncertainty of the attenuation parameter λ_2 (see chapter 5). Note that the main contribution stems from the uncertainty of the scattering angle.

4.4 Analysis of the ^{144}Xe Data

Going even further away from the $N = 82$ shell closure the Coulomb excitation cross section of the first excited state in ^{144}Xe has been measured in another beam time. Again a ^{96}Mo target has been used.

4.4.1 Particle Spectra

During this beam time only ring 14 in sector 2 of the CD detector was defect. The CD was also shielded by a degrader foil as in the ^{124,126}Cd runs. Unfortunately, the target recoils can not be identified by plotting the energy of the detected particles versus their scattering angle (cf. figure 4.31). One reason for that is that the Rutherford cross section for ^{96}Mo is 1 - 2 orders of magnitude smaller in the range covered by the CD detector than for larger angles ϑ. Therefore, only a cut on the projectiles has been applied and the *event types* have been defined according to table 4.12. Note that about

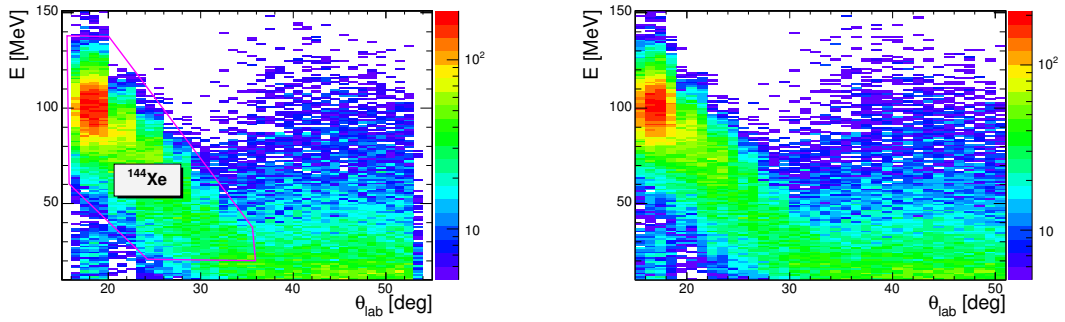

Figure 4.31: The detected particle energy versus the scattering angle is plotted before (left) and after (right) beam shift correction. The applied cut on ^{144}Xe is also shown.

56% of all events are of type 1 and only about 0.5% are of type 2 (cf. figure 4.32). Only events of type 1 are considered for the analysis.

Definition of Event Types

Event Type	Particle Multiplicity
0	0
1	1
2	> 1

Table 4.12: Different event types according to the number of particles detected in the graphical cut.

The beam shift has been corrected using the same method as described in section 4.1 (see figure 4.33), resulting in a radial shift of $r = 2\ mm$ and an angular shift of $\varphi = 18.75°$. This results in a total angular range covered by the CD detector and the cut of $12.0(24)° \leq \vartheta \leq 36.0(18)°$.

4.4.2 Efficiency of the CD Detector

The efficiency of the CD detector and the applied cut has again been determined by comparing the number of elastically scattered particles within an interval $[\vartheta, \vartheta + d\vartheta]$ with the corresponding Rutherford cross section. Both the number of elastically scattered beam-like particles and the Rutherford cross section is shown in figure 4.34 (top). The resulting efficiency is also shown in figure 4.34 (bottom).

4.4.3 Gamma Ray Spectra

Since the target recoils have not been detected their energies and angles were always reconstructed kinematically from the detected angles of the projectiles. The γ-ray spectra were again taken during the *prompt peak* as well as during the random time gate for later background subtraction (cf. figure 4.35).

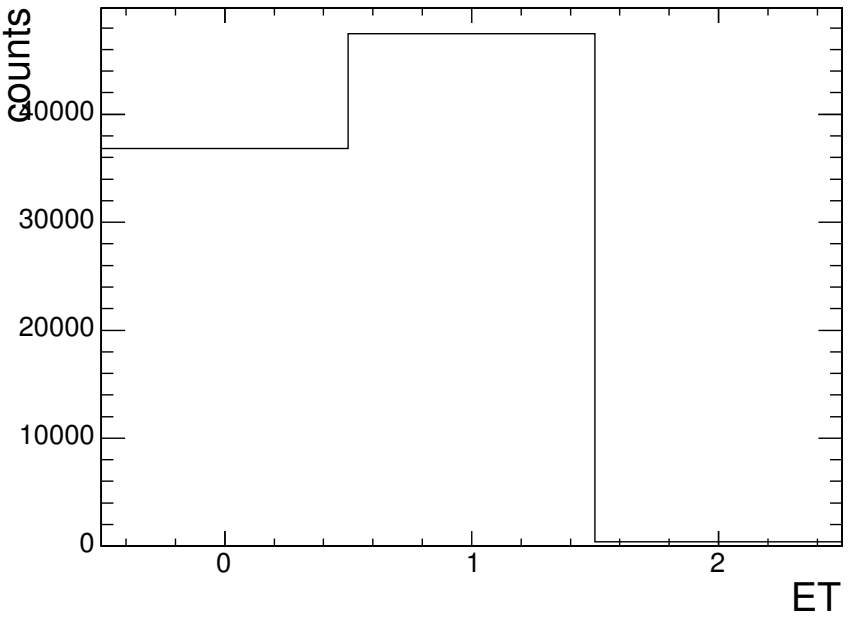

Figure 4.32: The number of events per event type. Only ET 1 is taken into account for the analysis.

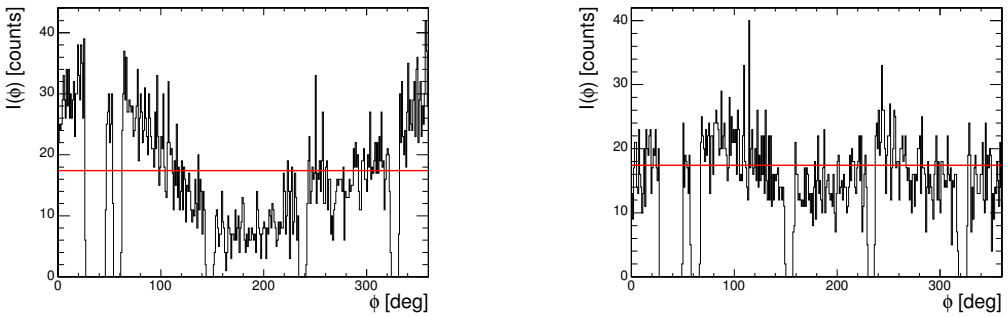

Figure 4.33: The intensity of elastically scattered projectiles in the range $24° \leq \vartheta \leq 27°$ before (left) and after (right) beam shift correction. The mean intensity is also shown (red line).

In the resulting Doppler corrected and efficiency weighted γ-ray spectra the peak from the $2_1^+ \rightarrow 0_1^+$ disexcitation of ^{96}Mo can hardly be seen (see figure 4.36).

Therefore, only a lower limit of $\sigma_{ce}^{0\rightarrow 2}$ could be determined by assuming the number of counts in the energy region from 720 keV to 840 keV to be the upper limit of the gamma yield from the target disexcitation. The results are summarized in table 4.13. Note that the half-live of $T_{1/2} = 388(7)\ ms$ for ^{144}Xe is of the same order of magnitude as the breeding time $\tau_{breed} = 204.1\ ms$. Therefore, the decay of ^{144}Xe during that time

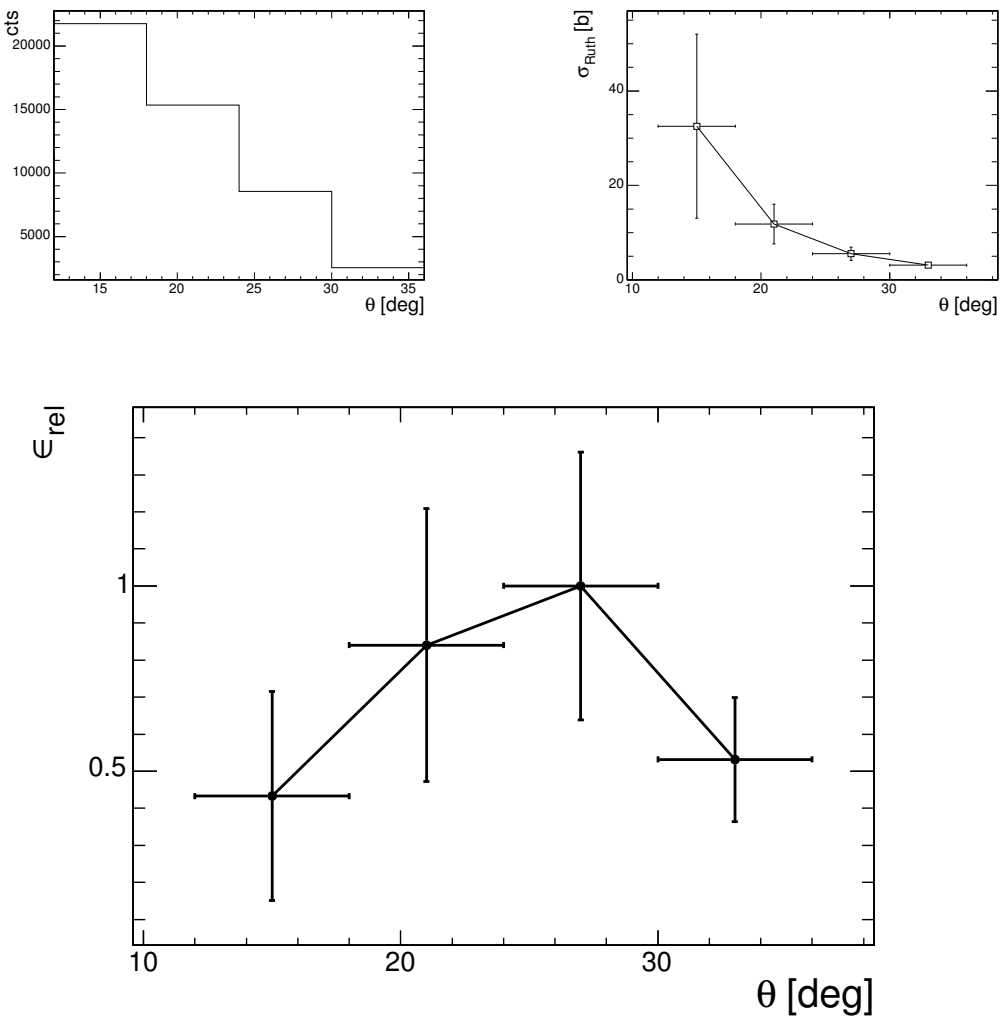

Figure 4.34: Top: The number of elastically scattered projectiles in four intervals of 6° ranging from $12° \leq \vartheta \leq 36°$ (left) and the Rutherford cross section of ^{144}Xe in this range is shown (right). Bottom: The resulting relative efficiency of the CD detector and the applied cut. The efficiency drops at both ends of the cut due to the beam spot size and the shift of the beam spot position. At about 20° the missing ring in sector 2 affects the efficiency.

has to be taken into account, resulting in a beam purity of $R = 65.8(5)\%$ at the target.

The uncertainty of the Coulomb excitation cross section of ^{144}Xe is mainly influenced by the statistical error of the gamma yields. The uncertainties of the CD detector efficiency, the beam purity and of σ_{ce} (Mo) are also taken into account. As in the former Xe runs, $\Delta\sigma_{ce}(Mo)$ depends mainly on the uncertainty in ϑ, although the uncertainties in the transitional matrix element and in λ_2 (see chapter 5) are also taken into account.

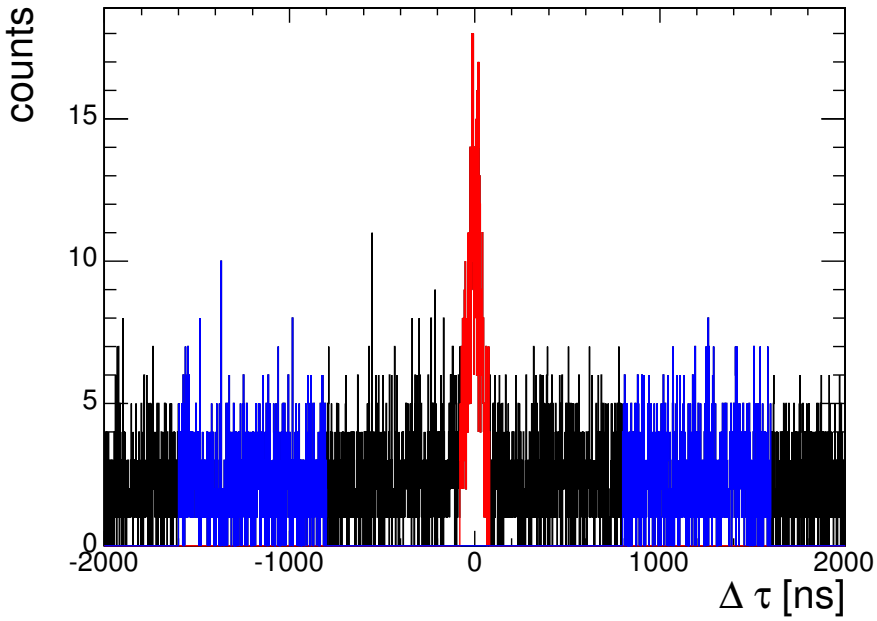

Figure 4.35: The time difference between the detection of particles and γ-rays is shown. The prompt peak (red) and the random time gate (blue) are indicated.

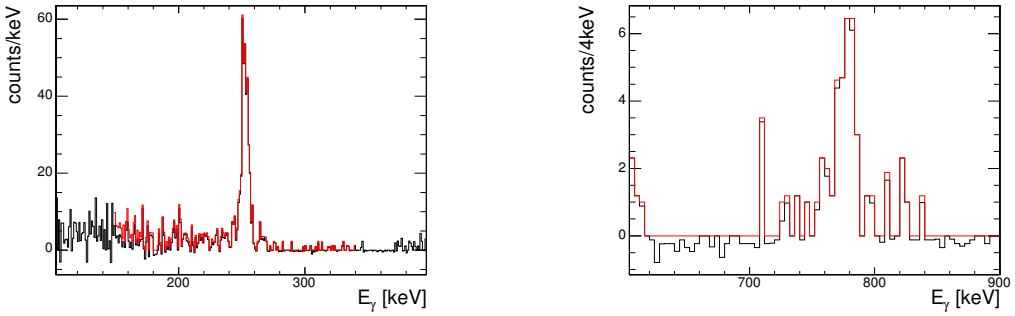

Figure 4.36: The Doppler corrected γ-ray spectrum with respect to the detected ^{144}Xe (left) and with respect to the reconstructed ^{96}Mo (right) is shown with (black) and without (red) random background subtraction. The peak from the $2_1^+ \rightarrow 0_1^+$ transition in ^{144}Xe at 252 keV (FWHM $\sim$ 6 keV) can clearly be seen. The peak of the same disexcitation in ^{96}Mo at about 780 keV is more ambiguous. Here the number of counts in the range from 720 keV to 840 keV is taken as maximal gamma yield.

Results for ^{144}Xe

Beam	ϑ_{CM} [°]	$N_{\gamma,Xe}$	$N_{\gamma,Mo}$	σ_{ce} (Mo) [b]	σ_{ce} (Xe) [b]	ME($0 \rightarrow 2$) [eb]
^{144}Xe	30 - 98	267	39	1.16(14)	5.9(13)	0.83(17)

Table 4.13: Summary of the results from the analysis of the Doppler corrected γ-ray spectra for ^{144}Xe. The cross section of the target and the transition matrix element in Xe have been determined using CLX.

—If it was so, it might be; and if it were so, it would be; but as it isn't, it ain't. That's logic.

Tweedledee in *Through the Looking-Glass, and What Alice Found There* by Lewis Carroll (1832-1898)

5 Results & Discussion

5.1 Results

In chapter 4 the Coulomb excitation cross sections of the nuclides under investigation have been determined from the experimental data. The aim of this work is now to extract the $B(E2)$ values for these nuclides. This can be achieved by using the computer code CLX (see section 2.6). The transitional matrix element, which is one of the input parameters of CLX, is linked to the $B(E2)$ value via eq. 2.11. Therefore, by varying this input parameter until the experimentally determined Coulomb cross section is reproduced, the corresponding $B(E2)$ value can be determined.

5.1.1 Results for $^{122-126}$Cd

The Coulomb excitation cross sections are calculated in two different ranges of the scattering angle ϑ, taking into account the uncertainty $\Delta\vartheta$ due to the strip width, the beam spot size and the distance between target and CD detector (see section 3.5). In figure 5.1 the calculated Coulomb excitation cross sections for ^{122}Cd are shown with respect to ME($0 \rightarrow 2$). The experimentally determined value is also shown. The corresponding interval of ME($0 \rightarrow 2$) for which the calculated and the experimental value agree can be determined by linear interpolation. The $B(E2)$ values are then determined using eq. 2.11.

The same procedure has been applied to the data for ^{124,126}Cd and the results are summarized in table 5.1. Note that the second measurement for ^{124}Cd significantly reduced the relative error of the $B(E2)$ value (see section 4.2). The agreement of the three different methods applied for the determination of the Coulomb excitation cross sections in the ^{122,124}Cd beam time (see section 4.1) has already been shown in table 4.4. Here, only the value determined for the full statistics is given.

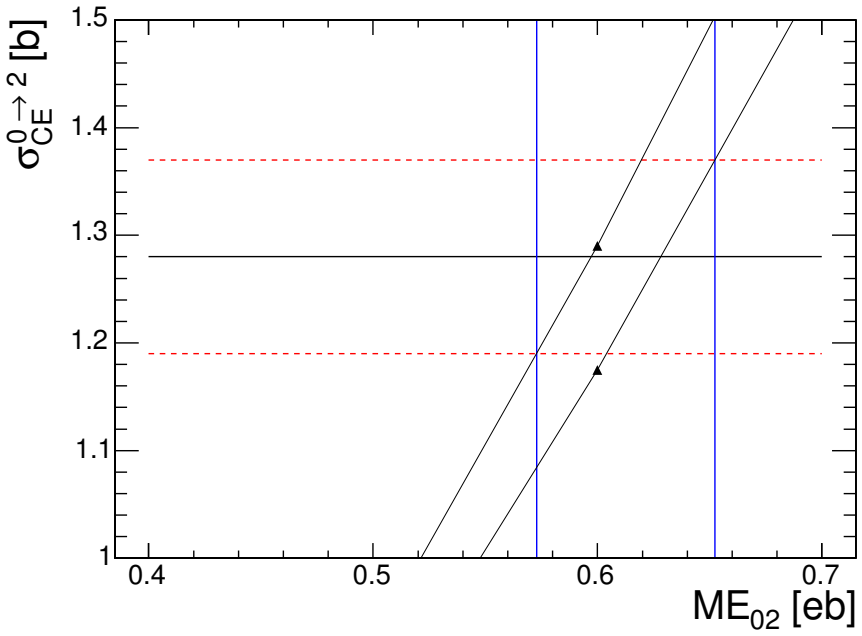

Figure 5.1: The dependency of the Coulomb excitation cross section $\sigma_{ce}^{(Cd)}$ on the transitional matrix element is calculated with CLX. The two graphs (black triangles) correspond to the upper and lower limit, taking into account the uncertainties of $\sigma_{ce}^{(Pd)}$ and of the scattering angle ϑ. The upper and lower limit of the experimentally determined cross section (red dashed lines) and the interval of ME($0 \rightarrow 2$) for which both agree (blue lines) is also shown.

$E2$ **Transition Strengths of** $^{122-126}$**Cd**

Isotope	$E_\gamma(2_1^+ \rightarrow 0_{g.s.}^+)[keV]$	$B(E2)[e^2b^2]$	$B(E2)_{exp}/B(E2)_{sys}$
^{122}Cd	571.6	0.37(5)	1.0(2)
^{124}Cd	614.6	0.45(17)	1.4(6)
		0.34(2)	1.1(2)
^{126}Cd	653.3	0.28(1)	1.1(2)

Table 5.1: The transitional matrix elements and resulting $B(E2)$ values for $^{122-126}$Cd, assuming $\beta = 0$. A comparison of the experimentally determined $B(E2)_{exp}$ values with those derived by the modified Grodzins rule $B(E2)_{sys}$ is also given. The $B(E2)$ value of ^{124}Cd has been measured in two independent experiments, hence both values are given here.

5.1.2 Results for $^{138-144}$Xe

In the $^{138-142}$Xe data the angular distribution of the emitted γ-rays and the deorientation effect (see section 2.3) have been taken into account for the further analysis. In ^{140,142}Xe the γ-rays from the $4_1^+ \rightarrow 2_1^+$ transition have also been observed. This feeding of the 2_1^+ state has been taken into account for the determination of $\sigma_{ce}^{0\rightarrow 2}$.

The corresponding Coulomb excitation cross section $\sigma_{ce}^{2\to4}$ could also be determined. The CLX calculations have to reproduce both cross sections with the same set of input parameters. Furthermore the influence of the diagonal matrix elements has also been examined.

Angular Distribution of γ-Rays

Since the γ-rays are not emitted isotropically, their angular distribution has been examined more closely. The coincident disexcitation γ-rays have been divided into six groups corresponding (i) to the forward and backward direction of the gamma detectors and (ii) to three different ranges of the particle scattering angle ϑ.

The data has subsequently been normalized to the integrated gamma yield over φ and plotted with respect to $\delta\phi = \varphi - \phi$. Here, φ denotes the azimuthal angle of the detected particle whereas ϕ denotes that of the detected γ-ray. A theoretical angular distribution has been calculated with CLX (see section 2.6). These calculated Coulomb excitation cross sections have also been normalized to their integrated values over φ. The influence of the deorientation effect can clearly be seen in figure 5.2.

By varying the attenuation parameter λ_2 (cf. section 2.5) this distribution has then been optimized, i.e. the χ^2 value of its fit to the data has been minimized. The resulting values of λ_2 are summarized in table 5.2.

The uncertainty of the cross section for ^{96}Mo is then influenced by three factors: (i) the uncertainty in the range of ϑ, (ii) the uncertainty of the transitional matrix element ME($0 \to 2$)= 0.520(4) eb and (iii) the uncertainty in $\lambda_2 = 0.23^{+0.33}_{-0.20}\ ps^{-1}$. The resulting total error is dominated by the first of these.

Attenuation Parameters for $^{138-144}$Xe

Isotope	$E_\gamma(2_1^+)$ $[keV]$	λ_2 $[ps^{-1}]$
^{138}Xe	588.8	$0.08^{+1.42}_{-0.074}$
^{140}Xe	376.7	$0.046^{+0.354}_{-0.036}$
^{142}Xe	287.2	$0.026^{+0.174}_{-0.02}$
^{144}Xe	252.6	*0.015(11)*

Table 5.2: The values of λ_2 for the Xe isotopes as estimated from the fit of the calculated angular distribution of emitted γ-rays to the data (see figure 5.2). Note that the value for ^{144}Xe is only a linear interpolation from the previous three values.

The $0_1^+ \to 2_1^+$ Transitional Matrix Element

The transitional matrix elements ME($0 \to 2$) for the Xe isotopes can be extracted from the experimentally determined cross sections $\sigma_{ce}^{0\to2(\to4)}$ in a similar way as for the Cd isotopes.

In figure 5.3 the dependence of the Coulomb excitation cross sections for ^{140}Xe on this matrix element is shown. Note that for ^{140,142}Xe both cross sections have to be reproduced, whereas for ^{138}Xe only $\sigma_{ce}^{0\to2}$ has been determined. Again, the calculations take into account the uncertainty in the range of the scattering angle.

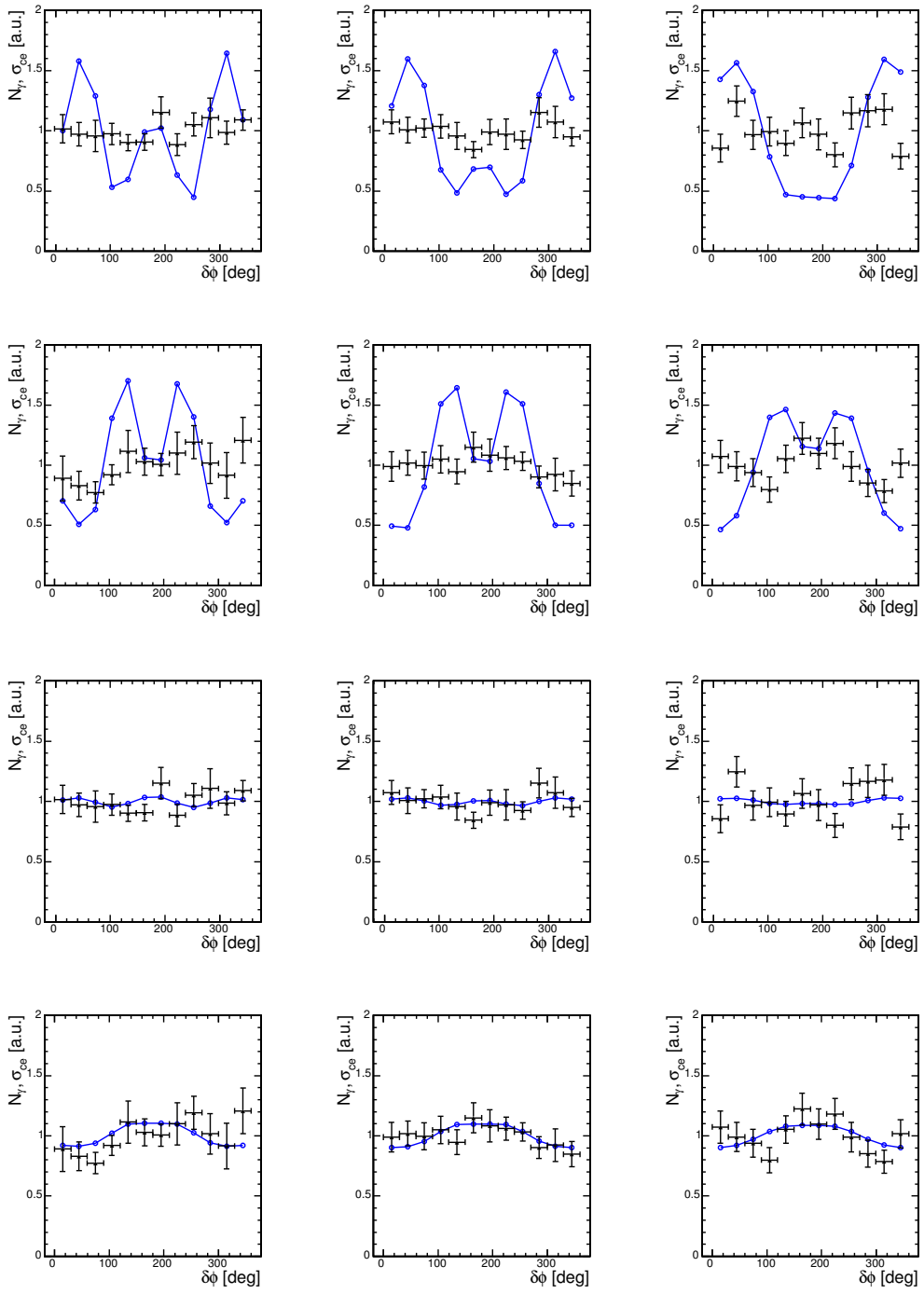

Figure 5.2: The first two rows show the angular distribution of the γ-rays emitted by ^{140}Xe (black dots) in forward (upper row) and backward (lower row) direction compared to a theoretical calculation (blue line) for $\lambda_2 = 0.0\ ps^{-1}$, i.e. without deorientation. The lower two rows show the same distribution compared to a theoretical calculation for $\lambda_2 = 0.046\ ps^{-1}$ (best fit). The three columns correspond to the three intervals in ϑ ranging from 28.0° to 34.5°, 34.5° to 41.0° and 41.0° to 47.5°, respectively.

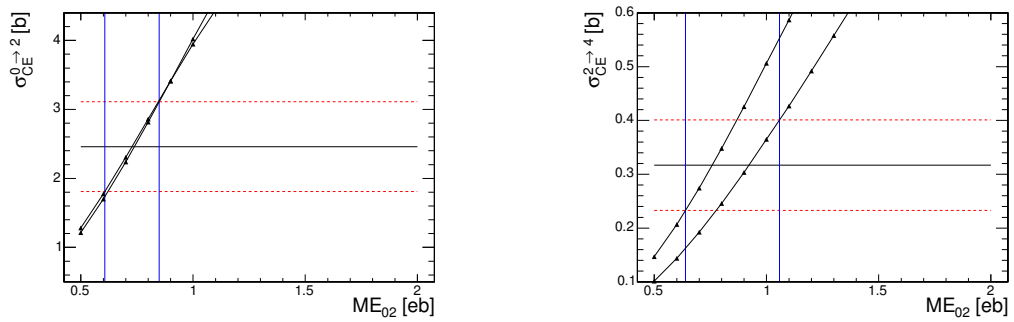

Figure 5.3: The dependence of $\sigma_{ce}^{0\to 2}$ (left) and $\sigma_{ce}^{2\to 4}$ (right) on ME($0 \to 2$) for ^{140}Xe is shown. The two graphs correspond to the uncertainty in the scattering angle ϑ. The experimental values including their uncertainties (red dashed lines) are also shown. Blue lines indicate the interval of agreement between calculated and experimentally determined cross sections.

The diagonal matrix element ME($2 \to 2$), which is linked to the quadrupole deformation parameter β via eq. 2.18, is set to zero (assuming a spherically shaped nucleus). The value for ME($2 \to 4$)= 1.25 *eb* for ^{140}Xe is taken from Lindroth et al. (1999) and the diagonal matrix element for the 4_1^+ state is set to ME($4 \to 4$)= 4.0 *eb*. An agreement for both cross sections can be seen for values of ME($0 \to 2$) between 0.63 *eb* and 0.85 *eb*.

Influence of the Quadrupole Moment

However, the assumption of a spherical shape might not be justified for the neutron-rich Xe isotopes. Therefore, the influence of non-vanishing quadrupole moment on the Coulomb excitation cross sections has to be examined. In figure 5.4 the rather strong dependence of σ_{ce} for ^{140}Xe on the deformation parameter β can be seen. The transitional matrix element ME($0 \to 2$) is kept constant at 0.70 *eb* in agreement with the above considerations. The values of ME($2 \to 4$) and ME($4 \to 4$) are kept constant. The deformation parameter is varied between -0.25 and +0.25, which is a reasonable interval since nuclei in the vicinity of shell closures are usually not strongly deformed. Note that the cross sections agree for $\beta \gtrsim -0.06$.

Higher-order Matrix Elements

For ^{138}Xe these considerations are sufficient since $\sigma_{ce}^{0\to 2}$ does not depend on the higher matrix elements ME($2 \to 4$) and ME($4 \to 4$). But for ^{140,142}Xe the dependence of $\sigma_{ce}^{2\to 4}$ on these matrix elements has been examined (cf. figure 5.5). Note that the diagonal matrix element ME($4 \to 4$) in ^{140}Xe has to be larger than 2 *eb* for the calculated cross section to be in agreement with the experimental determined value. Here, β is again chosen to be zero, ME($0 \to 2$) is kept at 0.70 *eb* and ME($2 \to 4$) = 1.25 *eb*.

These considerations show that all four input parameters to CLX (i.e. the transitional matrix elements $\langle J+2||\mathcal{M}(E2)||J\rangle$ for $J = 0, 2$ and the diagonal matrix elements $\langle J||\mathcal{M}(E2)||J\rangle$ for $J = 2, 4$) have to be varied within reasonable ranges and the agreement of the calculated Coulomb excitation cross sections with the experimental values

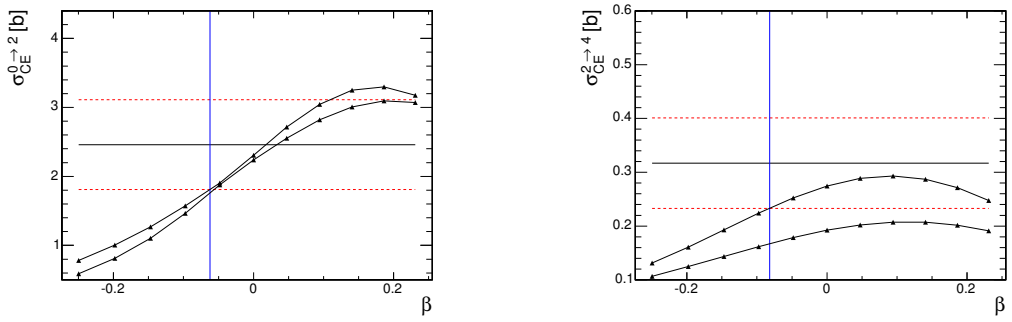

Figure 5.4: The calculated Coulomb excitation cross sections for the $0_1^+ \to 2_1^+$ (left) and $2_1^+ \to 4_1^+$ (right) transition in ^{140}Xe versus the quadrupole deformation parameter. The experimental values including uncertainties (red dashed lines) are also shown. The blue lines indicate the minimal value of β needed to reproduce the experimental cross sections.

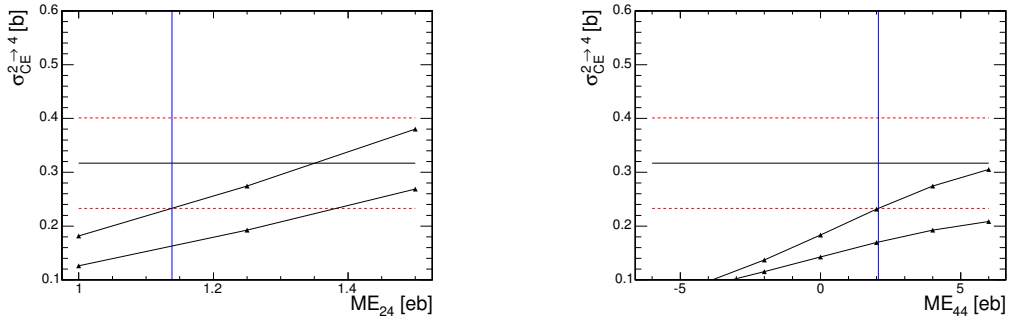

Figure 5.5: The calculated Coulomb excitation cross sections for the $2_1^+ \to 4_1^+$ transition in ^{140}Xe versus the transitional (left) and versus the diagonal (right) matrix element. The two graphs correspond to the uncertainty in the scattering angle ϑ. The experimental value including its uncertainty (red dashed lines) is also shown. The minimal values of the matrix elements needed for reproducing the experimental result is indicated (blue lines).

has to be checked for each combination of these. This has been done for $^{138-142}$Xe and the paramater ranges are summarized in table 5.3.

Ranges of the Input Parameters

ME$(0 \to 2)$ $[eb]$	ME$(2 \to 2)$ $[eb]$	β	ME$(2 \to 4)$ $[eb]$	ME$(4 \to 4)$ $[eb]$
0.5 to 2.0	-5 to +5	-0.25 to +0.25	1.0 to 1.5	-6 to +6

Table 5.3: The ranges of the input parameters for the CLX calculations for $^{138-142}$Xe.

Another constraint on ME$(0 \to 2)$ and ME$(2 \to 2)$ can be found from the experimentally determined Coulomb excitation cross sections $\sigma_{ce}^{0\to 2}$ within smaller ranges of ϑ, i.e. from its angular distribution $\sigma_{ce}(\vartheta)$. Since the experimental value has to be reproduced in each scattering interval for the same combination of input parameters

this sets more severe limits on the matrix elements (cf. figures 5.6 to 5.8).

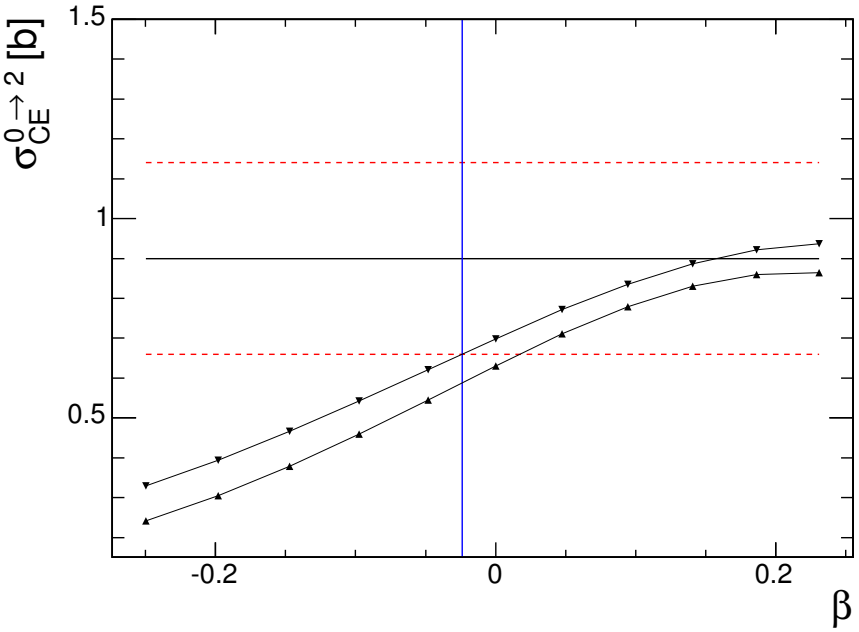

Figure 5.6: The calculated cross sections $\sigma_{ce}^{0\to2}$ for ^{140}Xe in the range $30° \leq \vartheta \leq 34°$ with ME$(0 \to 2) = 0.70\ eb$ is plotted. The intersection with the lower experimental limit is shown as well (blue line).

Conclusion

There are now three (or two, in the case of ^{138}Xe) independent constraints on the quadrupole deformation parameter with respect to the transitional matrix element ME$(0 \to 2)$ for each combination of the other two matrix elements (cf. figure 5.9). These stem from (i) reproducing $\sigma_{ce}^{0\to2}$ for $^{138-142}$Xe in the total angular range, (ii) reproducing the angular distribution $\sigma_{ce}^{0\to2}(\vartheta)$ in all three Xe isotopes and (iii) reproducing $\sigma_{ce}^{2\to4}$ for ^{140,142}Xe.

Merging the overlaps of these allowed regions for all combinations of ME$(2 \to 4)$ and ME$(4 \to 4)$ under consideration gives a conclusive summary of the maximal allowed values of the transitional matrix element ME$(0 \to 2)$ and the diagonal matrix element ME$(2 \to 2)$ (cf. figures 5.10 to 5.12).

Evaluating these results for $\beta = 0$ gives upper and lower limits for ME$(0 \to 2)$ which leads to $B(E2)$ values that can now be compared to those of neighbouring isotopes (cf. figure 5.13). It can then be shown that for $^{138-144}$Xe the measured $B(E2)$ values agree with the modified Grodzins rule and - for ^{140}Xe - also with experimental data from Lindroth et al. (1999). These results are summarized in table 5.4.

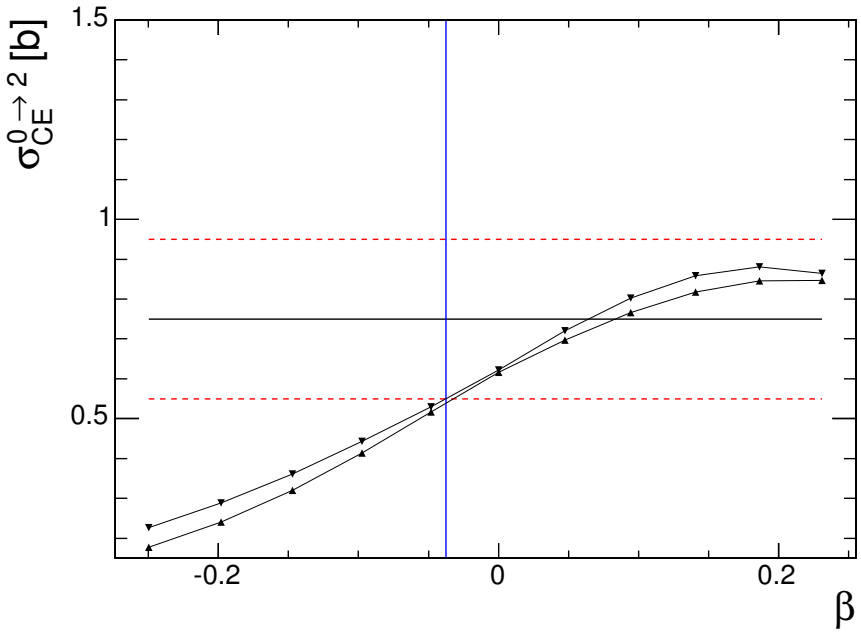

Figure 5.7: The upper and lower limits of the experimental (red dashed lines) and calculated cross sections $\sigma_{ce}^{0\rightarrow 2}$ versus β in the range $34° \leq \vartheta \leq 38°$ are shown for ^{140}Xe with ME$(0 \rightarrow 2)$ $= 0.70\ eb$. The lower limit of β for agreement between experiment and calculation is indicated (blue line).

Results for $^{138-144}$Xe

Isotope	$E_\gamma(2_1^+ \rightarrow 0_{g.s.}^+)[keV]$	$B(E2; 0_{g.s.}^+ \rightarrow 2_1^+)\ [e^2b^2]$	$B(E2)_{exp}/B(E2)_{sys}$
^{138}Xe	588.8	0.34(8)	0.83(20)
^{140}Xe	376.7	0.59(7)	1.0(2)
^{142}Xe	287.2	0.66(9)	1.2(3)
^{144}Xe	252.6	0.69(28)	1.0(2)

Table 5.4: The resulting $B(E2)$ values for $^{138-142}$Xe and a comparison for the estimation from the modified Grodzins rule. Here, $\beta = 0$ has been assumed.

The $4_1^+ \rightarrow 2_1^+$ Transition

Since the $4_1^+ \rightarrow 2_1^+$ transition peak has been observed in the Doppler corrected γ-energy spectra of ^{140,142}Xe, the Coulomb excitation cross section $\sigma_{ce}^{2\rightarrow 4}$ has been ascertained for these nuclei.

The determination of the corresponding $B(E2; 4 \rightarrow 2)$ value is rather difficult, since this cross section depends not only on the transitional matrix element ME$(2 \rightarrow 4)$, but on all four parameters ME$(J_i \rightarrow J_f)$ under investigation here.

Therefore, the range of ME$(2 \rightarrow 4)$ used in the calculations in this work is fully

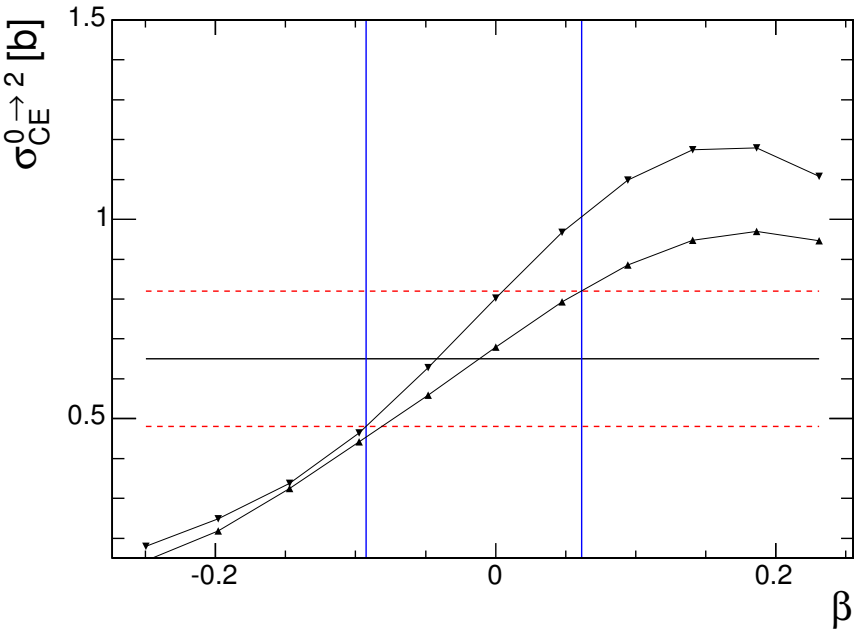

Figure 5.8: The theoretical as well as the experimental upper and lower limits of $\sigma_{ce}^{0\rightarrow 2}$ versus β for ^{140}Xe in the range $38° \leq \vartheta \leq 42°$ are shown. The interval of agreement between both in β is indicated (blue lines). A transitional matrix element of ME$(0 \rightarrow 2) = 0.70\ eb$ is assumed.

suitable for both nuclei, depending on the choice of the other three matrix elements. However, under certain assumptions the ratio $B(E2; 4 \rightarrow 2)/B(E2; 2 \rightarrow 0)$ could be estimated quite well (see table 5.5). Note that in the simple picture of multi-phonon excitations in ideal vibrational nuclei this ratio should be exactly 2.0 (see Casten (2000)).

5.2 Discussion

In the framework of this thesis $B(E2)$ values of neutron-rich Cd and Xe isotopes both below and above the shell closure at $N = 82$ have been measured by means of low-energy Coulomb excitation experiments. For all investigated nuclei the experimentally determined $B(E2)$ values are in the range of those derived via the modified Grodzins rule, assuming a vanishing or only small quadrupole moment. Note that this assumption is in agreement with the QRPA[1] calculations performed by Terasaki et al. (2002) which could reproduce the anomalous low $B(E2)$ value of ^{136}Te.

Analyzing the results for a larger range of deformation parameters β leads to larger regions of possible transitional matrix elements ME$(0 \rightarrow 2)$ (cf. figures 5.10 to 5.12). These regions are compared to the expectations from the modified Grodzins rule (see table 5.6) or to experimental data (in the case of ^{140}Xe). Note that a relative uncertainty

[1] **Q**uasi-particle **R**andom **P**hase **A**pproximation

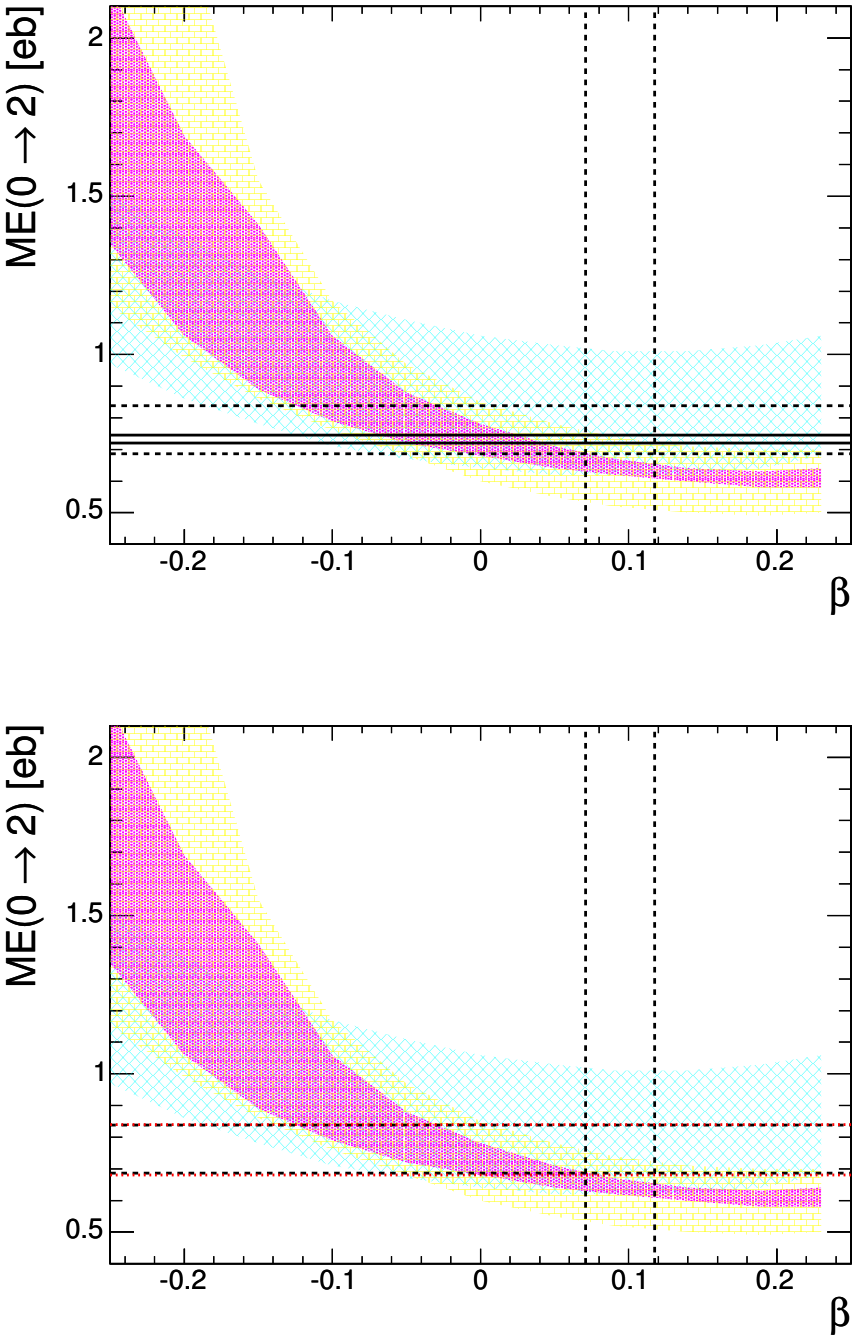

Figure 5.9: The allowed regions for ME(0 → 2) versus β from all three investigations, reproducing $\sigma_{ce}^{0\to2}$ (yellow), $\sigma_{ce}^{2\to4}$ (cyan) and $\sigma_{ce}^{0\to2}(\vartheta)$ (magenta). The constraints from the IBA model (dashed lines, both) and the result from Lindroth et al. (1999) (solid lines, top) as well as the value from a modified Grodzins rule ± 20% (red lines, bottom) are also shown. The other two parameters are kept at ME(2 → 4)= 1.25 *eb* and ME(4 → 4)= 4.0 *eb*.

Ratios of $B(E2)$ values for IBA constraints

Isotope	β	ME$(2 \rightarrow 4)$ $[eb]$	$B(E2;4 \rightarrow 2)/B(E2;2 \rightarrow 0)$
	-0.15	1.50	0.70(14)
	-0.10	1.50	1.18(22)
	-0.05	1.50	1.77(35)*†
^{140}Xe	0.00	1.50	2.35(52)†
	0.05	1.25	1.77(37)*†
		1.50	2.74(55)
	0.10	1.25	2.09(46)*†
		1.50	3.00(57)
	0.15	1.25	2.26(49)†
		1.50	3.25(60)
	-0.15	1.25	0.36(16)
		1.50	0.59(34)
	-0.10	1.25	0.73(23)
		1.50	1.08(35)*
	-0.05	1.25	1.03(28)
		1.50	1.48(36)*
		1.00	0.76(20)
^{142}Xe	0.00	1.25	1.31(32)*
		1.50	1.88(41)*†
		1.00	0.91(26)
	0.05	1.25	1.50(39)*
		1.50	2.16(51)*†
		1.00	1.03(31)
	0.10	1.25	1.63(43)*†
		1.50	2.35(56)*†
		1.00	1.06(32)*
	0.15	1.25	1.65(43)*†
		1.50	2.38(55)*†

Table 5.5: The ratio of the transition strengths $B(E2)$ for the $4_1^+ \rightarrow 2_1^+$ and $2_1^+ \rightarrow 0_1^+$ transitions in ^{140,142}Xe under the assumption that the two diagonal matrix elements correspond to the constraint from the IBA model calculation in the vibrator limit. The values indicated with an asterisk are additionally in agreement with the IBA constraints on the transitional matrix elements. The values indicated with a dagger are in agreement with the multi-phonon excitation picture for vibrational nuclei (see text for details).

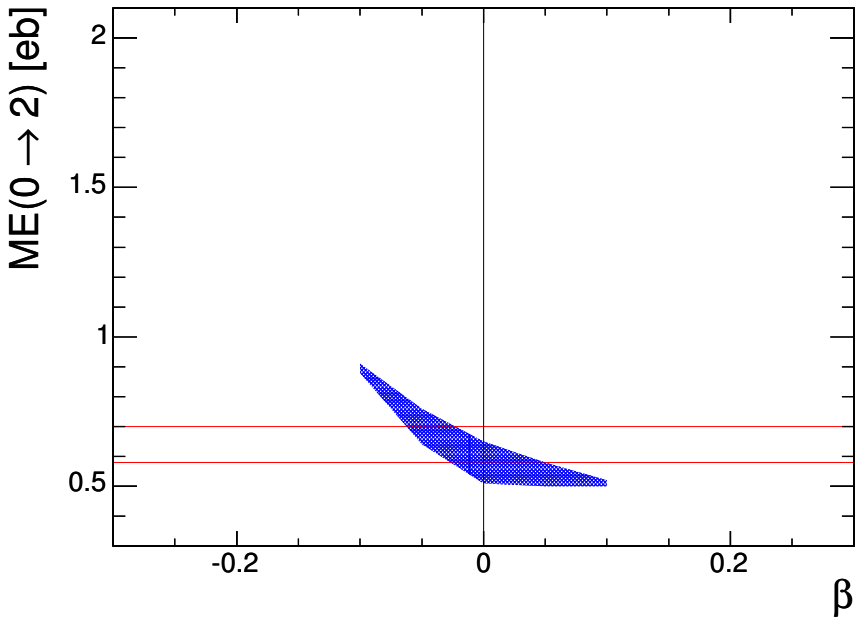

Figure 5.10: The maximal allowed regions for ME($0 \rightarrow 2$) versus the quadrupole deformation parameter for ^{138}Xe. The other matrix elements range from ME($2 \rightarrow 4$) = 1.0 to 1.5 *eb* and ME($4 \rightarrow 4$) = -6 to +6 *eb*. Red lines indicate the value from the modified Grodzins rule ± 20%. The black line corresponds to $\beta = 0$ (Moeller et al., 1995).

of ±20% is taken into account for the $B(E2)$ values derived with the modified Grodzins rule.

Limits of β for Systematic $B(E2)$ values

Isotope	$B(E2)_{sys}[e^2b^2]$	β
^{138}Xe	0.41	-0.02(4)
^{140}Xe	0.58	-0.03(9)
^{142}Xe	0.69	0.08(5)

Table 5.6: The resulting possible values of β assuming the $B(E2)$ value to be as estimated from the modified Grodzins rule (± 20%) for $^{138-142}$Xe. The constraints are taken from $\sigma_{ce}^{0\rightarrow 2}(\vartheta)$.

A theoretical calculation of nuclear masses and deformations has been performed by (Moeller et al., 1995), utilizing a sophisticated macroscopic-microscopic model including additional shape degrees of freedom and improved pairing calculations. The shape parameters have been determined by calculating the potential-energy surfaces, minimizing the ground-state energies and searching for the minima in the potential-energy surfaces. Although they used a different parameterization for the nuclear shape, the corresponding quadrupole deformation parameter β has also been obtained. These

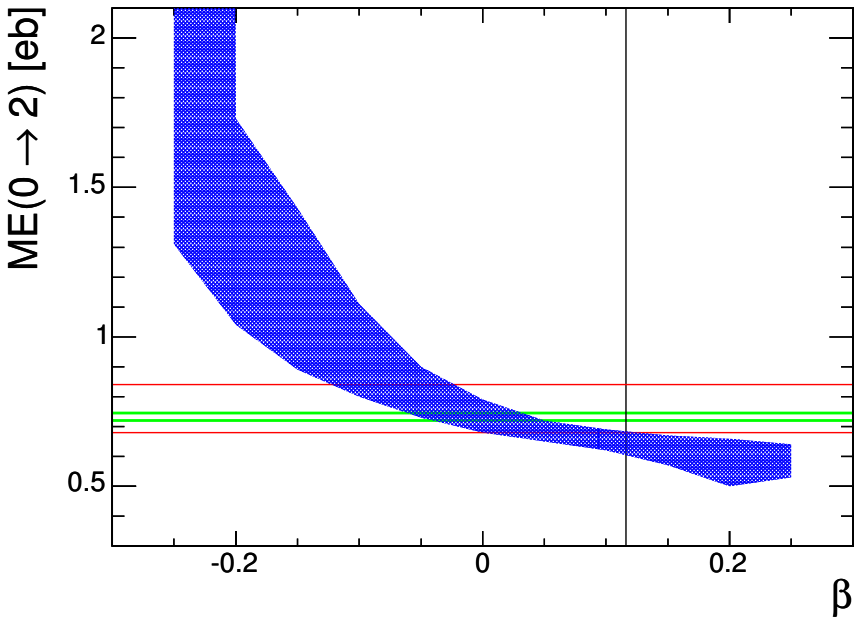

Figure 5.11: The maximal allowed regions for ME($0 \rightarrow 2$) versus the quadrupole deformation parameter for ^{140}Xe. The other matrix elements range from ME($2 \rightarrow 4$) = 1.0 to 1.5 *eb* and ME($4 \rightarrow 4$) = -6 to +6 *eb*. Red lines again indicate the value from the modified Grodzins rule ± 20%. The value determined by Lindroth et al. (1999) is in agreement with that (green lines). The black line shows that the deformation parameter calculated by Moeller et al. (1995) ($\beta = 0.116$) is not in agreement with these values.

theoretically derived values of β are also compared to the experimental data in this work (see table 5.7). Note that this β value for ^{140}Xe is not in agreement with the experimental results from Lindroth et al. (1999).

$B(E2)$ **Limits with Respect to** β

Isotope	β	$B(E2; 0^+_{g.s.} \rightarrow 2^+_1)$ $[e^2b^2]$
^{138}Xe	0.000	0.34(8)
^{140}Xe	0.116	0.40(3)
^{142}Xe	0.145	0.55(13)

Table 5.7: The resulting $B(E2)$ values for $^{138-142}$Xe assuming a quadrupole deformation parameter as calculated in Moeller et al. (1995).

Assuming $\beta \simeq 0$, no deviation from Grodzins systematics could be found. This is also true for the $N = 84$ nucleus ^{138}Xe, in contrast to the $B(E2)$ value of ^{136}Te measured by Radford et al. (2002). It is worth mentioning here that a new measurement at HRIBF indicates this value to be larger by about 30% (Baktash, 2005), whereas a

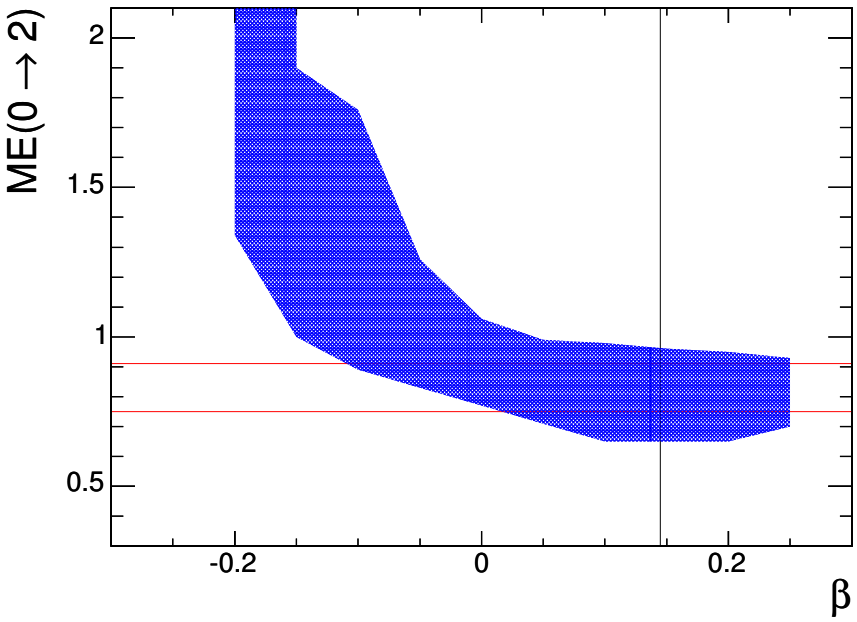

Figure 5.12: The maximal allowed regions for ME(0 → 2) versus the quadrupole deformation parameter for ^{142}Xe. The other matrix elements range from ME(2 → 4) = 1.0 to 1.5 *eb* and ME(4 → 4) = -6 to +6 *eb*. Red lines indicate the value from the modified Grodzins rule ± 20%. The black line corresponds to $\beta = 0.145$ (Moeller et al., 1995).

recent lifetime measurement (Fraile, 2008) even indicates an increase of about 50%.

Measurements of Cd isotopes with $N < 82$ also do not show any evidence for a weakening of the $N = 82$ shell gap in this region. Note that the measurements of this isotopic chain will be extended towards the r-process *waiting-point* nucleus ^{130}Cd with a Coulomb excitation experiment of a ^{128}Cd beam at REX-ISOLDE (Kröll et al., 2007). The trend of decreasing $B(E2)$ values for Cd isotopes when approaching the shell closure has been reproduced by shell model calculations (Scherillo et al., 2004), although these values are significantly lower than expected and experimentally determined (see figure 5.14).

For $^{138-142}$Xe the $B(E2)$ values have been determined including the deorientation effect in the analysis. They agree well with the modified Grodzins rule and it is also possible to reproduce the $B(E2)$ values of ^{140}Xe measured by Lindroth et al. (1999). However, assuming transitional matrix elements as in Lindroth et al. (1999) the theoretically calculated quadrupole deformation parameter β (Moeller et al., 1995) is no longer consistent with the experimental data.

The experimentally determined $B(E2)$ values are also compared to the QRPA calculations (Terasaki et al., 2002) and to more recent **M**onte-**C**arlo **S**hell **M**odel (MCSM) calculations (Shimizu et al., 2006), both of which were able to reproduce the $B(E2)$ value of ^{136}Te (cf. figure 5.14). It is worth emphasizing that both theoretical approaches underestimate the experimentally determined $B(E2)$ values.

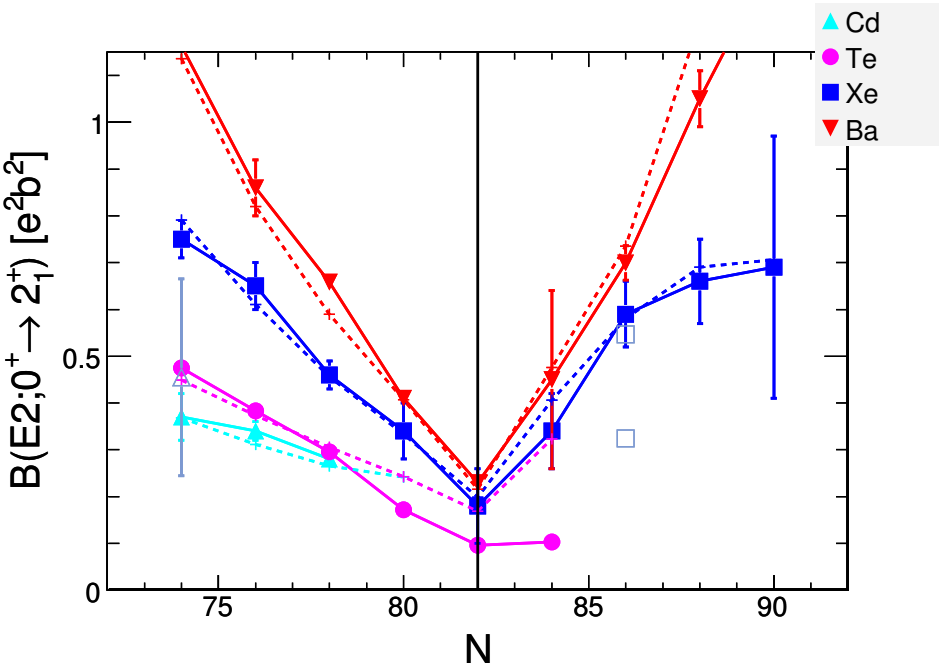

Figure 5.13: The $B(E2)$ values for selected isotopes around $N = 82$, including the results from the experiments discussed in this thesis assuming a vanishing quadrupole moment. The old values for ^{122}Cd (open triangle) and ^{140}Xe (open squares) are also shown. The $B(E2)$ values derived with Grodzins rule are indicated for comparison (dashed lines).

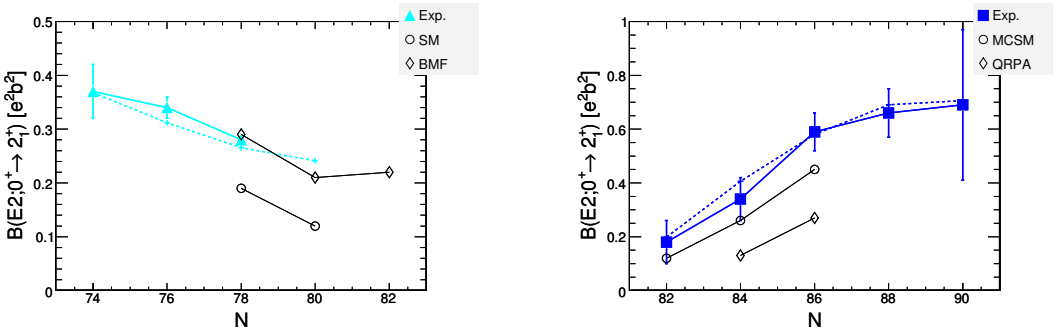

Figure 5.14: Left: A comparison of experimentally determined $B(E2)$ values (filled triangles) for $^{122-126}$Cd to shell model (SM) calculations (open circles) and theoretical values from a *beyond mean-field* approach (BMF). The latter are taken from Jungclaus (2007). Right: A comparison of QRPA and MCSM calculations (open markers) with experimentally determined $B(E2)$ values (filled squares) for neutron-rich Xe isotopes. In both cases the dashed line indicates the values derived from the modified Grodzins rule.

Additionally the data of $^{138-142}$Xe has been compared to constraints from IBA model calculations in the $U(5)$ limit, i.e. assuming the nuclei to be ideal vibrators. This is a reasonable approximation regarding their $\mathcal{R}_{42}$ values (see section 1.3). It could be shown that these constraints can be in agreement with the experimental data.

The Interacting Boson Model

Besides the geometric model (see section 1.1) and the shell model (see section 1.2), another approach for modeling the nucleus has been established in the 1970s.

The **I**nteracting **B**oson **A**pproximation, introduced by Arima and Iachello (1975), is an algebraic approach utilizing group theoretical methods. It effectively truncates the shell model space by neglecting closed shells and coupling the valence nucleons pairwise to so-called *s-* and *d-bosons* with total angular momenta of 0 and 2. The low-lying excitations of even-even nuclei can then be described by the energies and interactions of these bosons.

Mathematically, the s-d boson system can be described in terms of the $U(6)$ group, with 6 being the sum of the magnetic substates of the s ($J = 0$) and d ($J = 2$) boson. The subgroup $U(5)$ can then be shown to be a useful description for ideal vibrators, which has been assumed for the calculations in this work. A basic introduction to the IBA model can be found in Casten (2000) and references therein.

Treating $^{138-142}$Xe as ideal vibrators the IBA calculations result in constraints on the ratios of the included matrix elements. These constraints are summarized in table 5.8 and shown in figure 5.9.

Constraints from IBA Calculations

Isotope	ME($4 \rightarrow 2$)/ME($2 \rightarrow 0$)	ME($4 \rightarrow 4$)/ME($2 \rightarrow 2$)
^{138}Xe	1.55	2.0
^{140}Xe	1.64	2.0
^{142}Xe	1.70	2.0

Table 5.8: The resulting constraints on the ratios of the matrix elements for $^{138-142}$Xe from IBA calculations in the $U(5)$ limit (see text for details).

Outlook

With the experiments described in this work, the $B(E2; 0^+_{g.s.} \rightarrow 2^+_1)$ values of exotic nuclei around the $N = 82$ shell closure have been determined.

The study of the $Z = 48$ (i.e. Cd) isotopic chain below $N = 82$ will be continued with a low-energy Coulomb excitation experiment of ^{128}Cd at REX-ISOLDE (Kröll et al., 2007). Since one possible explanation of the $A \approx 130$ peak in the solar r-abundances is a quenching of the $N = 82$ shell closure for spherical nuclei below ^{132}Sn (i.e. $Z < 50$ and $N < 82$), this measurement might shed new light on this still open question. Another remarkable feature of ^{128}Cd is that the energy of its first excited state $E(2^+_1) = 645\ keV$ is *lower* than in ^{126}Cd, in contrast to the expectations when approaching a shell closure.

For nuclei above $N = 82$ Terasaki et al. (2002) proposed a reduced neutron pairing to explain the anomalous $B(E2)$ value of ^{136}Te. Hence, the investigation of $B(E2; 0^+_{g.s.} \rightarrow 2^+_1)$ values described in this work will be extended towards more collective nuclei with measurements of ^{140,148,150}Ba (Kröll et al., 2006). There is already experimental data indicating a decreasing neutron pairing gap for Ba isotopes above $N = 86$, though theoretical calculations only predict a dip at $N = 88$ (Terasaki et al., 2002).

For the measurement of heavy Ba isotopes at REX-ISOLDE the development of molecular BaF^+ beams is necessary. The molecules will be cracked in the EBIS, resulting in a complete suppression of isobaric contaminants. However, the development of these molecular beams is still in progress.

The heaviest Ba isotope for which a $B(E2)$ value is published is ^{146}Ba, although a new measurement of ^{148}Ba is included in figure 5.15. The value derived for ^{140}Ba has a relative uncertainty of about 50%. Since this nucleus is just above the $N = 82$ shell closure, a more precise measurement is desirable. The measurement of $B(E2; 0^+_{g.s.} \rightarrow 2^+_1)$ values of heavy Ba isotopes will also help to distinguish between predictions following the phenomenological systematics established as Grodzins rule from recent Monte-Carlo shell model calculations (see figure 5.15).

However, the data analysis described in this thesis showed that the measurement of $B(E2)$ values by means of Coulomb excitation experiments is hampered by (i) the uncertainty in the scattering angle ϑ and (ii) the lack of knowledge on the quadrupole deformation of the state under investigation.

The first difficulty can be overcome by the development of a new target chamber where the distance between target and CD detector is about twice as large, resulting in a far better angular resolution (Bildstein). Additionally, the barrel-shaped structure (see figure 5.16) allows the implementation of particle detectors parallel to the beam axis, hence covering a larger range in ϑ_{CM}. Due to a larger distance between the target

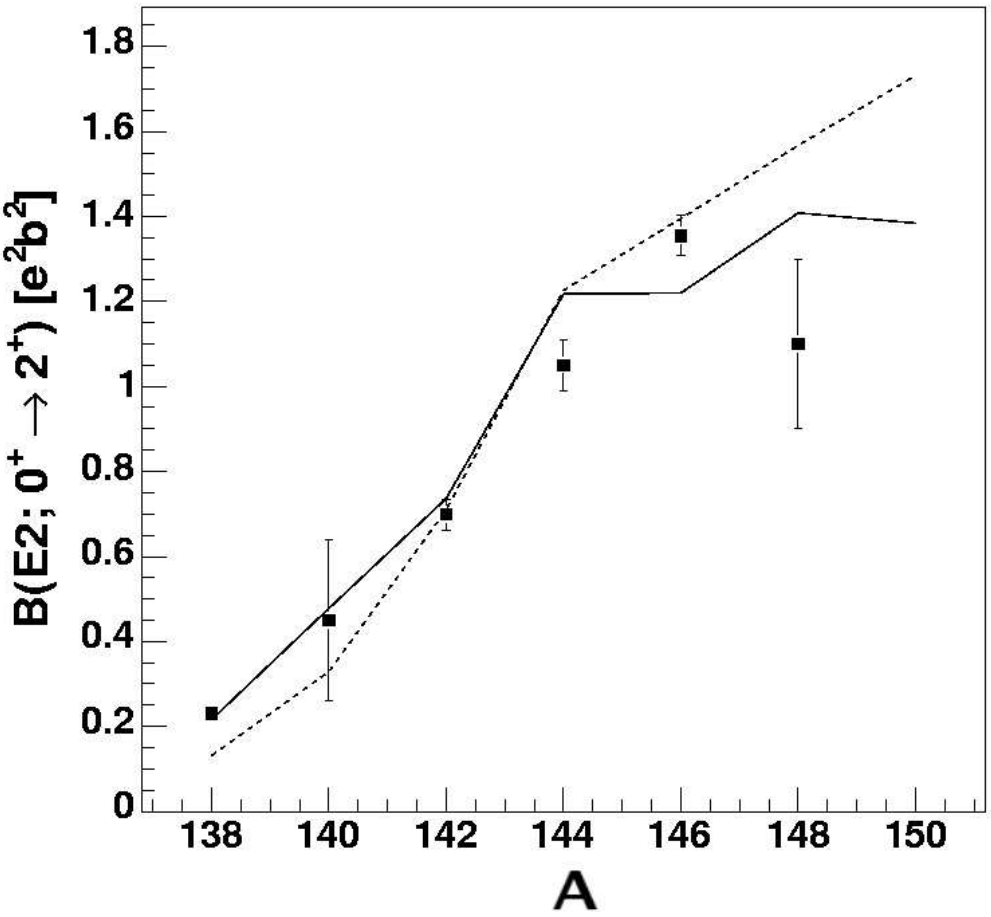

Figure 5.15: Experimental $B(E2)$ values for neutron-rich Ba isotopes. The solid line shows values derived from the modified Grodzins rule, the dashed line corresponds to Monte-Carlo shell model calculations (Shimizu et al., 2001). This plot is taken from Kröll et al. (2006).

and the MINIBALL detectors this new setup results in a reduced photopeak efficiency. But this is more than compensated by the larger particle detection efficiency.

The second problem could - in principle - be overcome by complementary lifetime measurements of the nuclear state investigated. However, this is only possible for lifetimes $\tau \lesssim 1ns$, because the state has to decay within the setup. It might therefore not be suitable for low-lying states in rotational nuclei. Of course, reasonable assumptions on the quadrupole moment based on theoretical calculations can be applied and the variation of the results within a range of β values can be checked.

On the other hand, a better angular resolution and a larger angular coverage enables a more precise and detailed measurement of the angular distribution of the Coulomb excitation cross section $\sigma_{ce}(\vartheta)$. In addition with smaller uncertainties of both the experimentally determined and the theoretical calculated cross sections, this might pin down the matrix elements more strictly.

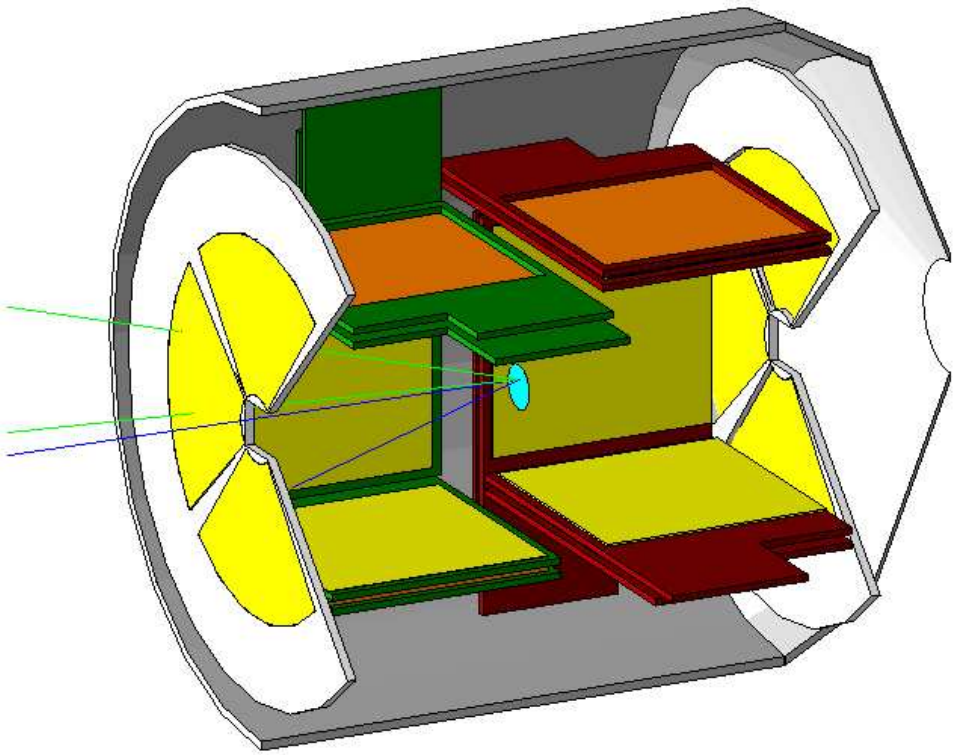

Figure 5.16: Schematic view of the new target chamber design. Note that there are two CD detectors mounted in forward and backward direction. Additionally segmented Si detectors are surrounding the beam axis, covering a much larger range of scattering angles (by courtesy of Kathrin Wimmer).

It remains to be emphasized that the investigation of neutron-rich nuclei, especially when going to more collective nuclei, will not only provide better data for nuclear structure and nucleosynthesis models, but might as well turn out to uncover new phenomena in nuclear physics that have not been thought of so far.

Bibliography

Abragam, A. and Pound, R. V.: 1953, *Phys. Rev.* **92(4)**, 943

Alder, K., Bohr, A., Huus, T., Mottelson, B., and Winther, A.: 1956, *Rev. Mod. Phys.* **28(4)**, 432

Alder, K. and Winther, A.: 1975, *Electromagnetic Excitation*, North-Holland Publishing Company

Ames, F., Cederkäll, J., Sieber, T., and Wenander, F. J. C.: 2005, *The REX-ISOLDE Facility: Design and Commissioning Report*, CERN, Geneva

Arima, A. and Iachello, F.: 1975, *Phys. Rev. Lett.* **35(16)**, 1069

Baktash, C.: 2005, *Selected Nuclear Structure Studies Near Coulomb Barrier at HRIBF*, MAFF Workshop

Bildstein, V., *in progress*, Ph.D. thesis, Technische Universität München

Bohr, A. and Mottelson, B. R.: 1975, *Struktur der Atomkerne*, Akademie-Verlag, Berlin, 1. edition

Brun, R. et al.: 2009, *ROOT: An Object-Oriented Data Analysis Framework - Users Guide*, CERN, <http://root.cern.ch/>

Casten, R. F.: 2000, *Nuclear Structure from a Simple Perspective*, Oxford Studies in Nuclear Physics, Oxford University Press, 2nd edition

Chadwick, J.: 1932, *Proc. Roy. Soc. Lond. A* **136(830)**, 692

Cheifetz, E. et al.: 1980, in *Proc. Conf. Nucl. Spectr. Fission Products, Grenoble, 1979*, p. 193

Danchev, M. et al.: 2005, *Nucl. Instr. Meth. B* **241(1-4)**, 971

Dillmann, I. et al.: 2003, *Phys. Rev. Lett.* **91(16)**, 162503

Eberth, J. et al.: 2001, *Progress in Particle and Nuclear Physics* **46(1)**, 389

Eppinger, K.: 2006, *Master's thesis*, TU München

Fraile, L.: 2008, in *INPC 2007 - Proceedings of the 23rd International Nuclear Physics Conference*

Gamow, G.: 1930, *Proc. Roy. Soc. Lond. A* **126(803)**, 632

Geiger, H. and Marsden, E.: 1909, *Proc. Roy. Soc. Lond. A* **82(575)**, 495

Grodzins, L.: 1962, *Physics Letters* **2(2)**, 88

Habs, D., Krücken, R., et al.: 2002, *Coulomb Excitation of Neutron-rich A∼140 Nuclei*, CERN Proposal INTC-P-156

Hager, R. and Seltzer, E.: 1968, *Nuclear Data A* **4**, 1

Haxel, O., Jensen, J., and Suess, H. E.: 1950, *Z. Phys.* **128**, 295

Heisenberg, W.: 1932, *Z. Phys.* **77**, 1

Heyde, K.: 1999, *Basic Ideas and Concepts in Nuclear Physics*, Graduent Student Series in Physics, Institute of Physics Publishing, 2nd edition

Jungclaus, A.: 2007, *Results from the RISING Stopped Beam Campaign 2006*, Annual NUSTAR Meeting

Jungclaus, A. et al.: 2007, *Physical Review Letters* **99(13)**, 132501

Kanungo, R. et al.: 2009, *Physical Review Letters* **102(15)**, 152501

Knoll, G. F.: 1979, *Radiation Detection and Measurement*, John Wiley & Sons

Kröll, T. et al.: 2006, *Coulomb Excitation of Neutron-rich A∼140 Nuclei*, CERN Proposal INTC-P-156 Add.3

Kröll, T. et al.: 2007, *Approaching the r-process "waiting point" Nuclei below ^{132}Sn: Quadrupole Collectivity in ^{128}Cd*, CERN Proposal INTC-P-226

Lauer, M.: 2004, *Ph.D. thesis*, Ruprecht-Karls-Universität Heidelberg

Lindroth, A., Fogelberg, B., Mach, H., Sanchez-Vega, M., and Bielcik, J.: 1999, *Physical Review Letters* **82(24)**, 4783

Lutter, R. et al.: 2009, *MBS and ROOT Based Online Offline Utility*, MLL, <http://www.bl.physik.uni-muenchen.de/marabou/html/>

Mayer, M. G.: 1950, *Physical Review* **78(1)**, 16

McClelland, C. L. and Goodman, C.: 1953, *Physical Review* **91(3)**, 760

Moeller, P., Nix, J., Myers, W., and Swiatecki, W.: 1995, *At. Data and Nucl. Data Tables* **59(2)**, 185

Niedermaier, O. T.: 2005, *Ph.D. thesis*, Ruprecht-Karls-Universität Heidelberg

Nier, A. O. and Roberts, T. R.: 1951, *Physical Review* **81(4)**, 507

Otsuka, T., Fujimoto, R., Utsuno, Y., Brown, B. A., Honma, M., and Mizusaki, T.: 2001, *Phys. Rev. Lett.* **87(8)**, 082502

Otsuka, T., Matsuo, T., and Abe, D.: 2006, *Physical Review Letters* **97(16)**, 162501

Otsuka, T., Suzuki, T., Fujimoto, R., Grawe, H., and Akaishi, Y.: 2005, *Phys. Rev. Lett.* **95(23)**, 232502

Radford, D. C. et al.: 2002, *Phys. Rev. Lett.* **88(22)**, 222501

Raman, S., Nestor, C., and Tikkanen, P.: 2001, *At. Data and Nucl. Data Tables* **78(1)**, 1

Ring, P. and Schuck, P.: 2000, *The Nuclear Many-Body Problem*, Texts and Monographs in Physics, Springer Verlag, 2nd edition

Rutherford, E.: 1911, *Philos. Mag.* **6(21)**, 669

Schatz, H. et al.: 1998, *Phys. Rep.* **294(4)**, 167

Scherillo, A. et al.: 2004, *Phys. Rev. C* **70(5)**, 054318

Schiffer, J. P. et al.: 2004, *Phys. Rev. Lett.* **92(16)**, 162501

Schwalm, D., Bamberger, A., Bizzeti, P. G., Povh, B., Engelbertink, G. A. P., Olness, J. W., and Warburton, E. K.: 1972, *Nuclear Physics A* **192(3)**, 449

Shimizu, N., Otsuka, T., Mizusaki, T., and Honma, M.: 2001, *Phys. Rev. Lett.* **86(7)**, 1171

Shimizu, N., Otsuka, T., Mizusaki, T., and Honma, M.: 2006, *J. Phys.: Conf. Series* **49**, 178

Sommerfeld, A.: 1931, *Ann. d. Phys.* **407**, 257

Terasaki, J., Engel, J., Nazarewicz, W., and Stoitsov, M.: 2002, *Phys. Rev. C* **66(5)**, 054313

van de Walle, J.: 2006, *Ph.D. thesis*, Katholieke Universiteit Leuven

von Weizsäcker, C. F.: 1935, *Z. Phys.* **96(7-8)**, 431

Wallace, R. K. and Woosley, S. E.: 1981, *ApJS* **45**, 389

Weißhaar, D. W.: 2003, *Ph.D. thesis*, Universität zu Köln

Weisskopf, V. F.: 1938, *Phys. Rev.* **53**, 1018

Wilcke, W. W. et al.: 1980, *At. Data and Nucl. Data Tables* **25**, 389

XIA: 2007, *User's Manual Digital Gamma Finder (DGF) DGF-4C*, X-ray Instrumentation Associates, <http://www.xia.com/>

List of Figures

List of Tables

Danksagung

Als erstes möchte ich Herrn Prof. Dr. Reiner Krücken dafür danken, mich in das Gebiet der Kernstrukturphysik eingeführt und diese Arbeit ermöglicht zu haben. Seine intensive Betreuung hat stets zu neuen Ideen geführt.

Ferner möchte ich mich bei Thorsten Kröll und Roman Gernhäuser bedanken, ohne deren tatkräftige Unterstützung und großen Erfahrungsschatz diese Arbeit nicht so gelungen wäre.

Natürlich bedanke ich mich hier auch bei allen (jetzigen und ehemaligen) E12ern, die mir im Laufe der Zeit mit Rat und Tat zur Seite standen und die auch zu einer angenehmen, kollegialen Arbeitsatmosphäre beitrugen. Insbesondere möchte ich die Dienste unserer Administratoren würdigen und speziell Ludwig Maier für seine "Festplattenrettungsaktion" danken.

Dankend erwähnen sollte man auch unser Sekretariat, Petra Zweckinger und Sigrid Weichs, die oft Probleme mit der Verwaltung bzgl. Dienstreiseanträgen oder Reisekostenerstattungen lösen konnten.

Die in dieser Arbeit beschriebenen Experimente hätten natürlich nicht ohne die Mithilfe von Kollegen auch anderer Institute gelingen können. Deshalb möchte ich hier allen danken, die diese Experimente erst möglich gemacht haben und speziell denjenigen, die in einer der Strahlzeiten tatkräftig dabei waren. Insbesondere möchte ich hier auch Fredrik Wenander und Didier Voulot danken, die als Operateure an ISOLDE zum Gelingen aller Experimente wesentlich beigetragen haben.

Eine solche Doktorarbeit lebt aber nicht nur von fachlicher und kollegialer Unterstützung. Auch das private Umfeld des Doktoranden trägt zu ihrem Erfolg bei. Und deshalb möchte ich mich hier auch bei allen Freunden bedanken, die in den letzten Jahren so viel Geduld mit mir hatten und mich oft genug aufheitern konnten, wenn ich nicht weiter wusste. Insbesondere seien hier erwähnt Andi und Annegret, Christian, Matthi, Michael K., Michael S., Nadine, Robert und Stephan. Und natürlich Isabelle, der ein ganz spezieller Dank gebührt.

Last but not least möchte ich auch meinen Eltern danken, deren stete Unterstützung mir erst das Physikstudium möglich machte und die auch während der Promotion immer für mich da waren.

Danke an alle!